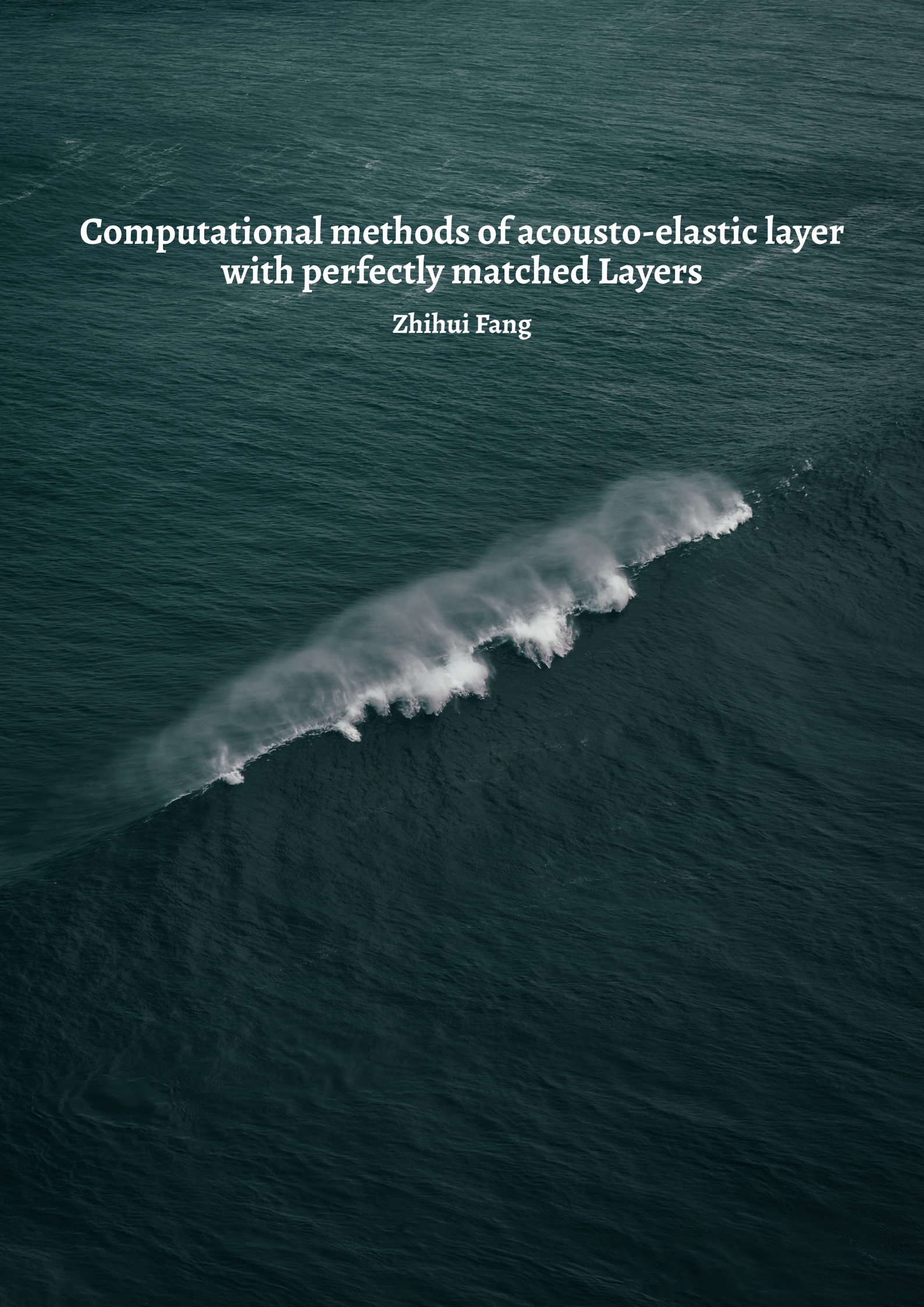# Computational methods of acousto-elastic layer with perfectly matched Layers

Zhihui Fang

Computational methods of acousto-elastic layer with perfectly matched layers

Master Thesis

for the purpose of obtaining the degree of Master of Science in Civil Engineering
at Delft University of Technology
to be defended publicly on Monday 8 September 2025 at 13:00 o'clock

by

Zhihui Fang

Graduaction Committee:

Dr. ir. A. Tsouvalas,	Offshore Engineering, Committee Chair
Ir. R.J. van Leijden,	Dynamics of Solids and Structures, Daily Supervisor
Dr. ir. A. Tsetas,	Dynamics of Solids and Structures, Daily Supervisor
Dr. ir. K.N. van Dalen,	Dynamics of Solids and Structures

An electronic version of this dissertation is available at
`https://repository.tudelft.nl/.`

TUDelft

Contents

Summary

Perfectly Matched Layer (PML) has become a powerful tool in computational underwater acoustics and elastodynamics. By employing complex coordinate stretching in the wavenumber–frequency domain, PMLs effectively attenuate outgoing waves from the physical domain and thereby provide an efficient means to truncate the computational domain. Although PMLs have been widely adopted in the finite element and finite difference communities, their use in semi-analytical solutions remains limited. A major challenge is that, when modal analysis is applied to the acousto-elastic domain with PML in a semi-analytical framework, the found modes are not orthogonal. This challenge formulates the main motivation of this research. On the other hand, the modes obtained from the discrete solution of the elastic layer with PML, based on the thin-layer method, do preserve orthogonality. Therefore, this thesis aims to understand the differences between the modal solutions of the semi-analytical and thin-layer methods in the elastic domains with PMLs, which may provides insights into the reasons why modes in the semi-analytical solution are not orthogonal to each other.

The main storyline of this thesis is developed through four cases with increasing system complexity. In the first case, the modes of the elastic domain are computed using both the semi-analytical approach and the thin-layer method (TLM), and the comparison demonstrates the equivalence of the two methods in the absence of PMLs. In the second case, the acoustic domain with PML is investigated using the semi-analytical approach, with emphasis on the polynomial order of the complex-stretching function. Mathematical derivations show that a zero-order polynomial induces discontinuities at the interface, leading to unelimiated boundary terms and perturbing modal orthogonality, while numerical results confirm that higher-order polynomials preserve the cross-orthogonality of modes, as well as the continuous slopes of the potential functions at the interface. In the third case, a quadratic complex-stretching function is employed, and the elastic domain with PML is analyzed using both approaches. The comparison reveals differences in eigenvalues and eigenvectors; finer TLM discretization yields increased matches between the two methods, but excessive discretization results in orthogonality violations. Finally, in the fourth case, the semi-analytical modes of the acousto-elastic domain with PML are studied. Propagating, evanescent, and Bérenger modes are identified, with cross-orthogonality preserved given sufficient integration points. Bérenger modes consistently arise in PML formulations and exhibit anomalous dispersion characteristics.

The main contribution of this thesis lies in revealing the influence of the polynomial order of the complex-stretching function on the modes of the acoustic domain with PML. When a quadratic complex-stretching functions are employed, the numerical results suggest that the semi-analytical modes of the elastic or acousto-elastic domains with PML are orthogonal. Therefore, it is suggested that a positive value of polynomial order is recommended when computing normal modes of the acousto-elastic domain with PML. However, in the future, a systematic study on the influence of the polynomial order should be conducted for the elastic layer or acousto-elastic domain with PML.

Furthermore, the comparative study of modal solutions highlights the differences between the semi-analytical approach and the thin-layer method. The nature of modal solutions comes from the different formulations of the eigenvalue problem, leading to different eigenvalues and eigenmodes. For TLM, the over-discretization of the PML domain is not suggested due to the violated orthogonality, although the reasons behind that require further investigations.

Overall, this thesis advances the fundamental understanding of the modal basis of acoustic, elastic, and acousto-elastic layers with PML formulations, providing a foundation for future research in two main directions: (i) the study on modes of the acoustic layers coupled with multiple elastic layers with PML, which better represent realistic ocean environments with geological strata; and (ii) the computation of forced responses of structures in acousto-elastic layers with PMLs to model the pile-water-soil interactions using modal matching techniques.

Preface

This thesis represents my explorations over the previous year in the field of computational underwater acoustics and elastodynamics, following up on my specialization in *Applied Dynamics of Structures* at TU Delft. Looking back, I may have forgotten the initial reason for entering the world of structural dynamics, but thanks to the efforts of all lecturers involved in the related modules, I fortunately found a domain I have enjoyed so much for the last two years.

I would like to first express my sincere gratitude to the chair Dr. ir. Apostolos Tsouvalas. Thank you, Apostolos, for introducing this challenging but interesting topic to me. Thank you very much for the trust, guidance, and suggestions you have given for this MSc thesis. Besides, I would like to extend my thanks Dr. ir. Karel. van Dalen for his valuable suggestions.

I would like to express my gratitude to my daily supervisors Ir. Rens van Leijden and Dr. ir. Athanasios Tsetas for their continuous guidance and support throughout this research. Thank you, Rens, for all the discussions whenever I needed them during the research internship and master thesis—we finally found an answer to the challenging question. Thank you so much for the help in debugging both this research and PyDynSM work. Thank you, Thanasis, for all the support during progress meetings and continuous guidance throughout the PyDynSM work.

I would like to express my gratitude to my colleagues who have made this journey memorable. Thank you, Rajat, for being an excellent teammate in nearly all our shared modules. Thank you, Dakka, for the wonderful cooperation during our TA work, PyDynSM, and U-BASE Committee activities. I would also like to express my thanks to everyone in U-BASE, who made my first year far from boring and filled with meaningful experiences.

I would like to extend my special appreciation to all Chinese friends at TU Delft. Thank you, Pengran, for giving me the freedom to stay in your office whenever I needed it. Thank you, Liangzhi, for being my roommate—I enjoyed every hangout and travel with you guys during these two years. Thank you, Hang, for being one of my 'MSc thesis teammates' and for your suggestions regarding finding a job and housing. I really wish you a bright future in the Netherlands. Thank you, Luyuan, for sharing your experiences with PhD applications. I wish you the best of luck in your future academic life in Germany.

Finally, I would like to thank my family and friends in China. Thank you, Yi, Qi, and Yihang, for all the continuous support and encouragement; I could not have survived the last five years without you. I would like to express my deepest gratitude to my parents—thank you for all your unconditional love, trust, and support over the years. I want to extend my special thanks to my cousin. I regret that I cannot stay with you during your most difficult time, but I am extremely happy for your recovery and I wish you all the best in the future.

I hope my maternal grandmother and grandfather could see my work—they would be happy for me.

Zhihui
Delft, July 2025

1

Introduction

1.1 Motivation and research questions

A waveguide is a finite domain with parallel boundaries, where energy propagates via multiple reflections between the upper and lower surfaces [7, 20]. Elastic and acoustic waveguides are essential in numerous engineering applications, such as underwater acoustics, seismic exploration, and structural health monitoring, as they facilitate wave propagation over large distances [8]. Normal mode methods are one of the approaches for studying wave propagation in acoustic or elastic waveguides [11]. More specifically, their robustness and computational efficiency contribute to their preference over wavenumber integration techniques [20]. Studies have also shown that normal mode solutions are widely applied to wave propagation in bounded media without range dependency. However, existing models of ocean environments include layered waveguides and a half-space [11]. Among existing literature, a combination of complex wavenumber integration and modal methods was found to provide the exact solution [16]. However, purely adopting the standard mode solution for wave propagation in infinite or semi-infinite media necessitates truncation.

In general, two approaches have been used in the existing research for domain truncation: (1) assuming *a non-reflecting boundary condition* at the truncation interface; (2) defining an *absorbing boundary layer*. The first approach minimizes wave reflection from the interface by applying an appropriate boundary condition at the interface between the computational domain and the truncated domain. The non-reflecting boundary conditions can be either exact or local, where a comprehensive review of these two categories was given in [25]. The exact method provides high accuracy but is computationally expensive, whereas the local method is more efficient but introduces errors due to reflections [13]. In the second approach, an absorbing layer is introduced to enforce the decay of wave motion within the region, thereby minimizing waves reflected from the truncation interface. This approach is considered to be one of the most successful techniques for numerical truncation, mainly due to the success of Perfectly Matched Layers (PMLs).

Perfectly Matched Layer (PML) is one type of the aforementioned absorbing layer. PML was initially developed and implemented by Bérenger [5] for Maxwell's equations by introducing an additional flat layer beneath the regular domain. This layer attenuates electromagnetic waves propagating in all directions. Consequently, reflections at the interface of PMLs and the regular domain can be minimized. In [5], Bérenger highlighted the mathematical superiority of the PML approach over existing absorbing layers by achieving a significantly lower reflection rate, independent of their incident angles. Extending from application in electromagnetics, extensive research suggests the successful application of PML formulations in elastic wave propagation problems, and a comprehensive review of their applications can be found in [13].

Although perfectly matched layers (PMLs) are widely utilized in the Finite Element (FE) community, their application in semi-analytical solutions remains limited. Furthermore, the nonphysical nature of PMLs also introduces leaky modes for some cases [9, 26], which corresponds to poles of the characteristic equations located in the improper Riemann sheets. Leaky modes grow exponentially in the vertical direction, indicating they violate the radiation conditions for exact and continuous solutions of displacements in the lower half-space. Alongside normal and leaky modes, Bérenger modes are also

identified in the eigenvalue problems of waveguides with PMLs. Those modes, with energy localized in the PML regions, are sensitive to PML parameters [17]. Moreover, they are considered to be purely mathematical modes with anomalous modal shapes [4]. Generally, educated guesses based on boundary and interface conditions can be given for an arbitrary question, called *continuous solutions*. Alternatively, numerical methods can be used to solve the same problem, leading to a *discrete solution*. These two types of modal solutions consist of *eigenvalues* and *eigenvectors*. Throughout this thesis, the eigenvalues arising in the continuous solution are sometimes referred to as roots, as they correspond to the solutions of the dispersion relation. The associated eigenvectors, or modes, are continuous functions defined over the modal coordinates. In contrast, in the discrete solution, the eigenvectors are represented as vectors of modal values sampled at discrete points.

More specifically, the continuous modal solutions presented in this work are semi-analytical, since the eigenvalues associated with the dispersion relations are computed using numerical root-finding algorithms. In addition to these continuous solutions, this thesis also employs a discrete solution, the Thin-Layer Method (TLM). Originally developed in the early 1970s, TLM has been widely used for wave propagation analysis. It discretizes the waveguide along the layering (typically transverse) direction, while analytical expressions are retained in the remaining coordinates [4].

When the Thin-Layer Method (TLM) is applied to the eigenvalue problem in an elastic domain with a perfectly matched layer (PML), the resulting discrete solution yields a set of normal modes whose associated eigenvalues exhibit the expected orthogonality. In contrast, the semi-analytical formulation no longer preserves orthogonality among different eigenvectors, despite describing the same physical system. This discrepancy between the continuous and discrete treatments of the same problem motivates a deeper investigation into the underlying mathematical and physical mechanisms, ultimately leading to the *main research question* of this thesis, which is:

> **How and why do the modal characteristics differ between semi-analytical and thin-layer method (TLM) solutions in acoustic or elastic domains with PMLs?**

The following supplementary questions are proposed to support the investigation of the main research question:

1. For a *linear isotropic elastic layer*, how do the eigenvalues and eigenmodes obtained from the semi-analytical method differ from those produced by the thin-layer method (TLM)? What are the primary factors contributing to these differences?

2. In a *fluid layer with a PML*, how does the presence of the PML affect the semi-analytical modal solutions? Specifically, how does varying the PML polynomial order m_{PML} influence the computed eigenvalues, eigenvectors, and their orthogonality?

3. For a *linear isotropic elastic layer with an adjacent PML*, what are the differences in modal characteristics (in particular, eigenvalues and eigenmodes) between the semi-analytical and thin-layer methods? What mechanisms account for these differences?

1.2   Research aim

This research aims at investigating how and why the modal solution of an elastic domain with PMLs differs between the following two computational methods: (1) the semi-analytical approach and (2) the thin-layer method. The comparison of results for the two methods may give insights into the reason why modal orthogonality fails sometimes in the semi-analytical solution.

1.3   Thesis objectives

The following four objectives of this thesis are given:

1. A comparative analysis between the Thin-Layer Method (TLM) and the semi-analytical solution for a linear elastic layer is first conducted to identify their similarities and differences. This comparison serves as an essential preparatory step for understanding more complex acoustic, elastic, and acousto-elastic domains involving perfectly matched layers (PMLs).

2. Investigate the modal behavior of an acoustic layer with a perfectly matched layer (PML), with particular attention to the orthogonality of modes and their associated eigenvectors, as formulated in [26]. While previous studies, such as [4], have frequently noted the emergence of nonphysical Bérenger modes, their mathematical and physical origins remain insufficiently explored. Here, a semi-analytical framework is employed to analyze the eigenvalue spectrum, modal structures, and dispersion characteristics, with the aim of clarifying the nonphysical nature of these modes. Furthermore, the impact of various complex-stretching functions on the modal properties is assessed, with an emphasis on the role of the polynomial order m_{PML}.

3. Examine the differences in modal solutions between two formulations—discrete (thin-layer method, TLM) and continuous (semi-analytical)—for an elastic medium with a perfectly matched layer (PML). Understanding the correspondence and divergence between these approaches is essential for analyzing wave propagation in PML-coupled elastic waveguides. However, such a comparative study remains largely absent in the existing PML literature, thus motivating this key objective of the thesis.

4. Provide a modal solution for an acousto-elastic layer with PML via the semi-analytical solution.

1.4   Scope of the research

The complete modal solutions of the acousto-elastic domain are a fundamental topic in the context of underwater acoustics and elastodynamics, and their successful applications in solving complex pile-water-soil interaction problems in offshore pile-driving activities can be found in existing research [16, 22, 24]. The focus of work in this thesis is limited to a few aspects:

1. Problems considered here are limited to unforced systems. For the unforced system, the starting point of analysis is the eigenvalue problem after the separation of variables. In the next stage, the eigenvalue problem will be solved using either the semi-analytical or thin-layer method, including the roots of the dispersion relations (eigenvalues) and their corresponding modes (eigenvectors). The study of this thesis will focus on the basic properties of modes when PML is presented.

2. Generally, the modal basis of the elastic domain contains P-wave type, SV-wave type, and SH-wave type modes. Among these, P-wave type and SV-wave type modes form Rayleigh modes propagating along the surface; the SH-wave type modes are associated with Love waves. The focus of the study is on the P-SV wave type of modes in the elastic domain.

1.5   Thesis outline

This thesis presents a comparative study of continuous and discrete modal solutions of an elastic layer incorporating a Perfectly Matched Layer (PML). It begins with a comparison of continuous and discrete modal solutions for a single elastic layer, which provides Subsequently, the continuous modal solution for a single acoustic layer with a PML is introduced. The comparative analysis is then extended to the elastic layer with PML, focusing on main differences between the continuous and discrete solutions. Based on previous discussions, the modal solutions of an acousto-elastic domain via the semi-analytical approach will eventually be provided. The thesis concludes with a summary of findings and offers recommendations for future research.

The structure of this thesis is visualized in Figure 1.1. Chapter 2 provides a review of the necessary theoretical background for this thesis, introducing key concepts and foundational principles that are relevant to this thesis.

Chapter 3 presents a comparative study of modal solutions obtained via a semi-analytical and thin-layer method for a single elastic layer. The chapter begins with the formulation of both solution methods, followed by a detailed comparison of the roots and eigenvectors under various frequencies and attenuation rate.

In Chapter 4, the semi-analytical approach is extended to a single acoustic waveguide with one PML. The formulation of the semi-analytical solution in the presence of the PML is presented in detail. Additionally, the properties of the roots and modes are examined, with particular attention given to the orthogonality between modes and their conjugate eigenvectors. Furthermore, this chapter also includes a discussion on the influences of the order of the polynomial complex-stretch function m_{PML} on the modal solutions.

Chapter 5 focuses on the modal analysis of an elastic layer with one PML. The formulations of the two approaches are briefly introduced, followed by a comparison of the resulting eigenvalues and eigenvectors. Finally, the orthogonality conditions of modes in the semi-analytical approach will be checked. This comparative study highlights the similarities and differences between the two methods, with a discussion on possible causes for any differences.

Chapter 6 presents the modal solutions of an acousto-elastic domain with a single PML, obtained using the semi-analytical approach. Following the methodology presented in Chapter 4, the analysis covers the eigenvalue, modes, and their cross-orthogonality properties.

Chapter 7 concludes the thesis by answering all research questions and providing recommendations for future research directions.
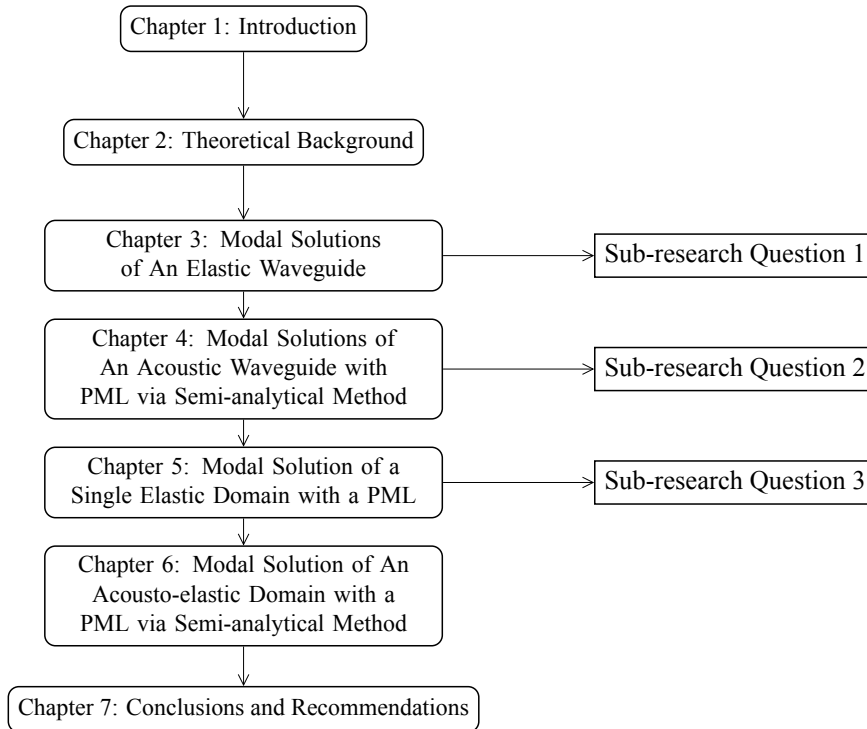
Figure 1.1. A flowchart of the structure of the thesis

2

Theoretical Background

Labels

dependent variables   independent variables

Figure 2.1. A Flow Chart of the theoretical framework of this thesis

In this Chapter, the theoretical background of this thesis will be introduced, along with a review of existing research within the continuous and discrete modal solutions of acoustic and elastic layers with and without PML formulations. As shown in the framework of all physical variables (See Figure 2.1), this chapter mainly provides:

{2.1} Basic mathematical definitions and the coordinate system used in this research.

{2.2} Wave propagation in acoustic and elastic media.

{2.3} An explanation of normal-mode solutions, including both the continuous and discrete form.

{2.4} Wave-dispersion phenomena.

{2.5} PML techniques, with a focus on complex stretch.

{2.6} A review of the Thin-layer method, including the formulation, orthogonality, and the application with PML.

2.1 Definitions

First of all, all integration transforms are defined here:

Fourier transform would be used for frequency domain analysis, which is given as below:

$$f(\mathbf{x}, t) = \int_0^\infty \tilde{f}(\mathbf{x}, \omega) \exp(\mathrm{i}\omega t)\, \mathrm{d}\omega, \qquad\qquad \tilde{f}(\mathbf{x}, \omega) = \int_0^\infty f(\mathbf{x}, t) \exp(-\mathrm{i}\omega t)\, \mathrm{d}t. \qquad (2.1)$$

In addition, the *Hankel functions* that are used in this thesis are as follows:

$$H_0^{(1)}(x) = J_0(x) + \mathrm{i}Y_0(x), \qquad\qquad H_0^{(2)}(x) = J_0(x) - \mathrm{i}Y_0(x). \qquad (2.2)$$

Two kinds of Bessel functions are plotted in Figure 2.2b, with the solid and dashed lines representing the first and second kind, respectively. The corresponding Hankel functions are plotted in Figure 2.2b.
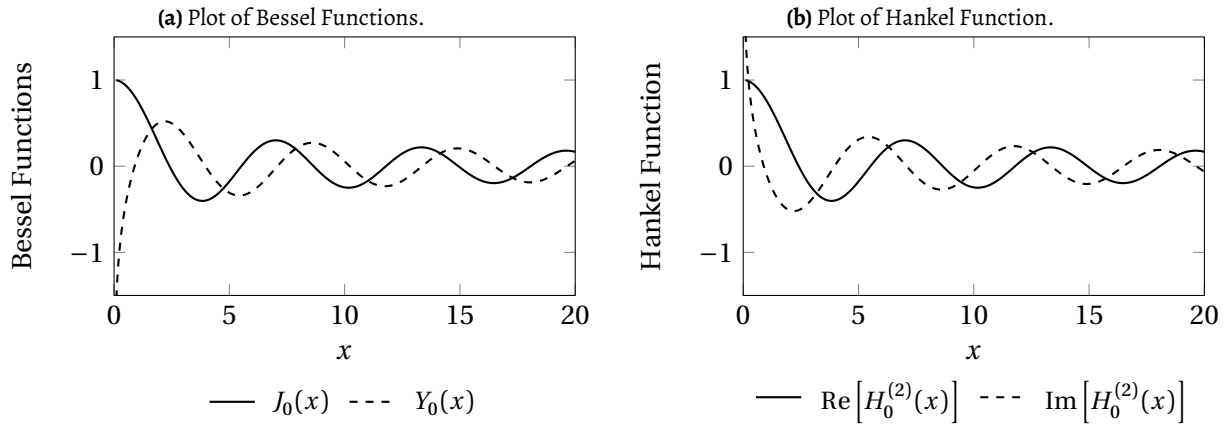

(a) Plot of Bessel Functions.   **(b)** Plot of Hankel Function.

— $J_0(x)$ - - - $Y_0(x)$ — $\mathrm{Re}\left[H_0^{(2)}(x)\right]$ - - - $\mathrm{Im}\left[H_0^{(2)}(x)\right]$

Figure 2.2. Indicative plots of Bessel and Hankel functions

Secondly, the following gradient operator ∇ and Laplacian operator ∇^2 will be utilized in this thesis:

$$\nabla = \partial_x\, \mathbf{e}_x + \partial_y\, \mathbf{e}_y + \partial_z\, \mathbf{e}_z, \qquad\qquad \nabla^2 = \partial_x^2\, \mathbf{e}_x + \partial_y^2\, \mathbf{e}_y + \partial_z^2\, \mathbf{e}_z.$$

where $\mathbf{e}_x$, $\mathbf{e}_y$, and $\mathbf{e}_z$ represent the unit vectors along the Cartesian coordinate axes x, y, and z, respectively, indicating the directional components of the gradient and Laplacian operators in three-dimensional space.

Finally, Einstein's summation convention was used for repeated indices. Besides, the Kronecker delta notation δ_{ij} is defined as

$$\delta_{ij} = \begin{cases} 1, & i = j, \\ 0, & i \neq j. \end{cases} \qquad (2.3)$$

2.2 Horizontally stratified waveguides

In the real ocean environment, the acoustic impedance varies continuously in the fluid layer, while it jumps at the interfaces between geological strata. Therefore, the layered model in the following figure could be applied in the analytical and numerical framework, aimed at reflecting two distinct types of medium heterogeneity [11]. The model in Figure 2.3 is assumed to be *horizontally stratified*, which is considered to be a widely recognized canonical model in underwater acoustics. This assumption indicates that waveguide properties are only dependent on z.
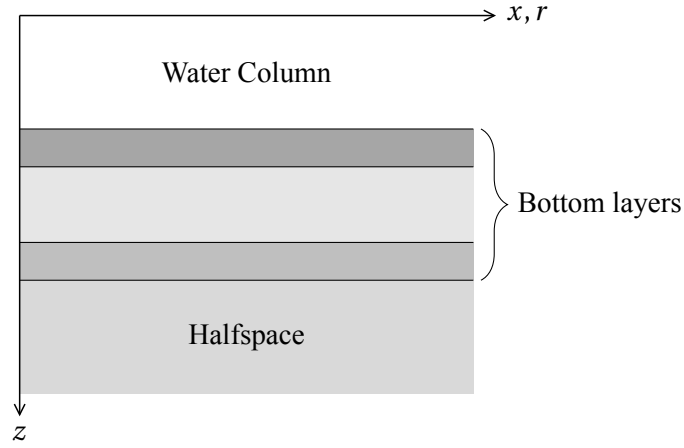
Figure 2.3. Horizontally Stratified Model
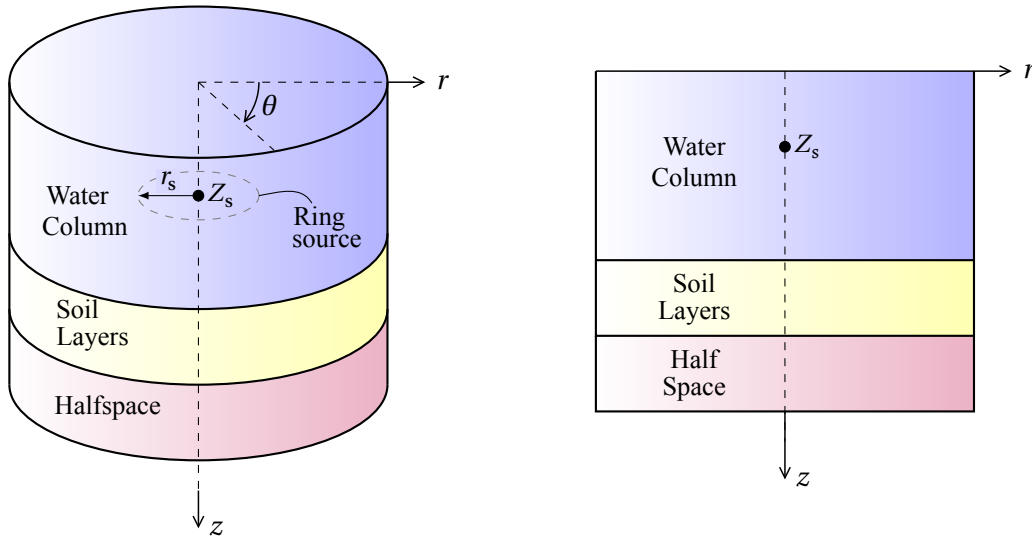
Figure 2.4. Schematic of the Coordinate System

2.3 Cylindrical coordinate system

The propagation of conical waves considered in this thesis is formulated as an *axisymmetric potential problem,* in which both the geometry and the applied boundary conditions are symmetric about the axis of revolution. A cylindrical coordinate system is adopted to express the analysis in the radial and axial directions [3].

In cylindrical coordinates, the position vector is expressed as $\mathbf{r} = (r, \theta, z)$, with the z-axis passing through the source (see Figure 2.4). Consequently, Equation (2.3) takes the form:

$$\nabla = \partial_r\, \mathbf{e}_r + \partial_\theta / r\, \mathbf{e}_\theta + \partial_z\, \mathbf{e}_z \qquad\qquad \nabla^2 = \partial_r\,(r\partial_r)\,/r + \partial_\theta^2/r^2 + \partial_z^2. \tag{2.4}$$

Given the assumption of axisymmetry in the cylindrical coordinate system, i.e., $\partial_\theta = 0$, Equation (2.4) should be simplified to:

$$\nabla = \partial_r\, \mathbf{e}_r + \partial_z\, \mathbf{e}_z \qquad\qquad \nabla^2 = \partial_r^2 + \partial_r/r + \partial_z^2. \tag{2.5}$$

2.4 Wave propagation in an acoustic medium

Linear wave equation

The motion of an inviscid, compressible fluid can be described by the scalar velocity potential $\phi_f(r, z, t)$, which satisfies the acoustic wave equation:

$$\nabla^2 \phi_f - \frac{1}{c_f^2} \ddot{\phi}_f = 0, \tag{2.6}$$

where cf denotes the sound speed in the fluid, and ∇^2 is the Laplacian operator as defined in Equation (2.5).

Helmholtz equation

Applying a Fourier transform to Equation (2.6) leads to the frequency-domain Helmholtz equation:

$$\nabla^2 \widetilde{\phi}_f + \frac{\omega^2}{c_f^2} \widetilde{\phi}_f = 0, \tag{2.7}$$

where $\widetilde{\phi}_f(r, z, \omega)$ denotes the velocity potential of the fluid layer in the frequency domain.

Constitutive relation

The velocity field $\tilde{\mathbf{v}}(r, z, \omega)$ and pressure field $\tilde{p}_f(r, z, \omega)$ in the fluid layer are given by:

$$\tilde{\mathbf{v}} = \nabla \widetilde{\phi}_f, \qquad\qquad \tilde{p}_f = -\mathrm{i}\omega \rho_f \widetilde{\phi}_f. \tag{2.8}$$

where ρ_f represents the fluid density and ∇ is the gradient operator defined in Equation (2.5).

2.5 Wave propagation in elastic medium

Navier-Cauchy equations

The motion of an isotropic, linear elastic soil layer is governed by Navier–Cauchy equation:

$$\mu_s \nabla^2 \mathbf{u}_s + (\lambda_s + \mu_s)\nabla\nabla \cdot \mathbf{u}_s - \rho_s \ddot{\mathbf{u}}_s = 0, \tag{2.9}$$

where $\mathbf{u}_s(r, z, t) = u_{s,r}(r, z, t)\,\mathbf{e}_r + u_{s,z}(r, z, t)\,\mathbf{e}_z$ denotes the displacement vector of the soil particles, ∇ is the gradient operator defined in Equation (2.5), λ_s and μ_s are the Lamé constants, and ρ_s is the density of the elastic medium.

Transforming Equation (2.9) into the frequency domain via the Fourier transform yields

$$\mu_s \nabla^2 \tilde{\mathbf{u}}_s + (\lambda_s + \mu_s)\nabla\nabla \cdot \tilde{\mathbf{u}}_s + \rho_s \omega^2 \tilde{\mathbf{u}}_s = 0, \tag{2.10}$$

where $\tilde{\mathbf{u}}_s(r, z, \omega)$ denotes the displacement field in the frequency domain and ω is the angular frequency.

Pontential relations

The displacement field of the soil layer $\tilde{\mathbf{u}}_s$ can be expressed via *Helmholtz decomposition*:

$$\tilde{\mathbf{u}}_s = \nabla \widetilde{\phi}_s + \nabla \times \widetilde{\mathbf{\Psi}}_s. \tag{2.11}$$

where $\widetilde{\phi}_s(r, z, \omega)$ denotes the scalar potential that is associated with compressional (P wave) motion, and $\widetilde{\mathbf{\Psi}}_s(r, z, \omega)$ stands for the vector potential describing transverse (S wave) motion, which is written as

$$\widetilde{\mathbf{\Psi}}_s = \widetilde{\psi}_s \mathbf{e}_\theta. \tag{2.12}$$

where $\widetilde{\psi}_s(r, z, \omega)$ is a scalar potential of SV wave.

Combining the contributions from $\nabla \widetilde{\phi}_s$ and $\nabla \times \widetilde{\boldsymbol{\Psi}}_s$ yields

$$\widetilde{\mathbf{u}}_s = \left(\partial_r \widetilde{\phi}_s - \partial_z \widetilde{\psi}_s\right)\mathbf{e}_r + \left(\partial_z \widetilde{\phi}_s + \partial_r \widetilde{\psi}_s + \widetilde{\psi}_s/r\right)\mathbf{e}_z. \tag{2.13}$$

Constitutive relations

The constitutive and compatibility laws in the soil layer are expressed as:

$$\widetilde{\sigma}_{ij} = \lambda_s \widetilde{\varepsilon}_{kk}\delta_{ij} + 2\mu_s \widetilde{\varepsilon}_{ij}, \qquad\qquad \widetilde{\varepsilon}_{ij} = \frac{1}{2}\left(\widetilde{u}_{i,j} + \widetilde{u}_{j,i}\right). \tag{2.14}$$

Uncoupled equations

Substituting (2.11) into Equation (2.9) gives:

$$\mu_s \nabla^2 \left(\nabla\widetilde{\phi}_s + \nabla \times \widetilde{\boldsymbol{\Psi}}_s\right) + (\lambda_s + \mu_s)\nabla\nabla \cdot \left(\nabla\widetilde{\phi}_s + \nabla \times \widetilde{\boldsymbol{\Psi}}_s\right) + \rho_s \omega^2\left(\nabla\widetilde{\phi}_s + \nabla \times \widetilde{\boldsymbol{\Psi}}_s\right) = 0. \tag{2.15}$$

The following properties of gradient and curl terms can be easily proved:

$$\nabla \cdot \nabla\widetilde{\phi}_s = \nabla^2 \widetilde{\phi}_s, \qquad \nabla \cdot \nabla \times \widetilde{\boldsymbol{\Psi}}_s = 0. \tag{2.16}$$

Substituting (2.16) into Equation (2.15) results in the following expression:

$$\nabla\left[(\lambda_s + 2\mu_s)\nabla^2\widetilde{\phi}_s + \rho_s\omega^2\widetilde{\phi}_s\right] + \nabla \times \left[\mu_s\nabla^2\widetilde{\boldsymbol{\Psi}}_s + \rho_s\omega^2\widetilde{\boldsymbol{\Psi}}_s\right] = 0. \tag{2.17}$$

The substitution of Equation (2.12) into (2.17) will give the following uncoupled Equations of Motions (EoMs) for P-SV waves [20]:

$$\nabla^2\widetilde{\phi}_s + \frac{\omega^2}{c_L^2}\widetilde{\phi}_s = 0, \tag{2.18}$$

$$\nabla^2\widetilde{\psi}_s - \frac{\widetilde{\psi}_s}{r^2} + \frac{\omega^2}{c_T^2}\widetilde{\psi}_s = 0. \tag{2.19}$$

Here, c_L and c_T (in m/s) represent the medium wave speeds of P waves and S waves, respectively, given by:

$$c_L^2 = \frac{\lambda_s + 2\mu_s}{\rho_s}, \qquad c_T^2 = \frac{\mu_s}{\rho_s}. \tag{2.20}$$

2.6 Normal-mode method

The normal-mode method has been extensively applied in both underwater acoustics and elastodynamics. A comprehensive treatment of this method in the context of underwater acoustics is given in Chapter 5 of [11], while its applications to elastic media are discussed in detail in [2]. In this work, only the aspects directly relevant to the present study are outlined for brevity.

Continuous solution

By applying the *separation of variables*, Equation (2.7) can be projected onto the modal coordinates:

$$\frac{d^2\widetilde{\Phi}_{f,p}}{dz^2} + \left(k_f^2 - k_{rp}^2\right)\widetilde{\Phi}_{f,p} = 0, \tag{2.21}$$

where $\widetilde{\Phi}_{f,p}(z,\omega)$ is the p-th mode of the velocity potential of the fluid layer.

The general solution to Equation (2.21) is given as below:

$$\widetilde{\Phi}_{f,p}(z,\omega) = A_1 \exp(i\gamma_f z) + A_2 \exp(-i\gamma_f z). \tag{2.22}$$

where $\gamma_f(\omega) = \sqrt{\omega^2/c_f^2 - k_{rp}^2}$, respresenting the vertical wavenumber of the p-th mode.

Similarly, the modal equations derived from Equations (2.18) and (2.19) are given by

$$\frac{d^2 \widetilde{\Phi}_{s,p}}{dz^2} + \left(k_L^2 - k_{rp}^2 \right) \widetilde{\Phi}_{s,p} = 0 \tag{2.23}$$

$$\frac{d^2 \widetilde{\Psi}_{s,p}}{dz^2} + \left(k_T^2 - k_{rp}^2 \right) \widetilde{\Psi}_{s,p} = 0 \tag{2.24}$$

The general solutions to the equations above are given as:

$$\widetilde{\Phi}_{s,p}(z,\omega) = A_3 \exp(i\gamma_L z) + A_4 \exp(-i\gamma_L z) \tag{2.25}$$

$$\widetilde{\Psi}_{s,p}(z,\omega) = A_5 \exp(i\gamma_T z) + A_6 \exp(-i\gamma_T z) \tag{2.26}$$

where $\gamma_L(\omega) = \sqrt{\omega^2/c_L^2 - k_{rp}^2}$ and $\gamma_T(\omega) = \sqrt{\omega^2/c_T^2 - k_{rp}^2}$ are the vertical wavenumbers of the P- and S-waves, respectively.

Furthermore, $\widetilde{\Phi}_{s,p}(z,\omega)$ and $\widetilde{\Psi}_{s,p}(z,\omega)$ denote the p-th modes of the scalar displacement potentials for P- and S-waves in the soil layer.

In a domain composed of layered media, a system of algebraic equations can be formed by introducing post-processed physical fields, namely, displacement, stress, and pressure, into interface and boundary conditions, which reads

$$\mathbf{MA} = \mathbf{f} \tag{2.27}$$

The *dispersion relation* is given by setting the determinant of $\mathbf{M}$ to zero:

$$\det \mathbf{M} = 0 \tag{2.28}$$

For each ω, solving equations above gives infinite number of $k_{rp}(\omega)$ with $p = 1, 2, 3, \ldots, \infty$. Furthermore, the modes corresponding to each root could also be computed, which formulate the following modal expansions of velocity and displacement potentials:

$$\widetilde{\phi}_f(r,z,\omega) = \sum_{p=1}^{\infty} C_p H_0^{(2)}(k_{rp} r) \widetilde{\Phi}_{f,p}(z,\omega), \tag{2.29}$$

$$\widetilde{\phi}_s(r,z,\omega) = \sum_{p=1}^{\infty} C_p H_0^{(2)}(k_{rp} r) \widetilde{\Phi}_{s,p}(z,\omega), \tag{2.30}$$

$$\widetilde{\psi}_s(r,z,\omega) = \sum_{p=1}^{\infty} C_p H_1^{(2)}(k_{rp} r) \widetilde{\Psi}_{s,p}(z,\omega). \tag{2.31}$$

where $\widetilde{\Phi}_{f,p}(z,\omega)$, $\widetilde{\Phi}_{s,p}(z,\omega)$ and $\widetilde{\Psi}_{s,p}(z,\omega)$ are known modes along z direction, the unknown complex-valued constants C_p are determined by solving the forced response of the whole system. It should be indicated that the solutions of C_p are beyond the scope of this thesis.

Discretized solution

For a discretized elastic medium, normal modes can be found by solving the following generalized eigenvalue problem:

$$\left(k_r^2 \mathbf{A}_s + k_r \mathbf{B}_s + \mathbf{G}_s - \omega^2 \mathbf{M}_s \right) \mathbf{\Phi}_s = \mathbf{0} \tag{2.32}$$

Where k_r is the radial wavenumber of cylindrical modes; $\mathbf{\Phi}_s$ is the displacement potential vector along z direction; $\mathbf{A}_s$, $\mathbf{G}_s$, and $\mathbf{M}_s$ can be derived from virtual work principle of a linear, isotropic elastic layer, which have been discussed in [12] and [19]. We will also revisit this discretized solution in the review of the thin layer method.

Eigenmodes

For the single acoustic or elastic media with a rigid bottom, only discrete eigenvalues can be found, as shown indicatively in Figures 2.5a and 2.5c. Modes whose eigenvalues lie close to the real axis are referred to as trapped modes, as their energy remains confined within the waveguide due to repeated reflections at the rigid boundary [20]. In contrast, modes near the imaginary axis are known as evanescent modes, with energy localized near the source and rapidly decaying with range. Symbolically, the modal content in such a *closed waveguide* can be expressed as:

$$\widetilde{\Phi} \simeq \sum_{m=1}^{M} \mathrm{Trapped\,Modes} + \sum_{m=1}^{M} \mathrm{Evanescent\,Modes}. \tag{2.33}$$

It should be noted, however, that in an elastic medium—whether lossless or lossy—the distribution of eigenmodes differs significantly, as shown indicatively in Figure 2.5c and 2.5b. This difference has been mentioned in [16] *for the elastic halfspace*: Dissipation is included in the form of complex-valued Lamé constants, leading to complex-valued eigenvalues in the third and fourth quadrants in an asymmetric way. However, for the lossless elastic medium, all modes are distributed symmetrically.

When the rigid boundary is removed, the complex contour integration must also account for the contributions of continuously radiated body waves. The physical interpretation of these contributions has been discussed in [22]: Their radial wavenumbers k_r are small and satisfy $0 < k_r^2 < k_T^2$. Such small values of k_r correspond to steep angles of incidence, resulting in continuous radiation of energy into the lower halfspace. Consequently, these conical wave types are so-called leaky modes, and they inherently violate the radiation condition. In this context, the total field is expressed as a combination of discrete trapped modes and a continuous spectrum of radiated modes, represented by an integration along the branch-cut contour (dashed line) in Figure 2.6:

$$\widetilde{\Phi} \simeq \sum_{m=1}^{M} \mathrm{Trapped\,Modes} + \int_{\mathscr{C}_{\mathrm{branch}}} \mathrm{Radiated\,Modes}. \tag{2.34}$$

(a) Fluid waveguide: single layer

(b) Lossless single elastic waveguide

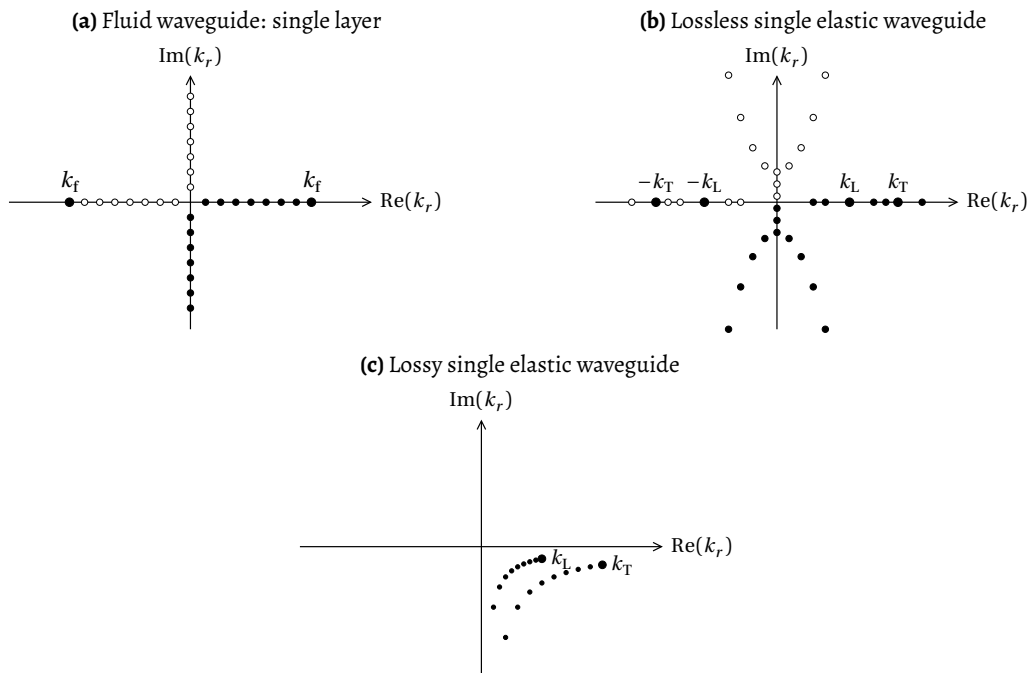**(c)** Lossy single elastic waveguide

Figure 2.5. Indicative positions of eigenvalues for different bounded layered media
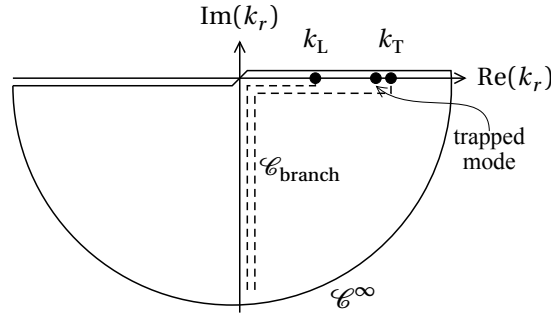
Figure 2.6. Complex contour integration of a lossless elastic halfspace

Modal dispersion

The founding of wave group phenomena by Russell (1844) marks the start of research on wave propagation in dispersive media. He found that some waves move more quickly than the group of waves. In 1876, Stokes developed the analytical expression of group velocity, which was later refined by Rayleigh. Following the definition of stationary by Kelvin (1887), Lamb gave the visualization of wave group-related concepts in 1990. The wave group is shown in Figure 2.7. It contains a modulation with a larger wavelength, which propagates with c_g and carrier waves propagating with $c_{ph} = c$.

A more general wave composed of wave groups with a continuous wavenumber spectrum, as shown in Figure 2.8a. A small variation $\Delta\text{Re}(k)$ around $\text{Re}(k_0)$, resulting in the $\Delta\omega$ around ω_0. This small perturbation is considered to be related to a cluster of waves with the following group $c_g(k_0)$ and phase velocity $c_{ph}(k_0)$:

$$c_g(k_0) = \partial_{\text{Re}(k_0)}\omega\big(\text{Re}(k_0)\big), \qquad c_{ph}(k_0) = \frac{\omega_0}{\text{Re}(k_0)}. \tag{2.35}$$

Achenbach [1] showed that its averaged energy density propagates with velocity:

$$c_E = c_g = \partial_{\text{Re}(k)}\omega \tag{2.36}$$

Based on this derivation, Miklowitz [14] pointed out that for symmetrical and antisymmetric P waves propagating in an infinite elastic plate, the aforementioned relationship is valid. Besides, the same conclusion has been proved for harmonic wave propagation in waveguides with constant cross sections.

For underwater acoustic wave propagation, modal dispersion is closely linked to energy transport. Jensen [11] observed that near the cut-off frequency, the phase velocity c_{ph} becomes large due to steep vertical wave propagation, attributed to a small k_r. Conversely, the group velocity c_g is nearly zero, reflecting a minimal horizontal energy transport. At higher frequencies, horizontally propagating waves dominate, causing c_{ph} and c_g to converge toward the medium's wave velocity c_f. As a result, c_{ph} decreases while c_g increases with frequency, with both asymptotically approaching c_f, as shown in Figure 2.8b.

For *physical dispersions*, the energy travels with the modulation in Figure 2.7 with $c_g < c_{ph}$. In other words, the energy travels more slowly than the phase of the waves. In contrast, anomalous dispersion occurs when $c_g > c_{ph}$ [14], Equation (2.35) yields:

$$\partial_{\text{Re}(k)}c_{ph} = \frac{\partial_{\text{Re}(k)}\omega\,\text{Re}(k) - \omega}{\text{Re}^2(k)} = \frac{1}{\text{Re}(k)}\big(c_g - c_{ph}\big) > 0 \tag{2.37}$$

That is to say, $\partial_{\text{Re}(k)}c_{ph} > 0$ for *anomalous dispersions*, suggesting their phase velocities c_{ph} increase with the real part of wavenumber $\text{Re}(k)$.
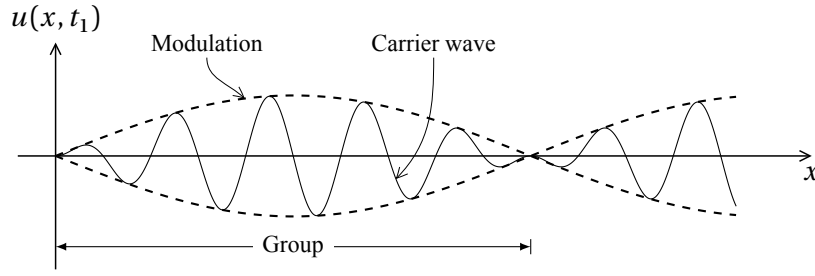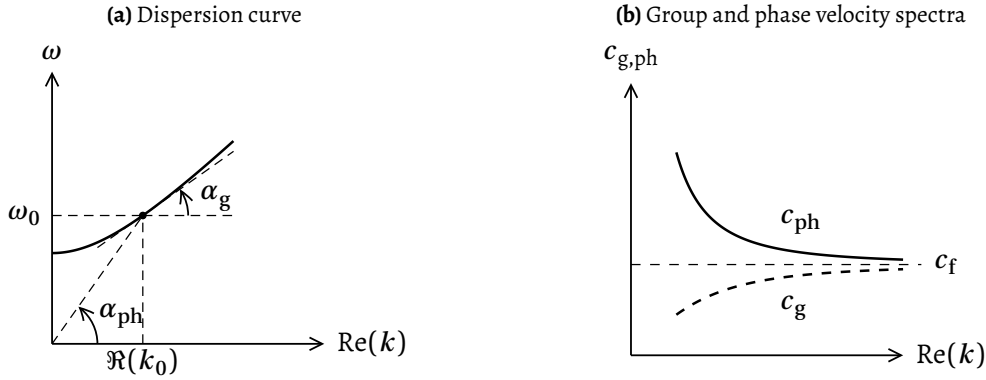
Figure 2.7. Wave grouping phenomena

Figure 2.8. Dispersion curve, wave and group velocity

Orthogonality The orthogonality of $P-SV$ modes for a single-layered elastic medium with a thickness of H_{EL} could be derived using reciprocity theorem of elastodynamics [6, 22], which could be found in as below:

$$\Gamma_{pq} = \Gamma_p \delta_{pq} = \int_0^{H_{EL}} \zeta_s \, k_p \, \tilde{u}_{s,r,p}(z) \frac{\tilde{u}_{s,r,q}(z)}{k_{r,q}} + \eta_s \cdot u_{s,r,p}(z) \frac{\sigma_{s,zz,q}(z)}{k_{r,p}}$$
$$- u_{s,z,p}(z) \frac{\sigma_{s,zr,q}(z)}{k_{r,q}} \, \mathrm{d}z, \tag{2.38}$$

where $\zeta_s = \rho_s \cdot \left[c_L^4 - (c_L^2 - 2 \cdot c_T^2)^2 \right] \big/ c_L^2$ and $\eta_s = \left(c_L^2 - 2c_T^2 \right) \big/ c_L^2$.

c_L and c_T are wave speeds of the compression and shear waves in the elastic waveguide, respectively. $\tilde{u}_{s,r}(z)$ and $\tilde{u}_{s,z}(z)$ define the displacement field of particles in the direction of r and z. $\tilde{\sigma}_{s,r}(z)$ and $\tilde{\sigma}_{s,z}(z)$ are normal and shear stresses respectively. Finally, k_r defines the radial wavenumbers.

What is more, the orthogonality of modes in an acoustic medium with a thickness of H_{FL} is given in [11] regarding modes of fluid potential $\phi_f(z)$, which is:

$$\Gamma_{pq} = \Gamma_p \delta_{pq} = \int_0^{H_{FL}} \frac{\phi_{f,p}(z) \phi_{f,q}(z)}{\rho_f} \, \mathrm{d}z, \tag{2.39}$$
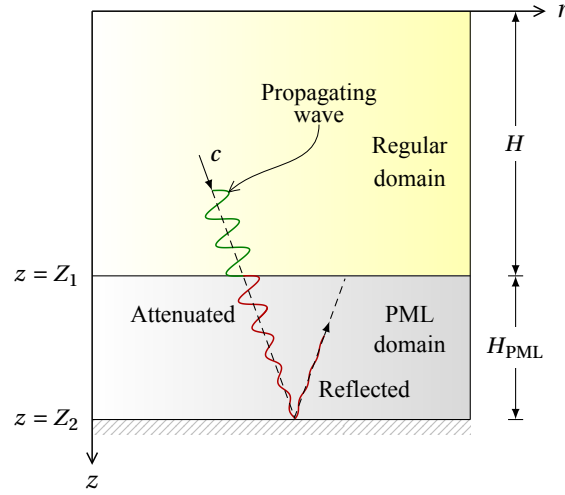
where ρ_f is the fluid density.

Figure 2.9. Schematic of A PML truncation boundary along coordinate z.

2.7 PML Technique

Initially developed by Bérenger [5] as an absorbing layer for electromagnetic waves, the Perfectly Matched Layer (PML) has been extensively applied in elastodynamics [4, 13] and underwater acoustics [10, 11, 26]. By employing complex stretching in the wavenumber-frequency domain, PMLs effectively attenuate waves in that layer, facilitating the truncation of numerical domains in semi-analytical and numerical formulations of open waveguides. This section will review the complex stretch technique and examine existing studies regarding its impact on modal contributions.

In the PML layer of Figure 2.9, $\mathrm{d}z$ is transformed to a complex-valued $\mathrm{d}\bar{z}$ by complex stretching function $\varepsilon(z, \omega)$:

$$\mathrm{d}\bar{z} = \varepsilon(z', \omega)\mathrm{d}z \tag{2.40}$$

Therefore, the transformed vertical coordinate $\bar{z}$ is

$$\bar{z} = \int_0^z \varepsilon(z', \omega)\,\mathrm{d}z'. \tag{2.41}$$

The complex stretching function $\varepsilon(z', \omega)$ in Equation (2.41) reads

$$\varepsilon(z', \omega) = \alpha(z) + \frac{\beta(z)}{\mathrm{i}\omega}, \tag{2.42}$$

where $\alpha_s(z)$ is called scaling function, and $\beta_s(z)$ is the attenuation function.
Moreover, they have the following basic properties:

1. When $0 < z < Z_1$, $\alpha(z) = 1$ and $\beta(z) = 0$.

2. When $Z_1 < z < Z_2$, $\alpha(z)$ and $\beta(z)$ *monotonically increase* with respect to z,

Therefore, the real and imaginary part of $\bar{z}$ are given as follow:

$$\mathrm{Re}(\bar{z}) = \int_0^z \alpha(z')\,\mathrm{d}z', \qquad\qquad \mathrm{Im}(\bar{z}) = -\frac{1}{\omega}\int_0^z \beta(z')\,\mathrm{d}z'. \tag{2.43}$$

In the PML layer, the basic properties of the scaling and attenuation functions imply

$$\mathrm{Re}(\bar{z}) > 1, \qquad\qquad \mathrm{Im}(\bar{z}) < 0. \tag{2.44}$$

Equation (2.40) indicates the following definitions related to spatial derivatives is given:

$$\frac{\mathrm{d}}{\mathrm{d}z} \rightarrow \frac{\mathrm{d}}{\mathrm{d}\bar{z}} = \frac{1}{\varepsilon} \cdot \frac{\mathrm{d}}{\mathrm{d}z} \tag{2.45}$$

For a *harmonic wave propagating within an one-dimensional PML layer* in Figure (2.9), where z is transformed to $\bar{z}$, the depth-separated part reads

$$\exp(-\mathrm{i}k\bar{z}) = \underbrace{\exp\left(-\mathrm{i}\mathrm{Re}(k)\mathrm{Re}(\bar{z}) + \mathrm{i}\mathrm{Im}(k)\mathrm{Im}(\bar{z})\right)}_{\text{Oscillatory part}} \cdot \underbrace{\exp\left(\mathrm{Re}(k)\mathrm{Im}(\bar{z}) + \mathrm{Im}(k)\mathrm{Re}(\bar{z})\right)}_{\text{Amplitude factor}}. \tag{2.46}$$

For a propagating wave, where $\mathrm{Re}(k) > 0$ and $\mathrm{Im}(k) = 0$, Equation (2.46) reads

$$\exp(-\mathrm{i}k\bar{z}) = \underbrace{\exp\left(-\mathrm{i}k\mathrm{Re}(\bar{z})\right)}_{\text{Oscillatory part}} \underbrace{\exp\left(k\mathrm{Im}(\bar{z})\right)}_{\text{Amplitude factor}}, \tag{2.47}$$

As a result, the propagating harmonic wave in Equation (2.46) is transformed into an *evanescent* one when $k\,\mathrm{Im}(\bar{z}) < 0$, because under this condition the exponential amplitude factor in Equation (2.46) decays with increasing $\mathrm{Im}(\bar{z})$. In the PML formulation, $\mathrm{Im}(\bar{z})$ increases monotonically with the physical coordinate z; therefore, the damping becomes progressively stronger toward the lower regions of the PML, ensuring effective absorption of outgoing waves.

For an *evanescent wave*, $\mathrm{Im}(k) < 0$ and $\mathrm{Re}(k) = 0$, hence Equation (2.46) is written as

$$\exp(-\mathrm{i}k\bar{z}) = \exp\left(\mathrm{i}\mathrm{Im}(k)\mathrm{Im}(\bar{z})\right)\exp\left(\mathrm{Im}(k)\mathrm{Re}(\bar{z})\right). \tag{2.48}$$

The attenuation term in Equation (2.48) is dominated by the scaling function. In both cases, the scaling function $\alpha(z)$ artificially increases the depth of the domain, which induces an accelerated amplitude decay of the wave within the PML layer. The scaling function $\alpha(z)$ reads

$$\alpha(z) = \begin{cases} 1 & 0 \le z \le Z_1, \\ 1 + \alpha_0 \left(\dfrac{z - Z_1}{H_{\mathrm{PML}}}\right)^{m_{\mathrm{PML}}} & Z_1 \le z \le Z_2. \end{cases} \tag{2.49}$$

On the other hand, the attenuation function $\beta(z)$ is written as

$$\beta(z) = \begin{cases} 0 & 0 \le z \le Z_1, \\ \beta_0 \left(\dfrac{z - Z_1}{H_{\mathrm{PML}}}\right)^{m_{\mathrm{PML}}} & Z_1 \le z \le Z_2. \end{cases} \tag{2.50}$$

where Z_1 and H_{PML} are the thicknesses of the two layers, β_0 and α_0 are tuning constants for scaling and attenuation functions, and m_{PML} is the order of the polynomial attenuation inside the PML domain.

When considering the attenuation of propagating wave only, the following complex-valued coordinate $\bar{z}$ can be given by neglecting the scaling tuning α_0 [19]:

$$\bar{z} = z - \mathrm{i}\mathrm{H}(z - Z_1)\frac{\beta_0 H_{\mathrm{PML}}}{\omega\,(m_{\mathrm{PML}} + 1)}\left(\frac{z - Z_1}{H_{\mathrm{PML}}}\right)^{m_{\mathrm{PML}}+1} \tag{2.51}$$

where $\mathrm{H}(\cdot)$ is the Heaviside function.

The polynomial order m_{PML} determines the attenuation function profile. A larger m_{PML} creates a smoother transition at the PML-regular domain interface, as well as a sharper attenuation near the fixed boundary [13]. This allows incoming waves to enter the PML smoothly before being attenuated. In the existing research, $m_{\mathrm{PML}} = 2$ is typically used for finite element and thin-layer methods [4, 13], as higher-order functions, namely, quadratic or cubic $\varepsilon(z)$, effectively minimize boundary reflections in discrete solutions [18]. However, the influence of m_{PML} in continuous solutions remains unstudied.
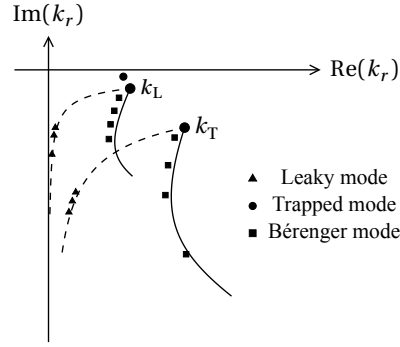
Figure 2.10. Indicative modes of *lossy elastic halfspace* truncated by single-layer PML, the dashed line stands for the $\mathscr{C}_{\text{branch}}$ in Equation (2.34) of the elastic halfspace and the solid lines are the new branches $\mathscr{C}_{\text{PML}}$ in [9]

When a finite PML is used to truncate the *elastic halfspace*, leaky modes will appear to compensate for the contribution of continuous radiated modes in Equation (2.34). Therefore, a new type of mathematical model will appear [4], which is called Bérenger modes, which is

$$\widetilde{\Phi} \simeq \sum \text{Trapped Modes} + \sum \text{Leaky Modes} + \sum \text{Bérenger Modes} \tag{2.52}$$

Overall, for the elastic halfspace with PMLs, the eigenvalues will contain both trapped modes, evanescent modes, and Bérenger modes. The characteristics of these three types of modes for the Pekiris waveguides have been studied [26]. What is more, it has been pointed out that, except for discrete points, a new branch cut $\mathscr{C}_{\text{PML}}$ would appear for the regular domain with *an infinite PML* [9]. Therefore, the modal basis can be expressed as:

$$\widetilde{\Phi} \simeq \sum \text{Trapped Modes} + \sum \text{Leaky Modes} + \int\limits_{\mathscr{C}_{\text{PML}}} \text{Bérenger Modes} \tag{2.53}$$

The energy of all discrete modes is trapped inside the domain if a rigid boundary is applied [23]. Therefore, the modal contribution for *a single regular layer with a finite PML layer*, the continuous radiation modes in Equation (2.52) will be replaced by (2.52) These Bérenger modes should be distributed along the hyperbolic branch $\mathscr{C}_{\text{PML}}$[9], as illustrated in Figure 2.10.

Existing research on the orthogonality of modes for continuous solutions in acoustic or elastic domains with PMLs remains limited: According to [4], these leaky modes represent non-physical solutions that continuously radiate energy into the lower halfspace; therefore, the orthogonality property will not be valid due to the infinite energy of the modes. [26] examined Pekeris waveguide systems with a PML. While the modes do not directly satisfy cross-orthogonality conditions, orthogonality can be established through the construction of conjugate (adjoint) eigenmodes, leveraging the special properties of the boundary conditions and the Helmholtz equation operator.

For the same physical problem, it is reasonable to expect that discrete and continuous solutions would exhibit similar modal characteristics. Discrete solutions obtained through the TLM method have been demonstrated to satisfy orthogonality; thus, continuous solutions describing the same system should, in principle, preserve this property. Moreover, for a finite PML with fixed boundaries, no energy leakage occurs into the lower halfspace, suggesting that orthogonality between leaky modes and trapped modes should remain valid. However, the validity of these assumptions for continuous solutions has not been systematically examined in the literature, thereby motivating the comparative analysis between continuous and discrete formulations conducted in this thesis.

2.8 Thin-Layer Method (TLM)

In this section, a brief introduction to the Thin-Layer Method (TLM) will be presented. The thin-layered method is an effective semi-discrete numerical approach for wave motion in layered media. As a discrete form of normal mode solution, TLM was initially developed in the early 1970s, and it has been commonly used in acoustic, elastic, and acousto-elastic problems since the 1990s [4]. Besides, TLM was limited to bounded domains with rigid boundaries, and nowadays TLMs have been used in the simulation of unbounded domains after the availability of PMLs and paraxial boundaries. A brief history of TLM can be found in [15].

Generally, the key concept of TLM is the partial discretization of the domain along the layering direction. In a 2D problem, A finite element discretization will be implemented along a spatial direction, while analytical solutions will be used in the remaining directions. For an axisymmetric linear elastic isotropic halfspace without body force, the Equation of motion can be expressed in the matrix form in the cylindrical coordinates (r, θ, z):

$$\mathbf{L}_\sigma^T \boldsymbol{\sigma}_s - \rho_s \ddot{\mathbf{u}}_s = 0, \tag{2.54}$$

where $\mathbf{u}_s$ is the displacement vector and $\boldsymbol{\sigma}_s$ is the stress tensor.

Using virtual work principle, the final elementary layer matrices $\mathbf{A}_\ell$, $\mathbf{G}_\ell$ and $\mathbf{M}_\ell$ can be derived as follows [4]:

$$\mathbf{A}_\ell = h_\ell \begin{bmatrix} \cdot & & \\ & \cdot & \\ & & \cdot \end{bmatrix}, \quad \mathbf{G}_\ell = h_\ell^{-1} \begin{bmatrix} \cdot & & \\ & \cdot & \\ & & \cdot \end{bmatrix}, \quad \mathbf{M}_\ell = h_\ell \begin{bmatrix} \cdot & & \\ & \cdot & \\ & & \cdot \end{bmatrix}. \tag{2.55}$$

However, the $\mathbf{B}_\ell$ is not dependent on the element thickness h_ℓ. Finally, the following matrix equation of the eigenvalue problem will be derived after matrix assembly:

$$\left(k_{rp}^2 \mathbf{A} + k_{rp} \mathbf{B} + \mathbf{G} - \omega^2 \mathbf{M} \right) \boldsymbol{\phi}_p = \mathbf{0} \tag{2.56}$$

where $\mathbf{A}$, $\mathbf{M}$ and $\mathbf{G}$ are symmetric. However, $\mathbf{B}$ is not symmetric, with the following structure:

$$\mathbf{B} = \begin{bmatrix} \mathbf{0} & \mathbf{0} & \mathbf{B}_{rz} \\ \mathbf{0} & \mathbf{0} & \mathbf{0} \\ \mathbf{B}_{zr} & \mathbf{0} & \mathbf{0} \end{bmatrix}. \tag{2.57}$$

The quadratic eigenvalue problem indicated by Equation (2.56) can be linearized and transformed to normal modes of Rayleigh and Love waves. On the one hand, for $P-SV$ modes, the following linear non-symmetric eigenvalue problem in k_{rm}^2 has been derived in [19]:

$$\left(k_{rp}^2 \overline{\mathbf{A}} + \overline{\mathbf{C}} \right) \begin{bmatrix} \boldsymbol{\phi}_{rp} \\ k_{rp} \boldsymbol{\phi}_{zp} \end{bmatrix} = \begin{bmatrix} \mathbf{0} \\ \mathbf{0} \end{bmatrix} \tag{2.58}$$

where $\overline{\mathbf{A}}$ and $\overline{\mathbf{C}}$ have the following form:

$$\overline{\mathbf{A}} = \begin{bmatrix} \mathbf{A}_r & \mathbf{0} \\ \mathbf{B}_{zr} & \mathbf{A}_z \end{bmatrix}; \quad \overline{\mathbf{C}} = \begin{bmatrix} \mathbf{G}_r - \omega^2 \mathbf{M}_r & \mathbf{B}_{rz} \\ \mathbf{0} & \mathbf{G}_z - \omega^2 \mathbf{M}_z \end{bmatrix} \tag{2.59}$$

On the other hand, the SH modes have the following linear symmetric eigenvalue problem in k^2:

$$\left(k_{rp}^2 \mathbf{A}_\theta + \mathbf{G}_\theta - \omega^2 \mathbf{M}_\theta \right) \boldsymbol{\phi}_{\theta p} = 0, \tag{2.60}$$

Where $\boldsymbol{\phi}_{rp}$, $\boldsymbol{\phi}_{\theta p}$ and $\boldsymbol{\phi}_{zp}$ are modal displacements at interfaces of thin layers in the radial, circumferential and vertical directions, evaluated at both the interfaces of each layer and the interpolation points within each layer. In this study, *quadratic interpolation polynomials* are employed for TLM, resulting in one interpolation point per layer.
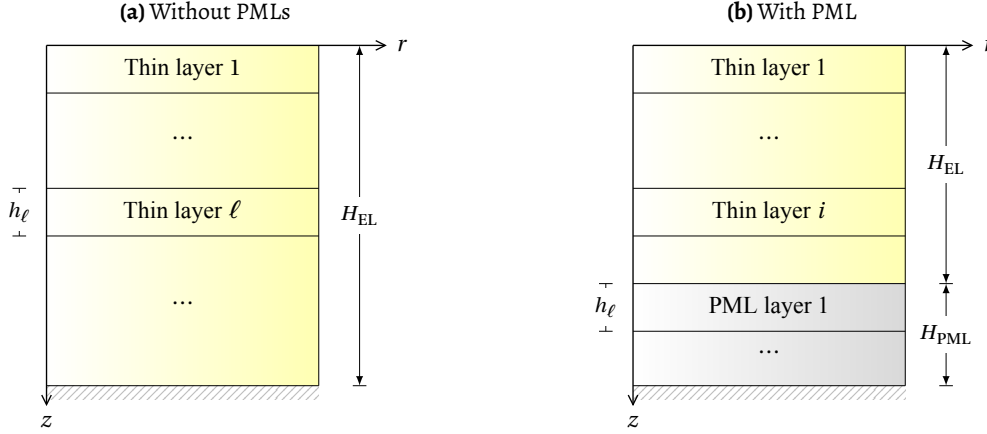
(a) Without PMLs

(b) With PML

Figure 2.11. Schematics of TLMs

Equation (2.58) can be written as:

$$\begin{bmatrix} \mathbf{A}_r k_{rp}^2 + \mathbf{G}_r - \omega^2 \mathbf{M}_r & \mathbf{B}_{rz} \\ \mathbf{B}_{zr} k_{rp}^2 & \mathbf{A}_z k_{rp}^2 + \mathbf{G}_r - \omega^2 \mathbf{M}_r \end{bmatrix} \begin{bmatrix} \boldsymbol{\phi}_{rp} \\ k_{rp} \boldsymbol{\phi}_{zp} \end{bmatrix} = \begin{bmatrix} \mathbf{0} \\ \mathbf{0} \end{bmatrix} \tag{2.61}$$

Alternatively, the Equation above can be written as:

$$\begin{bmatrix} \mathbf{A}_r k_{rp}^2 + \mathbf{G}_r - \omega^2 \mathbf{M}_r & \mathbf{B}_{rz} k_{rp}^2 \\ \mathbf{B}_{zr} & \mathbf{A}_z k_{rp}^2 + \mathbf{G}_r - \omega^2 \mathbf{M}_r \end{bmatrix} \begin{bmatrix} k_{rp} \boldsymbol{\phi}_{rp} \\ \boldsymbol{\phi}_{zp} \end{bmatrix} = \begin{bmatrix} \mathbf{0} \\ \mathbf{0} \end{bmatrix} \tag{2.62}$$

The *left and right eigenvectors* are defined as below:

$$\mathbf{Y} = \begin{bmatrix} \boldsymbol{\Phi}_r \mathbf{K}_r \\ \boldsymbol{\Phi}_z \end{bmatrix}, \qquad \mathbf{Z} = \begin{bmatrix} \boldsymbol{\Phi}_r \\ \boldsymbol{\Phi}_z \mathbf{K}_r \end{bmatrix}. \tag{2.63}$$

where $\mathbf{K}_r = \mathrm{diag}\{ k_{r1} \quad k_{r2} \cdots \}$ is the diagonal matrix computed from sorted eigen wavenumber k_{rp} associated with *P-SV* modes. Furthermore, $\boldsymbol{\Phi}_r$ and $\boldsymbol{\Phi}_z$ are modal matrices with the following form:

$$\boldsymbol{\Phi}_r = \begin{bmatrix} \boldsymbol{\phi}_{r1} & \boldsymbol{\phi}_{r2} & \cdots \end{bmatrix}, \qquad \boldsymbol{\Phi}_z = \begin{bmatrix} \boldsymbol{\phi}_{z1} & \boldsymbol{\phi}_{z2} & \cdots \end{bmatrix}. \tag{2.64}$$

Therefore, Equations (2.61) and (2.62) read:

$$\overline{\mathbf{A}} \mathbf{Z} \mathbf{K}_r^2 + \overline{\mathbf{C}} \mathbf{Z} = \mathbf{0} \qquad \overline{\mathbf{A}}^T \mathbf{Y} \mathbf{K}_r^2 + \overline{\mathbf{C}}^T \mathbf{Y} = \mathbf{0} \tag{2.65}$$

Therefore, we have the following normal orthogonality relations:

$$\mathbf{Y}^T \overline{\mathbf{A}} \mathbf{Z} = \mathbf{Z}^T \overline{\mathbf{A}}^T \mathbf{Y} = \mathbf{K}_r \qquad \mathbf{Y}^T \overline{\mathbf{C}} \mathbf{Z} = \mathbf{Z}^T \overline{\mathbf{C}}^T \mathbf{Y} = -\mathbf{K}_r^3 \tag{2.66}$$

Following the implementations introduced by Kausel and de Oliveira Barbosa, the layer thickness in the PML layer should be modified after complex stretch in Equation (2.51), which is:

$$\bar{h}_\ell = \bar{z}_\ell - \bar{z}_{\ell-1} = H \left\{ \frac{1}{N_{\mathrm{PML}}} - \mathrm{i}\Omega \left[\left(\frac{\ell}{N_{\mathrm{PML}}} \right)^{m_{\mathrm{PML}}+1} - \left(\frac{\ell-1}{N_{\mathrm{PML}}} \right)^{m_{\mathrm{PML}}+1} \right] \right\}, \tag{2.67}$$

where $\Omega = \dfrac{\beta_0}{\omega \left(m_{\mathrm{PML}} + 1 \right)}$.

According to Equation (2.55), elemental matrix for ℓ–th layer in PML domain should be modified as:

$$\overline{\mathbf{A}}_\ell = \frac{\bar{h}_\ell}{h_\ell} \mathbf{A}_\ell, \quad \overline{\mathbf{G}}_\ell = \frac{h_\ell}{\bar{h}_\ell} \mathbf{G}_\ell, \quad \overline{\mathbf{M}}_\ell = \frac{\bar{h}_\ell}{h_\ell} \mathbf{A}_\ell, \quad \overline{\mathbf{B}}_\ell = \mathbf{B}_\ell \tag{2.68}$$

Therefore, a new version of generalized eigenvalue problems of *SH* and *P*−*SV* waves should be derived for layered elastic media with PMLs.

<div style="text-align: right">
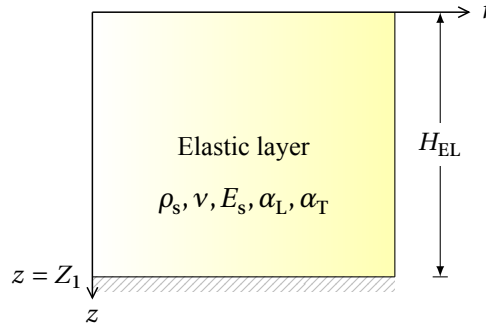
3

</div>

Modal Solutions of an Elastic Waveguide

Figure 3.1. Schematic of single elastic layer

Table 3.1. Basic parameters used for numerical examples in Chapter 3

Elastic layer thickness	H_{EL}	10	m
Solid density upper layer	ρ_s	1700	kg/m^3
Poisson's ratio	ν	0.4	-
Young's modulus	E_s	0.7	MPa

This chapter will perform a comparative study between the continuous and discrete solutions of the single elastic layer with a fixed bottom boundary. The elastic layer illustrated in Figure 3.1 will be solved using the normal mode method, with all dimensions given in Table 3.1. The methodology of this chapter consists of the following steps:

{3.1} Formulate the eigenvalue problem for both semi-analytical and TLM solutions. This chapter briefly introduces the mathematical derivations, while a detailed derivation will be given in Appendix A for readers interested in semi-analytical solutions.

{3.2} Solve eigen-value problems for three different loading frequencies for the elastic layer with zero and non-zero attenuation.

{3.3} Compare the eigenvalues (roots) and eigenvectors (mode shapes) of the discrete and continuous solutions.

{3.4} Check the orthogonality of eigenvectors from two different approaches.

3.1 Formulation of eigenvalue problems

3.1.1 Continuous solution

We start with the Helmholtz equations for the Rayleigh (PSV) waves in the single elastic layer:

$$\nabla^2 \widetilde{\phi}_s + k_L^2 \widetilde{\phi}_s = 0, \tag{3.1}$$

$$\nabla^2 \widetilde{\psi}_s - \frac{\widetilde{\psi}_s}{r^2} + k_T^2 \widetilde{\psi}_s = 0. \tag{3.2}$$

where $\phi_s(r,z)$ and $\psi_s(r,z)$ represent the potential field for P and S waves, and tildes over them denote the complex amplitude in the frequency domain. Additionally, k_L and k_T are the P-wavenumber and S-wavenumber, respectively, with the following expressions:

$$k_L = \omega/c_L, \qquad\qquad\qquad k_T = \omega/c_T. \tag{3.3}$$

in which c_L and c_T denote the speeds of the compressional and shear waves in the elastic waveguide, respectively. In addition, a set of boundary conditions for the system in Figure 3.1 must be satisfied:

$$\widetilde{\sigma}_{zz}(r,0,\omega) = 0 \qquad\qquad \widetilde{\sigma}_{zr}(r,0,\omega) = 0 \tag{3.4}$$

$$\widetilde{u}_{s,z}(r,Z_1,\omega) = 0 \qquad\qquad \widetilde{u}_{s,r}(r,Z_1,\omega) = 0 \tag{3.5}$$

The general solutions of Equation (3.1) and (3.2)are given as below:

$$\widetilde{\phi}_s(r,z,\omega) = \widetilde{\Phi}_s(z,\omega) H_0^{(2)}(k_r r) = \left[A_1 \exp\left(i\gamma_L z\right) + A_2 \exp\left(-i\gamma_L z\right) \right] H_0^{(2)}(k_r r) \tag{3.6}$$

$$\widetilde{\psi}_s(r,z,\omega) = \widetilde{\Psi}_s(z,\omega) H_1^{(2)}(k_r r) = \left[A_3 \exp\left(i\gamma_T z\right) + A_4 \exp\left(-i\gamma_T z\right) \right] H_1^{(2)}(k_r r), \tag{3.7}$$

where $\widetilde{\Phi}_s(z,\omega)$ and $\widetilde{\Psi}_s(z,\omega)$ are normal modes that are related to P and S waves. Besides, γ_T and γ_L are vertical wavenumbers with the following expressions:

$$\gamma_L = \sqrt{\omega^2/c_L^2 - k_r^2} \qquad\qquad \gamma_T = \sqrt{\omega^2/c_T^2 - k_r^2}. \tag{3.8}$$

Rewrite the normal modes as below to maintain numerical stability:

$$\widetilde{\Phi}_s(z,\omega) = A_1 \exp\left[-i\gamma_L\left(z - Z_1\right) \right] + A_2 \exp\left(i\gamma_T z\right), \tag{3.9}$$

$$\widetilde{\Psi}_s(z,\omega) = A_3 \exp\left[-i\gamma_T\left(z - Z_1\right) \right] + A_4 \exp\left(i\gamma_T z\right), \tag{3.10}$$

The displacement of soil particles $\widetilde{u}_{s,r}$ and $\widetilde{u}_{s,r}$ are given as below based on Equation (2.13):

$$\widetilde{u}_{s,r} = H_1^{(2)}(k_r r) \left[-k_r\left(A_1 \exp\left(i\gamma_L\left(Z_1 - z\right)\right) + A_2 \exp\left(i\gamma_L z\right) \right) \right.$$
$$\left. + i\gamma_T\left(A_3 \exp\left(i\gamma_T\left(z - Z_1\right)\right) - A_4 \exp\left(i\gamma_T z\right) \right) \right]. \tag{3.11}$$

$$\widetilde{u}_{s,z} = H_0^{(2)}(k_r r) \left[k_r\left(A_{2,1} \exp\left(i\gamma_T\left(Z_1 - z\right)\right) + A_{2,2} \exp\left(i\gamma_T z\right) \right) \right.$$
$$\left. + i\gamma_L\left(-A_{1,1} \exp\left[i\gamma_L\left(Z_1 - z\right)\right] + A_{1,2} \exp\left(-i\gamma_L z\right) \right) \right]. \tag{3.12}$$

The following formulae give the stress fields:

$$\tilde{\sigma}_{s,zz} = H_0^{(2)}(k_r r)\left[2\mu_s k_r \gamma_T \mathrm{i}\left(-A_{2,1}\exp\left(\mathrm{i}\gamma_T(Z_1-z)\right)+A_{2,2}\exp\left(\mathrm{i}\gamma_T z\right)\right)\right.$$

$$\left.-\left(\lambda_s k_L^2 + 2\mu_s\gamma_L^2\right)\left(A_{1,1}\exp\left(\mathrm{i}\gamma_L(Z_1-z)\right)+A_{1,2}\exp\left(\mathrm{i}\gamma_L z\right)\right)\right]. \tag{3.13}$$

$$\tilde{\sigma}_{s,zr} = H_1^{(2)}(k_r r)\mu_s\left[\left(\gamma_T^2 - k_r^2\right)\left(A_{2,1}\exp\left(\mathrm{i}\gamma_T(z-Z_1)\right)+A_{2,2}\exp\left(-\mathrm{i}\gamma_T z\right)\right)\right.$$

$$\left.+\left(\mathrm{i}k_r\gamma_L\right)\left(A_{1,1}\exp\left(\mathrm{i}\gamma_L(z-Z_1)\right)+A_{1,2}\exp\left(\mathrm{i}\gamma_L z\right)\right)\right]. \tag{3.14}$$

The substitution of all fields into the boundary conditions gives the coefficient matrix $\mathbf{M}$ as shown in Equation (A.1). therefore gives the dispersion relation

$$\det \mathbf{M} = 0. \tag{3.15}$$

The roots of dispersion relations in the complex k_r plane give all eigenvalues k_r. Based on these roots, the eigenvectors $\Phi_s(z)$ and $\Psi_s(z)$ will be computed by imposing an inhomogeneous displacement at the bottom boundary.

3.1.2 Discrete solution

Briefly, the generalized discrete eigenvalue problem of P-SV modes in the elastic waveguide is given in the following form using TLM [12]:

$$\left(k_{rp}^2\overline{\mathbf{A}}+\overline{\mathbf{C}}\right)\left[\begin{array}{c}\boldsymbol{\phi}_{rp}\\k_{rp}\boldsymbol{\phi}_{zp}\end{array}\right]=\left[\begin{array}{c}\mathbf{0}\\\mathbf{0}\end{array}\right] \tag{3.16}$$

where here $\boldsymbol{\phi}_{rp}$, $\boldsymbol{\phi}_{zp}$ are modal displacements at interfaces of thin layers in the radial and vertical directions. $\overline{\mathbf{A}}$ and $\overline{\mathbf{C}}$ have the following form:

$$\overline{\mathbf{A}}=\left[\begin{array}{cc}\mathbf{A}_r & \mathbf{0}\\\mathbf{B}_{zr} & \mathbf{A}_z\end{array}\right];\qquad \overline{\mathbf{C}}=\left[\begin{array}{cc}\mathbf{G}_r - \omega^2\mathbf{M}_r & \mathbf{B}_{rz}\\\mathbf{0} & \mathbf{G}_z - \omega^2\mathbf{M}_z\end{array}\right] \tag{3.17}$$

Define the left eigenvector $\mathbf{Y}$ and right eigenvector $\mathbf{Z}$ as below:

$$\mathbf{Y}=\left[\begin{array}{c}\boldsymbol{\Phi}_r\mathbf{K}_r\\\boldsymbol{\Phi}_z\end{array}\right],\qquad \mathbf{Z}=\left[\begin{array}{c}\boldsymbol{\Phi}_r\\\boldsymbol{\Phi}_z\mathbf{K}_r\end{array}\right]. \tag{3.18}$$

where $\mathbf{K}_r = \mathrm{diag}\{k_{r1}\quad k_{r2}\cdots\}$ is the diagonal matrix computed from sorted eigen wavenumber k_{rp} associated with P-SV modes. Furthermore, $\boldsymbol{\Phi}_r$ and $\boldsymbol{\Phi}_z$ are modal matrices with the following form:

$$\boldsymbol{\Phi}_r = \left[\begin{array}{ccc}\boldsymbol{\phi}_{r1} & \boldsymbol{\phi}_{r2} & \cdots\end{array}\right],\qquad \boldsymbol{\Phi}_z = \left[\begin{array}{ccc}\boldsymbol{\phi}_{z1} & \boldsymbol{\phi}_{z2} & \cdots\end{array}\right]. \tag{3.19}$$

Then we have the following eigenvalue problem based on $\mathbf{Y}$ and $\mathbf{Z}$:

$$\mathbf{Y}^T\overline{\mathbf{A}}\mathbf{K}_r^2 + \mathbf{Y}^T\overline{\mathbf{C}}\mathbf{Z} = \mathbf{0} \tag{3.20}$$

Therefore, $\mathbf{Y}$ and $\mathbf{Z}$ are supposed to have the following orthogonality relations, which have been proved by Waas and Kausel [12]:

$$\mathbf{Y}^T\overline{\mathbf{A}}\mathbf{Z} = \mathbf{K}_r,\quad \mathbf{Y}^T\overline{\mathbf{C}}\mathbf{Z} = -\mathbf{K}_r^3 \tag{3.21}$$

The eigenvalues k_{rp} and unnormalized eigenvectors are directly given by solving the eigenvalue problem shown in Equation (3.16), which can be solved easily using the inbuilt function `np.linalg.eig` in Python. Returned eigenvectors will be normalized by the orthogonality relation $\mathbf{Y}^T\overline{\mathbf{A}}\mathbf{Z} = \mathbf{K}_r$. Besides, the roots with positive imaginary part will be discarded to select the mode that decays in the range [12]. Implementations of all steps mentioned here have been done in the programming language Python. A detailed explanation of the Thin layer method can be found in [19].

3.2　Numerical results and discussions

In this section, the continuous and discrete modal solutions of a linear isotropic elastic layer will be compared, including their (1) eigenvalues, (2) eigenvectors, and (3) orthogonality. For completeness, we will show modal solutions for $f = 50\,\text{Hz}$, $f = 200\,\text{Hz}$, and $f = 500\,\text{Hz}$. Additionally, different attenuation rates α_s in the continuous solution, which correspond to material damping ξ_s in the discrete solution, will be considered.

Table 3.2. Fixed parameters of the Thin-layer method used in Chapter 3

Number of thin layers	N	1000	-
Layer thickness	h_ℓ	0.01	m

Table 3.3. Attenuation rates and frequencies used in six cases in Chapter 3

Groups	Attenuation rate			Frequency		
Group 1.1	α_s	0	dB/λ	f	50	Hz
Group 1.2	α_s	1	dB/λ	f	50	Hz
Group 2.1	α_s	0	dB/λ	f	200	Hz
Group 2.2	α_s	1	dB/λ	f	200	Hz
Group 3.1	α_s	0	dB/λ	f	500	Hz
Group 3.2	α_s	1	dB/λ	f	500	Hz

3.2.1　Parameter setup

In addition to the parameters displayed in Table 3.1, the fixed parameters used in the thin-layered method are shown in Table 3.2. However, the attenuation rates of elastic media in TLMs and the semi-analytical solution are defined in slightly different ways. Here we will briefly introduce a consistent way of defining them.

In the semi-analytical solution, the attenuation is defined in terms of the wave speed. Let us use c_L as an example:

$$c_L = \frac{\text{Re}(c_L)}{1 - i\eta} \tag{3.22}$$

where the attenuation coefficient $\eta = \alpha_s/(40\pi \log e)$, and α_s represents the attenuation rate of the elastic layer in dB/λ. However, the elastic damping ratio ξ_s in the TLM is incorporated through complex-valued Lamé constants [19]:

$$\lambda_s^* = \lambda_s\Big(1 + 2i\xi_s\,\text{sgn}(\omega)\Big) \text{ and } \mu_s^* = \mu_s\Big(1 + 2i\xi_s\,\text{sgn}(\omega)\Big). \tag{3.23}$$

They are used to calculate the complex-valued wave speeds using Equation (2.20); therefore, we can match α_s and ξ_s based on wave speeds. The calculation of complex-valued wave speeds in semi-analytical solutions is introduced in the first section of Appendix A for interested readers. Here we directly provide the mapping between ξ_s and α:

$$\xi_s = \left| \frac{1 - \big(1 - \alpha_s i/(40\pi \log e)\big)^2}{2i\big(1 - \alpha_s i/(40\pi \log e)\big)^2} \right|. \tag{3.24}$$

Note that in this chapter, we assume identical attenuation rates for both P and S waves:

$$\alpha_T = \alpha_L = \alpha_s. \tag{3.25}$$

Finally, six cases have been designed based on different frequencies and attenuation levels, as presented in Table 3.3.
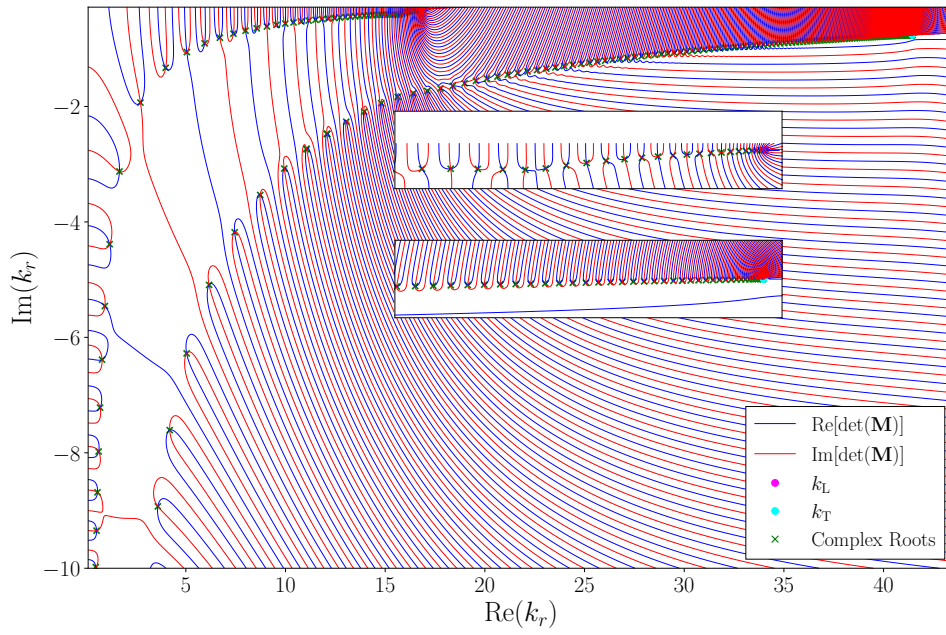
Figure 3.2. Zero contour plots of real and imaginary parts of Equation (3.15) and roots when $\alpha_s = 1\,\mathrm{dB}/\lambda$ and $f = 800\mathrm{Hz}$.

3.2.2 Eigenvalues

The algorithm is designed to locate the roots of the dispersion relation given in Equation (3.15). The underlying principles of the algorithm, as applied to both elastic and acousto-elastic layers, are discussed in detail in [20]. Briefly, the algorithm proceeds according to the following steps:

{1} **Counting**: Based on the principle of the argument, first count the total number of roots of the dispersion relation for given regions.

{2} **Subdivision**: Subdivide the region into smaller regions with a limited number of roots based on the principle of the argument method.

{3} **Polishing**: Refine the location of roots by minimizing the modulus of det **M** for each subdivision.

The roots and zero-contour plots of Equation (3.15), computed by the root-finder for $f = 800\,\mathrm{Hz}$ with $\alpha_s = 1$, are shown in Figure 3.2. The plots indicate that all roots located at the intersections of the real (blue line) and imaginary parts (red line) of the dispersion relation have been successfully identified. This demonstrates the effectiveness of the root-finder.

Figure 3.3 presents six subfigures comparing the roots obtained from the semi-analytical and TLM eigenvalue problems, corresponding to all cases defined in Table 3.3. The following observations can be noticed:

1. When the medium is *lossless* ($\alpha_s = 0$), the roots are symmetrically distributed in the third and fourth quadrant. However, this symmetry is violated in the presence of attenuation ($\alpha_s > 0$). For all cases, the roots move from an evanescent region near the imaginary axis to the real axis with increasing frequency, reflecting that more modes become propagative at higher frequencies.

2. The roots of the continuous and discrete solutions match closely at 50 and 200 Hz. At 500 Hz, small deviations appear, mainly due to the discrete solution having a finite number of modes set by the system matrix size, whereas the continuous formulation admits infinitely many modes. Increasing the number of thin layers in the TLM could reduce this gap but at a higher computational cost. Overall, both approaches agree well on the number and location of roots in the complex plane.
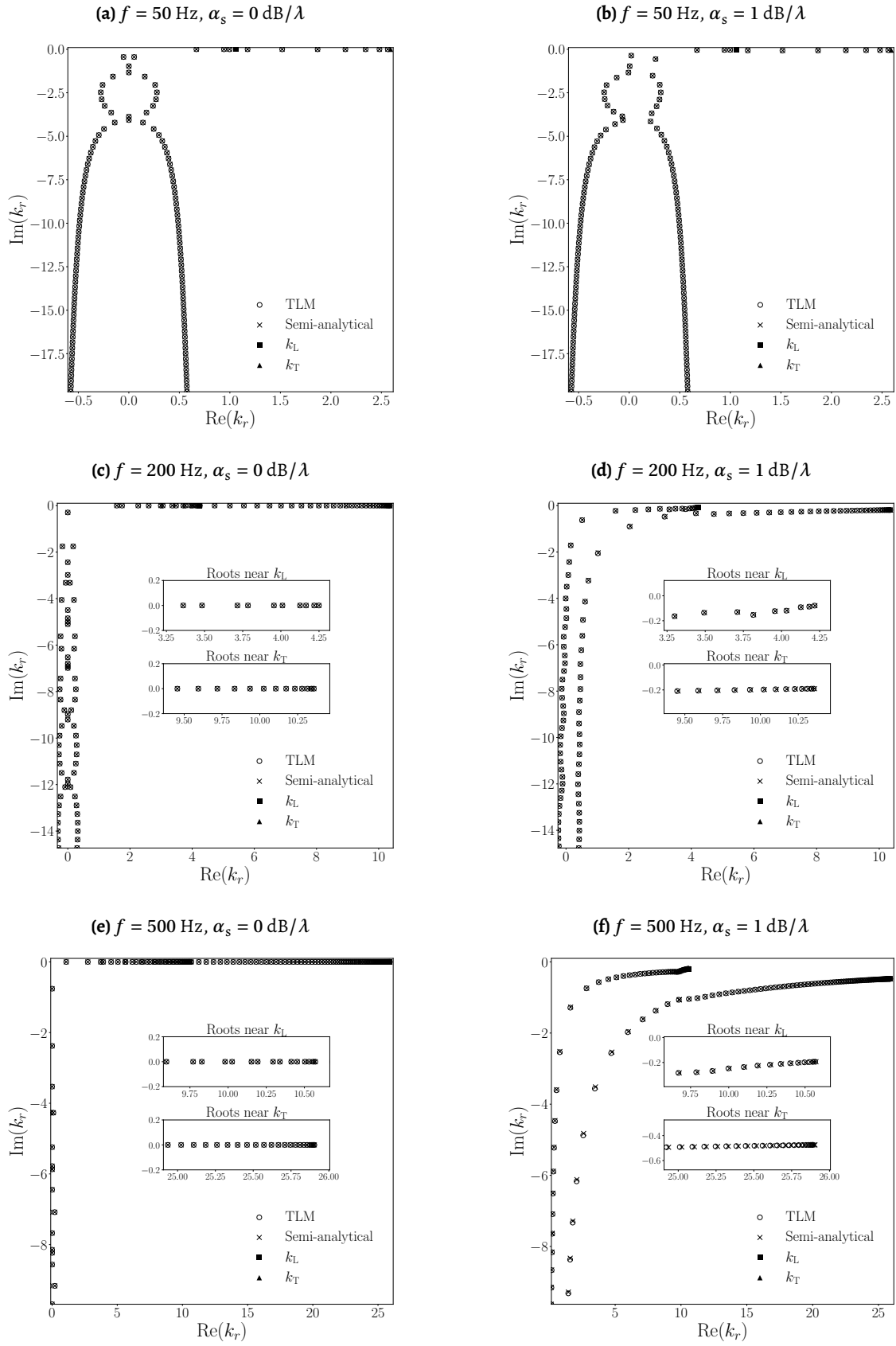
(a) $f = 50$ Hz, $\alpha_s = 0$ dB$/\lambda$

(b) $f = 50$ Hz, $\alpha_s = 1$ dB$/\lambda$

(c) $f = 200$ Hz, $\alpha_s = 0$ dB$/\lambda$

(d) $f = 200$ Hz, $\alpha_s = 1$ dB$/\lambda$

(e) $f = 500$ Hz, $\alpha_s = 0$ dB$/\lambda$

(f) $f = 500$ Hz, $\alpha_s = 1$ dB$/\lambda$

Figure 3.3. Comparison of eigenvalues from the discrete and continuous solutions for all groups listed in Table 3.3.

3.2.3 Eigenvectors

Eigenvectors from discrete and continuous eigenvalue problems are normalized based on orthogonality. In the thin-layer method, the left and right eigenvectors are normalized using the relation $\mathbf{Y}^T \mathbf{A} \mathbf{Z} = \mathbf{K}_r$. The normalization of the semi-analytical solution follows the orthogonality relation (2.38). This section compares different types of modes at 50 Hz and 500 Hz; additional results are provided in Appendix C.

SV wave type modes

Normalized SV wave type modes from both approaches , with k_r close to k_T, will be compared in the six subfigures of Figure 3.4, modes from two methods are consistent.

(a) $f = 50\,\text{Hz}$, $\alpha_s = 1\,\text{dB}/\lambda$, $k_r = 2.56 - 0.05\text{i}$

(b) $f = 500\,\text{Hz}$, $\alpha_s = 1\,\text{dB}/\lambda$, $k_r = 25.90 - 0.47\text{i}$
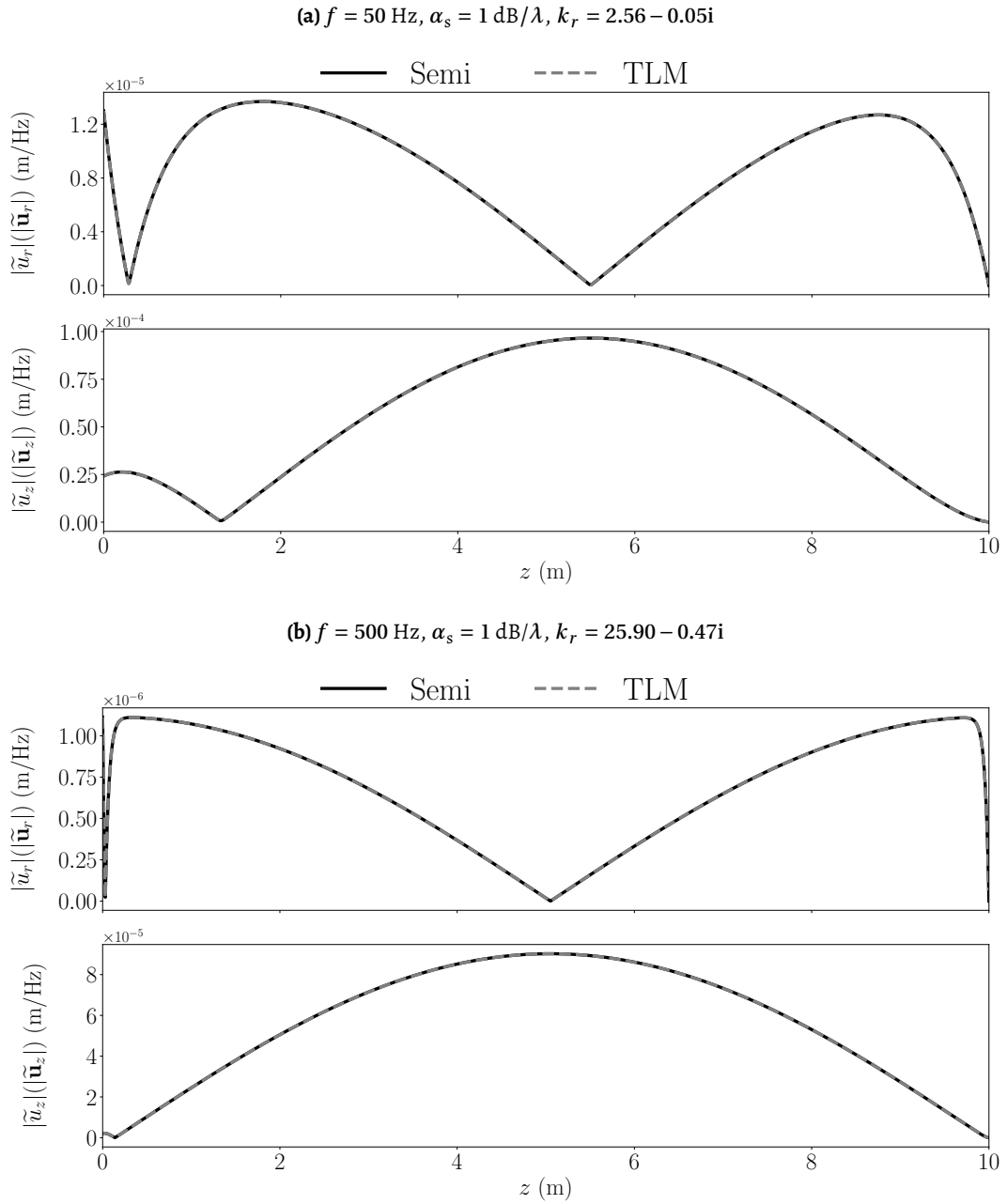

Figure 3.4. Comparison of selected normalized SV-wave type modes obtained from semi-analytical (black-continuous line) and TLM solutions (grey-dashed line) for different cases: (a) $f = 50\,\text{Hz}$, $\alpha_s = 1\,\text{dB}/\lambda$, (b) $f = 500\,\text{Hz}$, $\alpha_s = 1\,\text{dB}/\lambda$.

P wave type modes

In the next stage, normalized modes with k_r close to k_L will be compared. As shown in the following six subfigures, the modal shapes from both approaches agree well. Furthermore, these modes exhibit strong vertical oscillations, suggesting their energy propagates vertically.
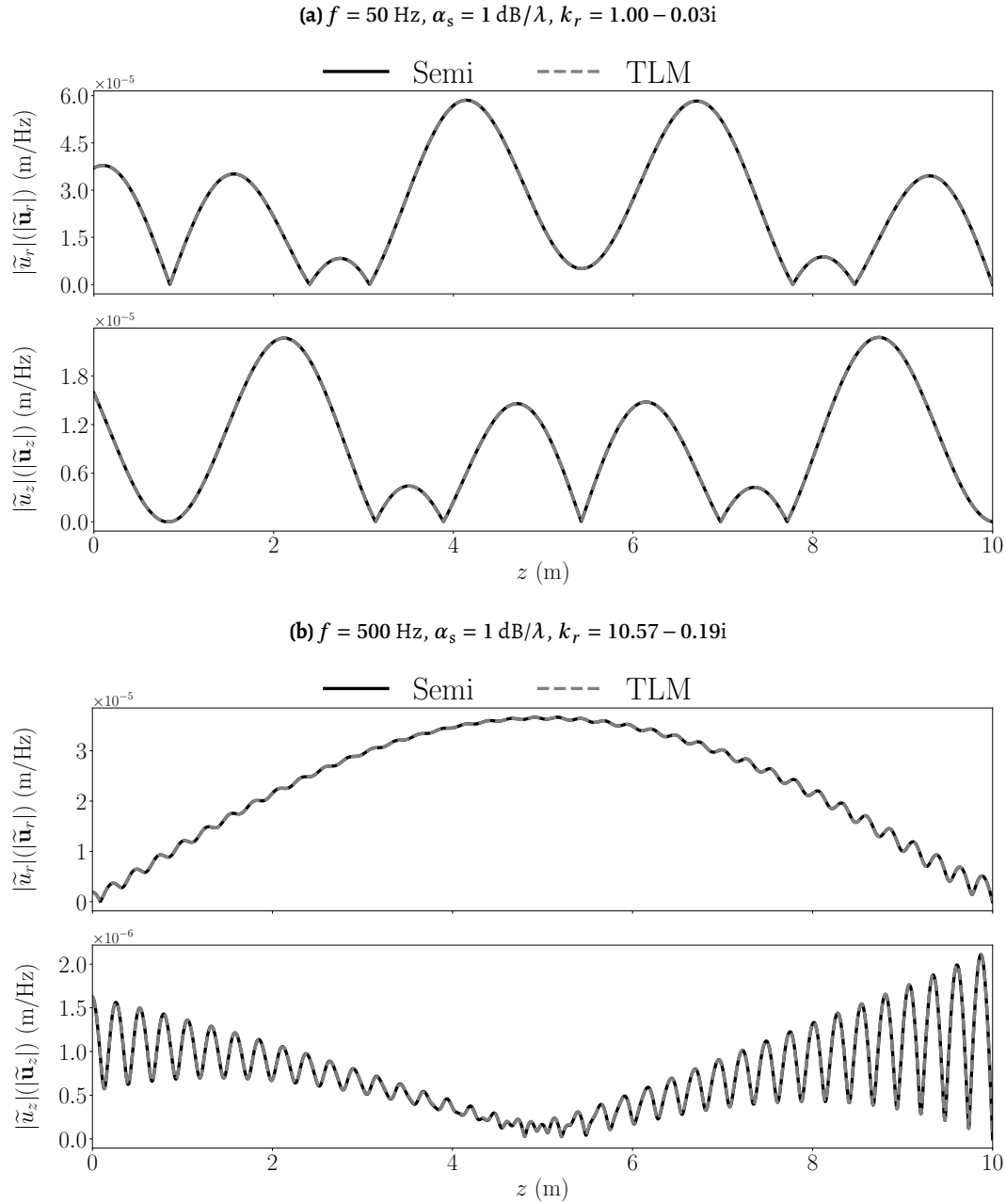
(a) $f = 50$ Hz, $\alpha_s = 1$ dB$/\lambda$, $k_r = 1.00 - 0.03$i

(b) $f = 500$ Hz, $\alpha_s = 1$ dB$/\lambda$, $k_r = 10.57 - 0.19$i

Figure 3.5. Comparison of selected normalized P-wave type modes obtained from semi-analytical (black-continuous line) and TLM solutions (grey-dashed line) for different cases: (a) $f = 50$ Hz, $\alpha_s = 1$ dB$/\lambda$, (b) $f = 500$ Hz, $\alpha_s = 1$ dB$/\lambda$.

Evanescent modes

Finally, we compared normalized modes with radial wavenumbers k_r that have large imaginary parts, resulting in rapid decay in the radial direction. Nevertheless, the spectrum of such evanescent modes is essential for accurately capturing near-field wave propagation and structure–soil–fluid interaction [20]. The six subfigures in Figure 3.6 show that the evanescent modes obtained from the two approaches are in close agreement.
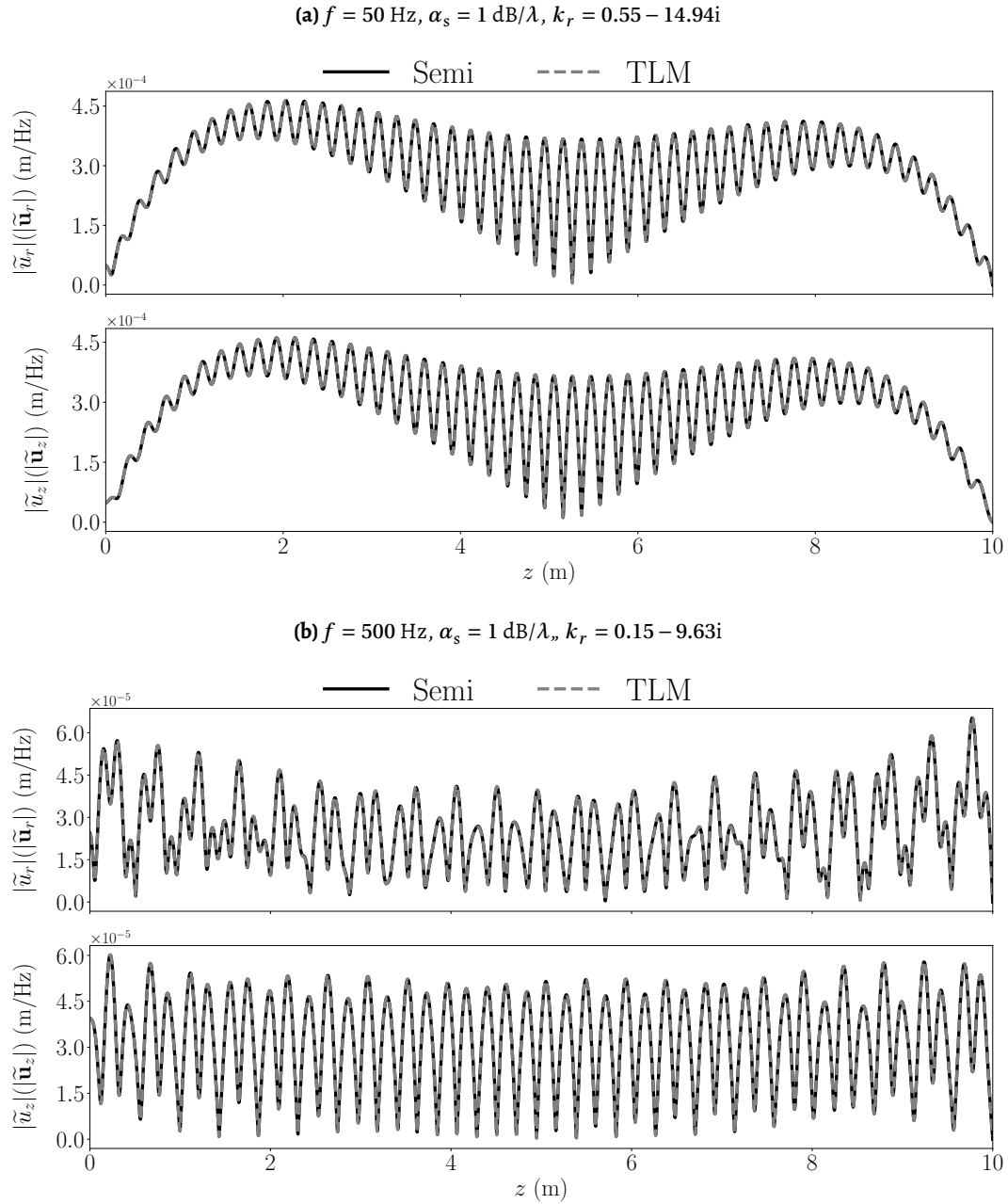
(a) $f = 50$ Hz, $\alpha_s = 1$ dB/λ, $k_r = 0.55 - 14.94$i

(b) $f = 500$ Hz, $\alpha_s = 1$ dB/λ, $k_r = 0.15 - 9.63$i

Figure 3.6. Comparison of selected normalized Evanescent wave type modes obtained from semi-analytical (black-continuous line) and TLM solutions (grey-dashed line) for different cases: (a) $f = 50$ Hz, $\alpha_s = 1$ dB/λ, (f) $f = 500$ Hz, $\alpha_s = 1$ dB/λ.

3.2.4 Orthogonality

Figures 3.7 and 3.8 show the orthogonality conditions of normalized eigenvectors for the elastic layer, both with and without dissipation, using continuous and discrete solutions. In each set of six subfigures, the left column displays the values $|\Gamma_{pq}|$ for the first three hundred normalized modes from the continuous solution, whereas the right column presents $\log_{10}|\Gamma_{pq}|$ for the first five hundred modes obtained from the discrete solution. The vertical axis corresponds to mode number p, and the horizontal axis to mode number q. In all cases, the off-diagonal terms are zero, indicating that the modes are orthogonal.

3.3 Summary

In this chapter, the continuous and discrete modal solutions of the elastic waveguide shown in Figure 3.1 have been compared. The primary conclusions are summarized as follows:

1. The eigenvalues obtained from the discrete and continuous solutions are consistent across various combinations of frequency f and attenuation rate α_s.

2. Different types of normalized eigenvectors—namely, P-wave type, SV-wave type, and evanescent modes—computed from the two methods agree well.

3. The modal orthogonality relations derived from both approaches remain valid for different combinations of frequency f and attenuation rate α_s.
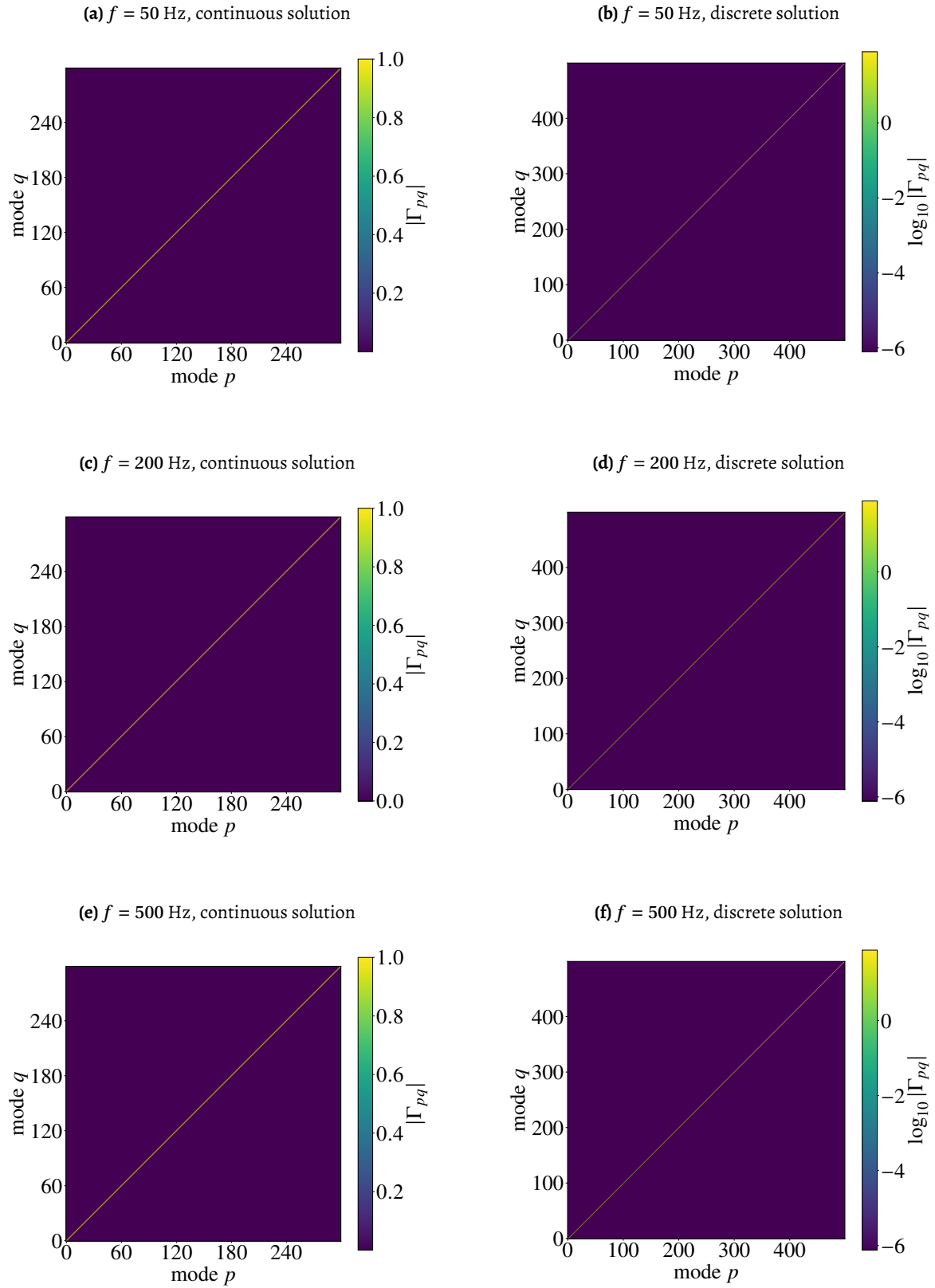
Figure 3.7. Comparison of eigenvector orthogonality between the continuous and discrete solutions for $\alpha_s = 0\,\mathrm{dB}/\lambda..$
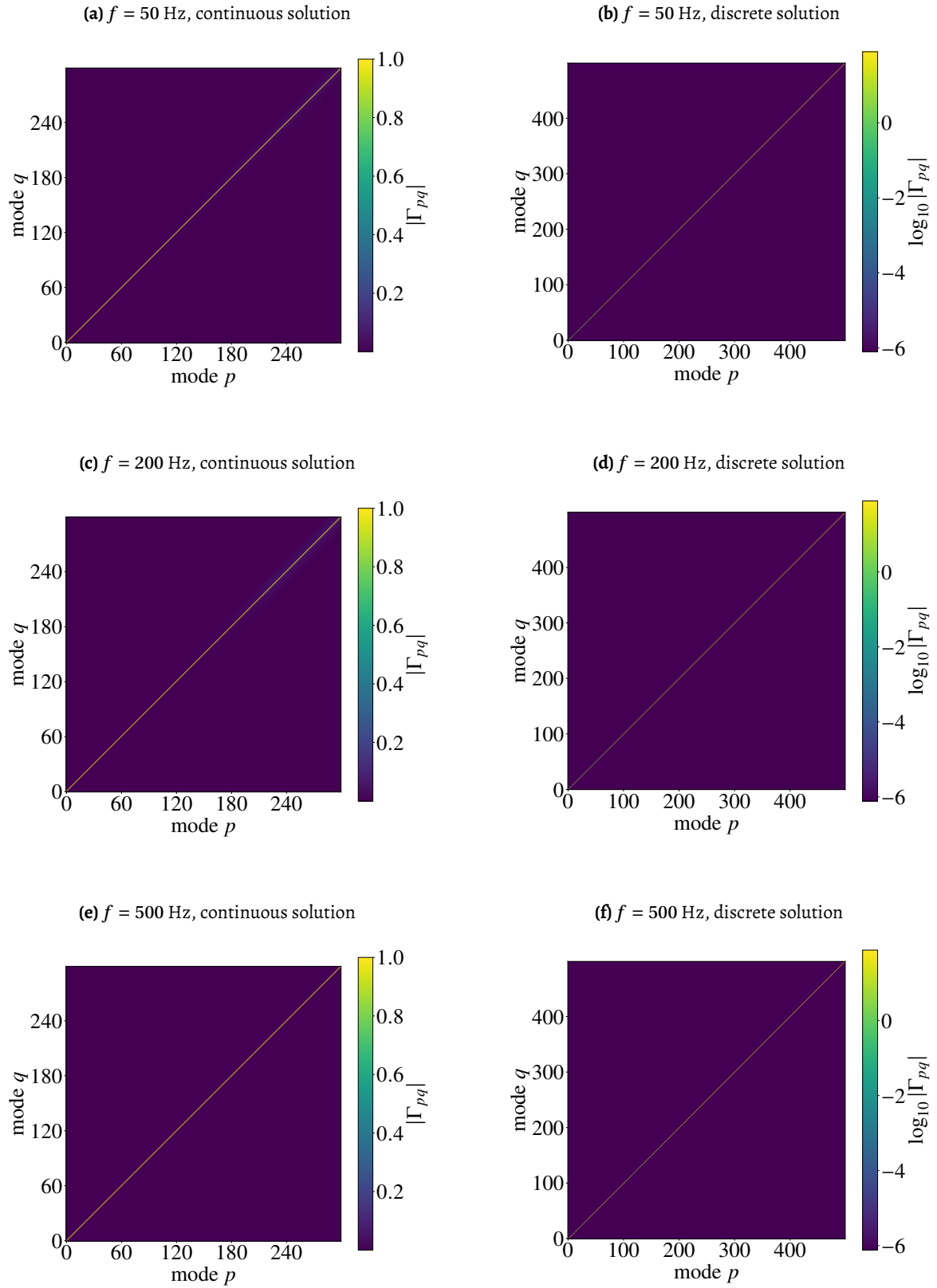
Figure 3.8. Comparison of eigenvector orthogonality between the continuous and discrete solutions for $\alpha_s = 1\,\mathrm{dB}/\lambda$.

4

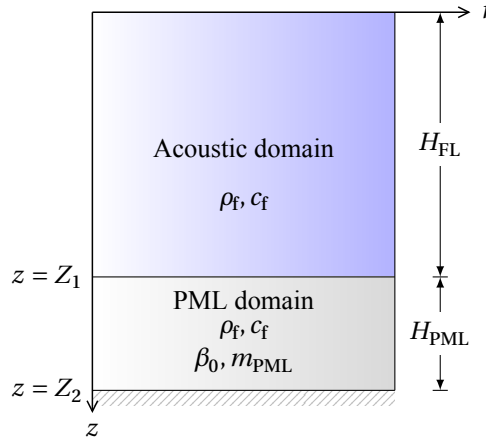# Modal Solution of an Acoustic Domain with PML via Semi-analytical Method

Figure 4.1. Schematic of a single acoustic layer with PML.

Table 4.1. Basic parameters used for numerical examples in Chapter 4

Acoustic layer thickness	H_{FL}	20	m
PML layer thickness	H_{PML}	20	m
Medium Wave Speed	c_{f}	1500	m/s
Fluid Density	ρ_{f}	1000	kg/m^3
Attenuation coefficient	β_0	5	-

This chapter presents the study of the semi-analytical modal solution of an acoustic waveguide with a PML. As shown in Figure 4.1, the single acoustic layer has a thickness of H_{FL} and is extended with a PML with a thickness of H_{PML}. The fluid density ρ_{f} and medium wave speed c_{f} remain constant across both layers. Furthermore, the PML layer requires two specific parameters: the attenuation coefficient β_0 and the polynomial order of the attenuation function m_{PML}. These parameters remain constant across all numerical examples in this chapter, as detailed in Table 4.1. The methodology of this chapter are:

{4.1} Formulate the dispersion relation for the semi-analytical solution.

{4.2} Identify the roots for two different frequencies for the acoustic layer with one PML, using three different polynomial complex stretching functions.

{4.3} Check the orthogonality of eigenmodes for different cases and investigate the effects of m_{PML} on the cross-orthogonality of modes.

{4.4} Check the dispersion characteristics of Bérenger modes.

4.1 Formulation of the eigenvalue problem

Complex-stretched coordinate

Follow the notation in [4, 13], the complex-stretched coordinate $\bar{z}$ is given as:

$$\bar{z} = \int_0^z \varepsilon(z', \omega)\,\mathrm{d}z' = z - \frac{\mathrm{i}}{\omega}\int_0^z \beta(z')\,\mathrm{d}z'. \tag{4.1}$$

where $\varepsilon(z', \omega)$ denotes the complex-valued stretching function [13] and $\beta(z)$ is defined as follows

$$\beta(z) = \begin{cases} 0 & 0 \le z \le Z_1, \\ \beta_0 \omega \big(m_{\mathrm{PML}} + 1\big)\Big(\dfrac{z - H_{\mathrm{FL}}}{H_{\mathrm{PML}}}\Big)^{m_{\mathrm{PML}}} & Z_1 \le z \le Z_2. \end{cases} \tag{4.2}$$

with the amplitude $\beta_0\,\omega\,(m_{\mathrm{PML}} + 1)$ chosen to normalize the magnitude of the complex-stretched coordinate $\bar{z}$ for different values of m_{PML} and ω.

The imaginary part of $\bar{z}$, which governs the exponential decay of waves in the PML, is

$$\mathrm{Im}(\bar{z}) = \begin{cases} 0 & 0 \le z \le Z_1, \\ \beta_0 H_{\mathrm{PML}}\Big(\dfrac{z - H_{\mathrm{FL}}}{H_{\mathrm{PML}}}\Big)^{m_{\mathrm{PML}}+1} & Z_1 \le z \le Z_2. \end{cases} \tag{4.3}$$

An equivalent compact form, also used in [19], is

$$\bar{z} = z - \mathrm{i}\mathrm{H}(z - H_{\mathrm{FL}})\beta_0 H_{\mathrm{PML}}\Big(\frac{z - H_{\mathrm{FL}}}{H_{\mathrm{PML}}}\Big)^{m_{\mathrm{PML}}+1} \tag{4.4}$$

where $\mathrm{H}(\cdot)$ indicates the Heaviside function.

As illustrated in Figure 4.2, while the complex coordinates have consistent boundary values $\bar{z}(Z_1) = Z_1$ and $\bar{z}(Z_2) = Z_2 - \beta_0 H_{\mathrm{PML}}\mathrm{i}$ for all values of m_{PML}, their smoothness at Z_1 is governed by the parameter m_{PML}: When $m_{\mathrm{PML}} = 0$, the profile exhibits a violation of C^1 continuity at $z = Z_1$. Conversely, higher polynomial orders ($m_{\mathrm{PML}} > 0$) ensure C^1 continuity across the interface.
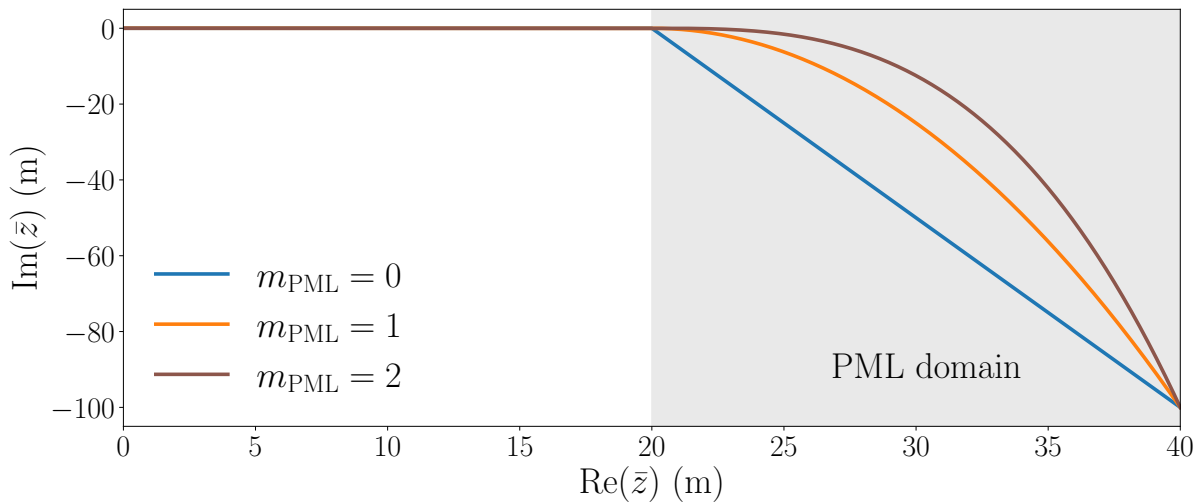

Figure 4.2. Comparison of $\bar{z}$ for different $m_{\mathrm{PML}} = 0$ (blue-continuous line), $m_{\mathrm{PML}} = 1$ (orange-continuous line), $m_{\mathrm{PML}} = 2$ (red-continuous line).

Equation of motions

In an *axisymmetric cylindrical coordinate system* with complex stretching in $\bar{z}$ only, the Helmholtz equation is given as:

$$\overline{\nabla}^2 \widetilde{\phi}_{\mathrm{f}}(r, \bar{z}) + \frac{\omega^2}{c_{\mathrm{f}}^2} \widetilde{\phi}_{\mathrm{f}}(r, \bar{z}) = 0, \tag{4.5}$$

where $\widetilde{\phi}_{\mathrm{f}}(r, z)$ is the velocity potential in the frequency domain of the acoustic layer. The complex-stretched Laplacian $\overline{\nabla}^2$ shows differences in two different layers:

$$\overline{\nabla}^2 = \begin{cases} \partial_r(r\partial_r)/r + \partial_z^2, & 0 \le z \le Z_1, \\ \partial_r(r\partial_r)/r + \partial_z\left[\partial_z/\varepsilon(z)\right]/\varepsilon(z), & Z_1 \le z \le Z_2. \end{cases} \tag{4.6}$$

where $\varepsilon(z) = 1 - \dfrac{\mathrm{i}}{\omega}\beta(z)$.

General solutions

Using *Separation of variables*, the general solutions of Equation (4.5) are given as:

$$\widetilde{\phi}_{\mathrm{f},1}(r, z) = H_0^{(2)}(k_r r)\left[A_1 \exp\left(\mathrm{i}\gamma_{\mathrm{f}}(z - Z_1)\right) + A_2 \exp\left(-\mathrm{i}\gamma_{\mathrm{f}} z\right)\right] \qquad 0 < z < Z_1 \tag{4.7}$$

$$\widetilde{\phi}_{\mathrm{f},2}(r, \bar{z}) = H_0^{(2)}(k_r r)\left[A_3 \exp\left(\mathrm{i}\gamma_{\mathrm{f}}(\bar{z} - \bar{Z}_2)\right) + A_4 \exp\left(-\mathrm{i}\gamma_{\mathrm{f}}(\bar{z} - \bar{Z}_1)\right)\right] \qquad Z_1 < z < Z_2 \tag{4.8}$$

where $\gamma_{\mathrm{f}} = \sqrt{\omega^2/c_{\mathrm{f}}^2 - k_r^2}$ represents the wavenumber of the scalar potential $\tilde{\phi}_{\mathrm{f}}$ in z direction and A_1, A_2 are unknown constants to be computed.

For the i-th mode ($i = 1, 2$), the vector velocity field $\widetilde{\mathbf{v}}_i$ and scalar pressure field $\tilde{p}_{\mathrm{f},i}$ are given by

$$\widetilde{\mathbf{v}}_i = \overline{\nabla}\widetilde{\phi}_{\mathrm{f},i}(r, z, \omega), \tag{4.9}$$

$$\tilde{p}_{\mathrm{f},i} = -\mathrm{i}\omega\rho_{\mathrm{f}}\widetilde{\phi}_{\mathrm{f},i}(r, z, \omega), \tag{4.10}$$

where $\widetilde{\mathbf{v}}_i = \tilde{v}_{r,i}\mathbf{e}_r + \tilde{v}_{z,i}\mathbf{e}_z$ has components in the r- and z-directions.

Boundary and interface conditions

Except for the radiation condition at $r \to \infty$ satisfied automatically via the general solutions, the following boundary and interface conditions:

$$\tilde{p}_{\mathrm{f},1}(r, 0, \omega) = 0 \qquad\qquad \tilde{p}_{\mathrm{f},2}(r, \overline{Z}_2, \omega) = 0 \tag{4.11}$$

$$\tilde{p}_{\mathrm{f},1}(r, Z_1, \omega) = \tilde{p}_{\mathrm{f},2}(r, \overline{Z}_1, \omega) \qquad\qquad \tilde{v}_{z,1}(r, Z_1, \omega) = \tilde{v}_{z,2}(r, \overline{Z}_1, \omega) \tag{4.12}$$

Substituting the assumed general solutions into the equations above leads to the eigenvalue problem $\mathbf{MA} = \mathbf{0}$. The detailed form of $\mathbf{M}$ is given in Equation (A.2) in Appendix A for interested readers.

Dispersion relation

Setting $\det \mathbf{M} = 0$ gives the following dispersion relation:

$$2\gamma_{\mathrm{f}}\left[1 + \exp\left(2\gamma_{\mathrm{f}}\left((\mathrm{i} + \beta_0)H_{\mathrm{PML}} + \mathrm{i}Z_1\right)\right)\right] = 0 \tag{4.13}$$

Equation (4.13) suggests that the dispersion relation of one acoustic layer with one PML layer depends on Z_1, k_{f}, β_0, and H_{PML}. In other words, the eigenvalues should be consistent for different values of m_{PML} in this scenario.

Table 4.2. PML polynomial order and frequencies used in Chapter 4

| Groups	PML Order		Frequency	
Group 1.1	m_{PML}	$0 - f$	50	Hz
Group 1.2	m_{PML}	$1 - f$	50	Hz
Group 1.3	m_{PML}	$2 - f$	50	Hz
Group 2.1	m_{PML}	$0 - f$	200	Hz
Group 2.2	m_{PML}	$1 - f$	200	Hz
Group 2.3	m_{PML}	$2 - f$	200	Hz

4.2 Numerical results and discussions

Six numerical cases have been considered in this chapter, as indicated in Table 4.2. These cases combine two frequencies with three PML polynomial orders:

1. $f = 50\,\mathrm{Hz}$: $m_{\mathrm{PML}} = 0, 1, 2$

2. $f = 200\,\mathrm{Hz}$: $m_{\mathrm{PML}} = 0, 1, 2$

4.2.1 Eigenvalues

Using the root-finding algorithm described previously, the roots of Equation (4.13) have been determined for all cases listed in Table 4.2. Figure 4.3 shows the visualization of $|\det(\mathbf{M})|$ in the complex k_r plane for $f = 50\,\mathrm{Hz}$, here $\log_{10}|\det(\mathbf{M})|$ is shown here for a better visualization. This surface plot clearly demonstrates the positions of the poles of Equation (4.13), which appear as minima of the surface in the complex k_r plane.
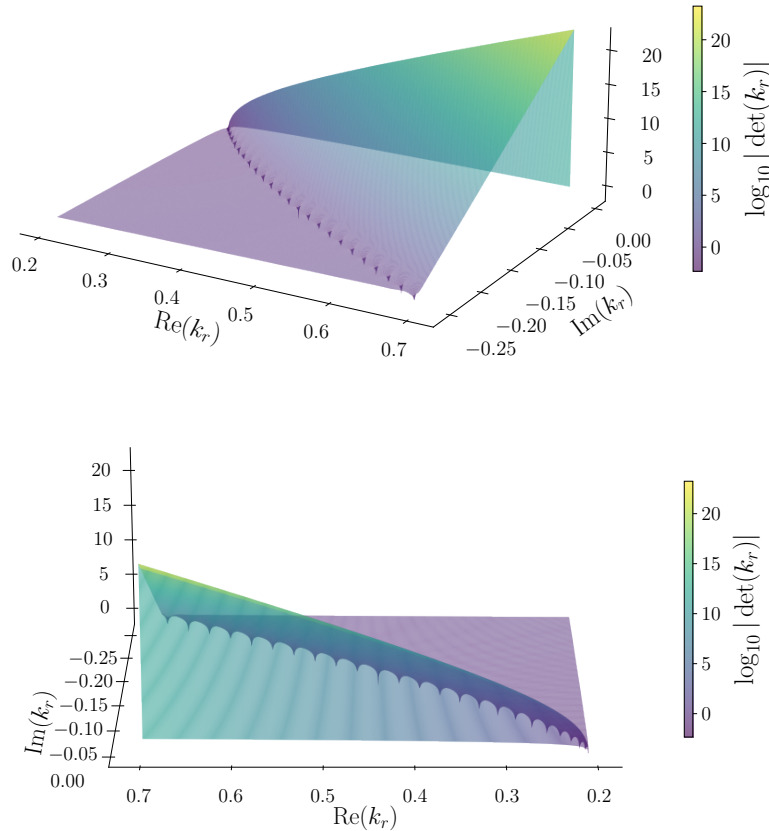
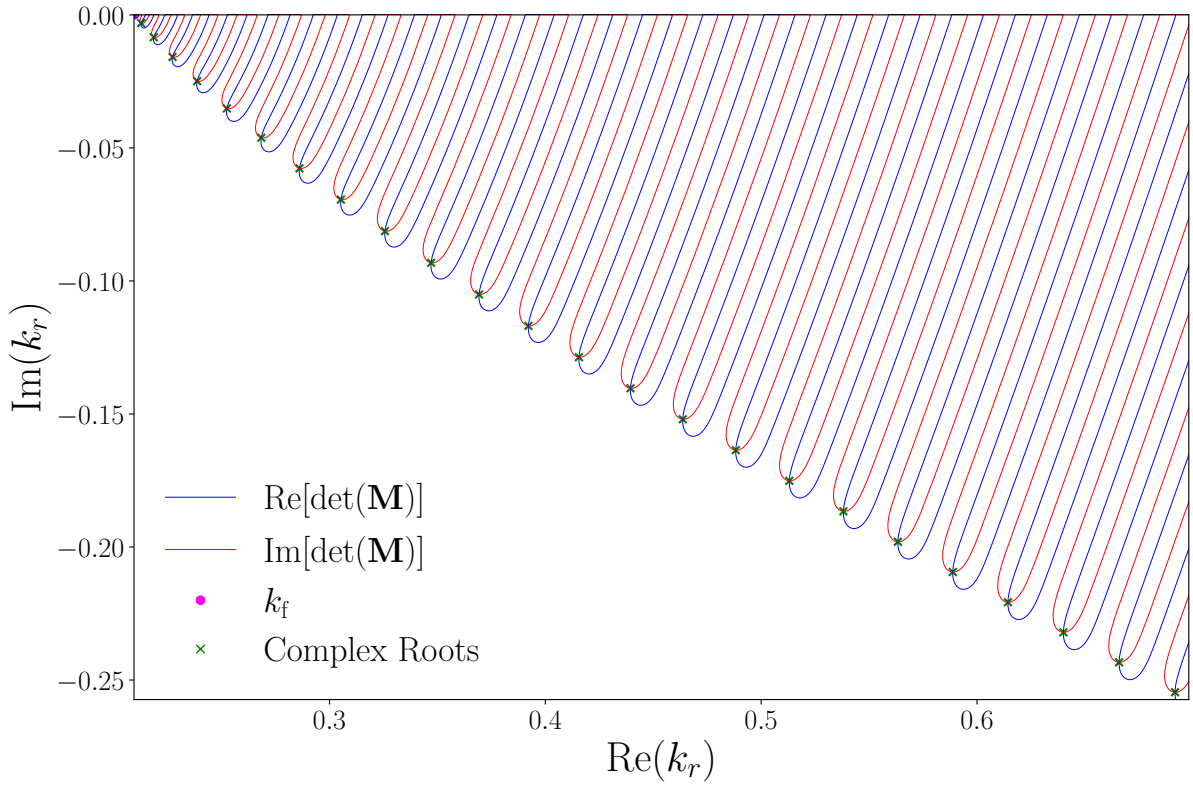**Figure 4.3.** 3D visualizations of $\det(k_r)$ for $f = 50$Hz

Figure 4.4. Zero contour plots of real and imaginary parts of Equation (4.13) for $f = 50$Hz

Figure 4.4 and 4.3 show that all complex roots were distributed along *one hyperbolic branch*, as suggested by [9] for the finite PML layer.

4.2.2 Orthogonality between Eigenvectors and Conjugate Eigenvectors

The cross-orthogonality of modes and their conjugate eigenvectors has already been proved in [26] for the Pekeris Waveguide with one PML, the method has been modified in this thesis for the single acoustic layer with one PML layer:

$$\Gamma_{pq} = \Gamma_p \delta_{pq} = \int_0^{Z_2} \overline{\varphi_{\mathrm{f},p}} \cdot \phi_{\mathrm{f},q} \, \mathrm{d}z \tag{4.14}$$

where $\overline{\varphi_{\mathrm{f},p}}$ is the $p-$th conjugate eigenvector and k_{r_p} are its related eigenvalue; $\varphi_{\mathrm{f},q}$ is the $q-$th eigenvector and k_{r_q} are its related eigenvalue. Moreover, $\overline{\varphi_{\mathrm{f},p}}$ satisfies the following adjoint equation of (4.5):

$$\frac{\mathrm{d}^2 \overline{\varphi_{\mathrm{f},p,1}}}{\mathrm{d}z^2} + \left(k_{\mathrm{f}}^2 - k_r^2\right)\overline{\varphi_{\mathrm{f},p,1}} = 0 \qquad\qquad 0 < z < Z_1 \tag{4.15}$$

$$\frac{\mathrm{d}}{\mathrm{d}z}\left(\frac{1}{\varepsilon(z)}\frac{\mathrm{d}}{\mathrm{d}z}\left(\frac{\overline{\varphi_{\mathrm{f},p,2}}}{\varepsilon(z)}\right)\right) + \left(k_{\mathrm{f}}^2 - k_r^2\right)\frac{\overline{\varphi_{\mathrm{f},p,2}}}{\varepsilon(z)} = 0 \qquad\qquad Z_1 < z < Z_2 \tag{4.16}$$

Therefore, the general solutions of Equation (4.16) is given as:

$$\overline{\varphi_{\mathrm{f},p,1}(z)} = A_1 \exp\left[\mathrm{i}\gamma_{\mathrm{f}}(z - Z_1)\right] + A_2 \exp(-\mathrm{i}\gamma_{\mathrm{f}}z) \qquad\qquad 0 \leq z \leq Z_1, \tag{4.17}$$

$$\overline{\varphi_{\mathrm{f},p,2}(z)} = \left[A_3 \exp\left[\mathrm{i}\gamma_{\mathrm{f}}(\bar{z} - \bar{Z}_2)\right] + A_4 \exp\left[-\mathrm{i}\gamma_{\mathrm{f}}(\bar{z} - \bar{Z}_1)\right]\right]\varepsilon(z) \qquad\qquad Z_1 \leq z \leq Z_2 \tag{4.18}$$

$\overline{\varphi_{\mathrm{f},p,2}(z)}/\varepsilon(z)$ satisfy the same boundary conditions of $\phi_{\mathrm{f},q}$. The detailed derivation of these equations will not be expanded here for the sake of brevity, but it is provided in Appendix A for interested readers.

4.2.3 Eigenvectors

The eigenvectors are determined by considering a slight inhomogeneous boundary velocity at the bottom of the PML domain, then normalized so that $|\Gamma_{pp}| = 1$. Figure 4.5 compares the normalized modes for different PML polynomial orders m_{PML}; each subfigure is associated with one frequency in Table 4.2.
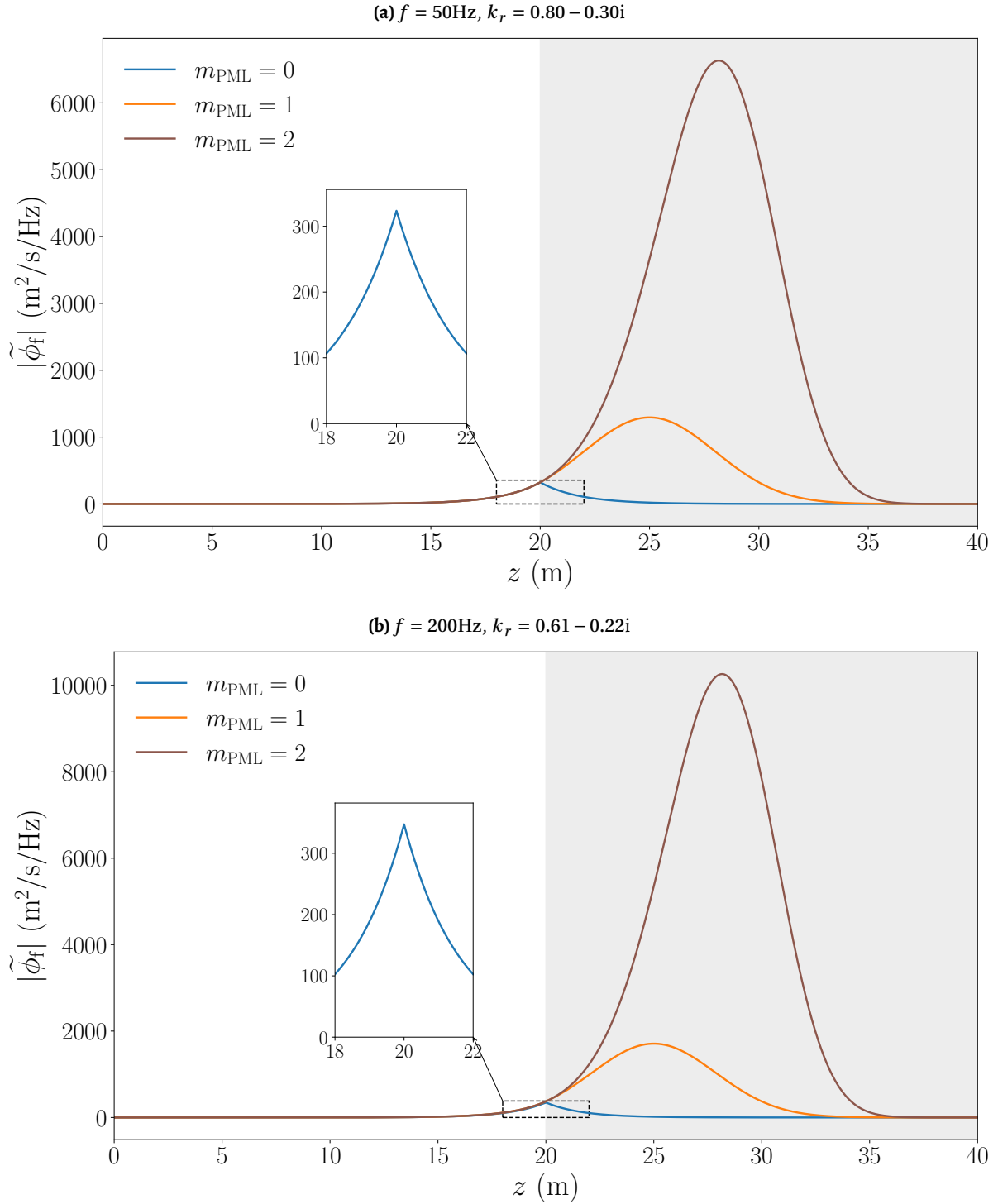

(a) $f = 50\text{Hz}$, $k_r = 0.80 - 0.30\text{i}$

(b) $f = 200\text{Hz}$, $k_r = 0.61 - 0.22\text{i}$

Figure 4.5. Comparison of different modes for three different values of m_{PML} for (a) $f = 50$ Hz, (b) $f = 200$ Hz.

The following observations are made:

(1) *These eigenvectors exhibit some anomalous behavior.* Figure 4.5 suggests all modes exhibit an exponential-like profile, remaining nearly flat in the regular region and rising sharply when approaching the PML. The modal amplitude is closely associated with the energy characteristics of the mode. Therefore, the modal energy exhibits the same characteristic behaviour. Theoretically, the energy of these modes should propagate with a nearly horizontal angle because $\mathrm{Re}(k_r) \gg \mathrm{Im}(k_r)$. However, the energy of eigenvectors in Figure 3.4 is suddenly amplified near the interface between the acoustic and PML domains, which is quite anamalous compared to physical modes. These modes are so-called nonphysical pseudo-numerical modes in the existing literature[4, 9, 17].

(2) *The C^1 continuity (continuity of slope) is violated at $z = Z_1$, if $m_{\mathrm{PML}} = 0$ is used.* Briefly, this discontinuity of $\mathrm{Im}(\varepsilon)$ will induce a discontinuity in the derivative operator, which finally results in a discontinuity of the slope of the modal solution at $Z = Z_1$. When $m_{\mathrm{PML}} = 0$ is assumed, a discontinuous complex stretch function $\mathrm{Im}(\varepsilon(z))$ will be generated, as depicted in Figure 4.6. The slope of the mode at the right interface $z = Z_1^+$ is complex stretched as follows in the PML domain:

$$\widetilde{\phi}'_{\mathrm{f},2}\Big|_{Z_1^+} = \frac{1}{\varepsilon(Z_1^+)} \frac{\mathrm{d}\widetilde{\phi}_{\mathrm{f},2}}{\mathrm{d}z}\Big|_{Z_1^+} \tag{4.19}$$

Whereas, this slope is as follows at $z = Z_1^-$ (left interface in the regular domain):

$$\widetilde{\phi}'_{\mathrm{f},1}\Big|_{Z_1^-} = \frac{\mathrm{d}\widetilde{\phi}_{\mathrm{f},2}}{\mathrm{d}z}\Big|_{Z_1^-} \tag{4.20}$$

When $m_{\mathrm{PML}} = 0$, as seen in the blue line in the Figure 4.6:

$$\mathrm{Im}(\varepsilon(Z_1^+)) < 0 \rightarrow \varepsilon(Z_1^+) \neq 1 \tag{4.21}$$

Therefore, a *discontinuous slope of the potential field* $\widetilde{\phi}_{\mathrm{f}}$ is found at $z = Z_1$ from Equations (4.19) and (4.20):

$$\varepsilon(Z_1^+) \neq 1 \leftrightarrow \widetilde{\phi}'_{\mathrm{f},1}\Big|_{Z_1^-} \neq \widetilde{\phi}'_{\mathrm{f},2}\Big|_{Z_1^+} \tag{4.22}$$

The physical meaning of the first-order derivative of the potential field corresponds to the velocity field. In other words, violation of the C^1 continuity condition represents a discontinuity in the velocity field at the regular-PML domain interface. For this reason, a piecewise-linear complex-stretching function is not recommended, as it would introduce artificial velocity discontinuities that are physically unrealistic.
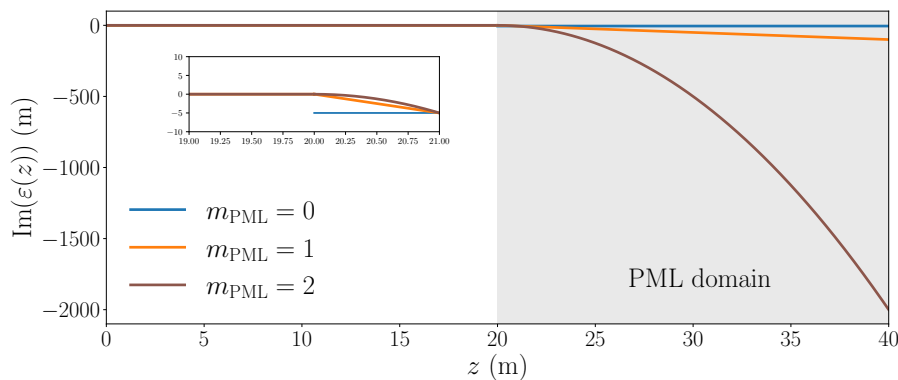

Figure 4.6. Comparison of $\varepsilon(z)$ for different $m_{\mathrm{PML}} = 0$ (blue-continuous line), $m_{\mathrm{PML}} = 1$ (orange-continuous line), $m_{\mathrm{PML}} = 2$ (red-continuous line).

4.2.4 Modal Orthogonality

This section investigates characteristics of modal orthogonality between modes and their conjugate eigenvectors under the context of the perfectly matched layer (PML) of acoustic layers. Briefly, the results and discussions reflect the following three aspects on orthogonality:

1. the influence of polynomial orders m_{PML};

2. the impact of the size of the integration step dz;

3. the influence of different integration schemes.

Orthogonality for different values of m_{PML}

$|\Gamma_{pq}|$ was computed using Equation (4.14). Furthermore, the in-built numerical integration function `np.trapz` was used and dz is 1×10^{-5} m. The six subfigures in Figure 4.7 indicate the $|\Gamma_{pq}|$ for the first thirty modes that correspond to different values of m_{PML} and f. For two different considered frequencies (50 Hz and 200 Hz), the following observations are made:

1. When the value of polynomial order m_{PML} is increased from 0 to 1 or 2, the values of off-diagonal elements are reduced, indicating a better cross-orthogonality.

2. However, when m_{PML} is equal to 2, some diagonal elements $|\Gamma_{pp}|$, are found to be larger than 1.

The cause of the first observation is given below: Following a derivation on the cross-orthogonality between eigenvectors and their conjugate eigenvectors of an acoustic layer with one PML with a fixed bottom boundary in Appendix A, the boundary terms that are produced during the integration by parts read:

$$\overline{\varphi_{\text{f},1}(Z_1)}\Big[\phi_{\text{f},1}'(Z_1) - \phi_{\text{f},2}'(Z_1)\Big] + \phi_{\text{f},2}(Z_1)\left[\left(\overline{\varphi_{\text{f},1}}/\varepsilon\right)'\bigg|_{z=Z_1} - \left(\overline{\varphi_{\text{f},2}}/\varepsilon\right)'\bigg|_{z=Z_1}\right] \tag{4.23}$$

where ϕ_i represents the mode and $\overline{\varphi_i}$ represents its conjugate eigenvectors. The elimination of boundary terms is seen as a necessary condition for deriving the final conjugate eigenvectors, which are subject to the following condition:

$$C^1 \text{ continuity of } \phi_{\text{f}}(z) \text{ and } \left(\overline{\varphi_{\text{f}}}(z)/\varepsilon(z)\right) \text{ at } z = Z_1$$

which is not valid at $m_{\text{PML}} = 0$ form the mathematical derivation and numerical results in Figure 4.5. Therefore, these remaining boundary terms may lead to the failure of deriving conjugate eigenvectors, which finally violates the orthogonality relations between eigenvectors and their conjugate eigenvectors in Equation (4.14).

Furthermore, the continuity of the complex stretching function ε and its derivative ε' are required to eliminate all boundary terms, which have been derived in Appendix A. Therefore, from mathematical derivation, it is suggested to use $m_{\text{PML}} = 2$ to maintain the C^0 and C^1 continuity of the complex stretching function.

However, the reason behind the second observation requires further investigation in future work. The values of $|\Gamma_{pq}|$ for a higher polynomial order, namely $m_{\text{PML}} = 3$, were also computed, and similar conclusions were obtained as for the case of $m_{\text{PML}} = 2$. As increasing m_{PML} results in a higher-order polynomial $\varepsilon(z)$ in the evaluation of $|\Gamma_{pq}|$ via Equation (4.14), it is possible that `np.trapz` may not provide sufficiently accurate numerical integration. This limitation arises because the trapezoidal rule is only first-order accurate, and its performance deteriorates when the integrand exhibits strong variations or oscillations, as is the case for higher-order $\varepsilon(z)$. Therefore, more advanced quadrature schemes may be required for $m_{\text{PML}} > 1$, which warrants systematic investigation in future work.
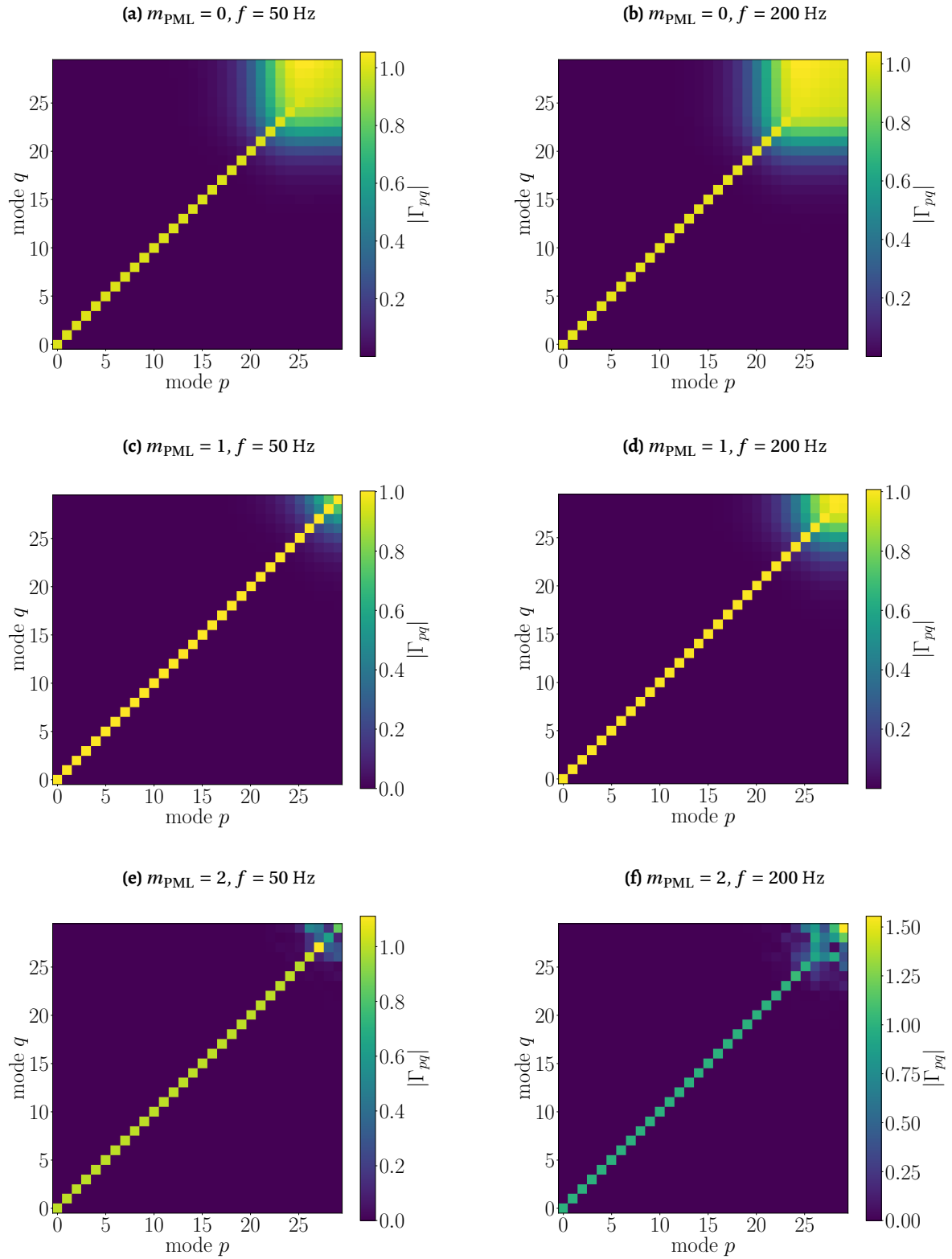
(a) $m_{\mathrm{PML}} = 0, f = 50$ Hz

(b) $m_{\mathrm{PML}} = 0, f = 200$ Hz

(c) $m_{\mathrm{PML}} = 1, f = 50$ Hz

(d) $m_{\mathrm{PML}} = 1, f = 200$ Hz

(e) $m_{\mathrm{PML}} = 2, f = 50$ Hz

(f) $m_{\mathrm{PML}} = 2, f = 200$ Hz

Figure 4.7. Orthogonality heatmaps of modes and its conjugate eigenvectors for different PML polynomial orders m_{PML} of complex-stretch functions at $f = 50$ Hz: (a) $m_{\mathrm{PML}} = 0$, (b) $m_{\mathrm{PML}} = 1$, (c) $m_{\mathrm{PML}} = 2$..

Orthogonality for different values of dz

In this section, the influence of the size of integration steps is discussed. $m_{PML} = 1$ will be assumed for this case, and three values of dz have been considered: (i) $dz = 1 \times 10^{-3}$ m, (ii) $dz = 1 \times 10^{-4}$ m and (iii) $dz = 1 \times 10^{-5}$ m.

The value of $|\Gamma_{pq}|$ are shown in Figure 4.8 for $f = 200$ Hz. It can be observed from the following six figures that finer integration steps will reduce the magnitude of the off-diagonal element with large values of p and q, reflecting a better cross-orthogonality between modes and their conjugate eigenvectors for these *high-order modes*[1]. This behavior can be explained by the exponential nature of higher-order modes. Modes with larger imaginary parts exhibit more pronounced exponential decay, causing their modal amplitudes to change rapidly near the peak values of the eigenvectors (see Figure 4.5). Consequently, more integration steps are necessary to accurately capture these steep variations and maintain an accurate calculation of the cross-orthogonality.
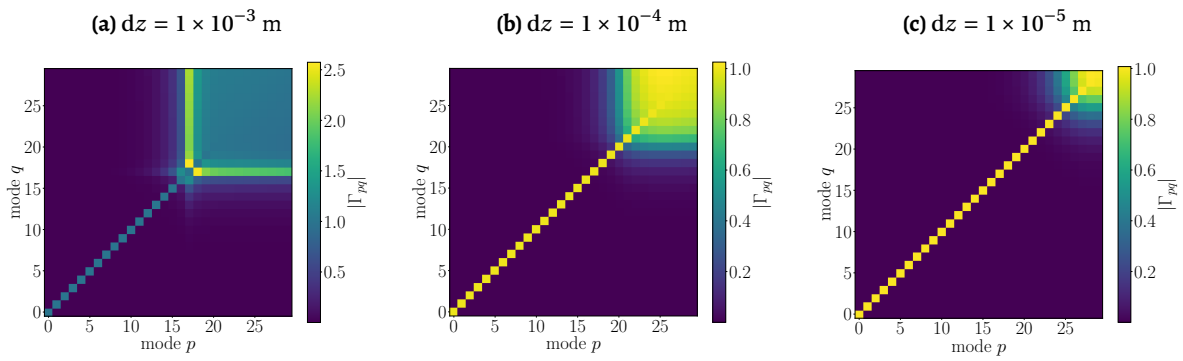

(a) $dz = 1 \times 10^{-3}$ m   **(b)** $dz = 1 \times 10^{-4}$ m   **(c)** $dz = 1 \times 10^{-5}$ m

Figure 4.8. Orthogonality heatmaps of the first thirty modes and their conjugate eigenvectors for different size of integration step dz of complex-stretch functions at $f = 200$ Hz: (a) $dz = 1 \times 10^{-3}$ m, (b) $dz = 1 \times 10^{-4}$ m, (c) $dz = 1 \times 10^{-5}$ m.
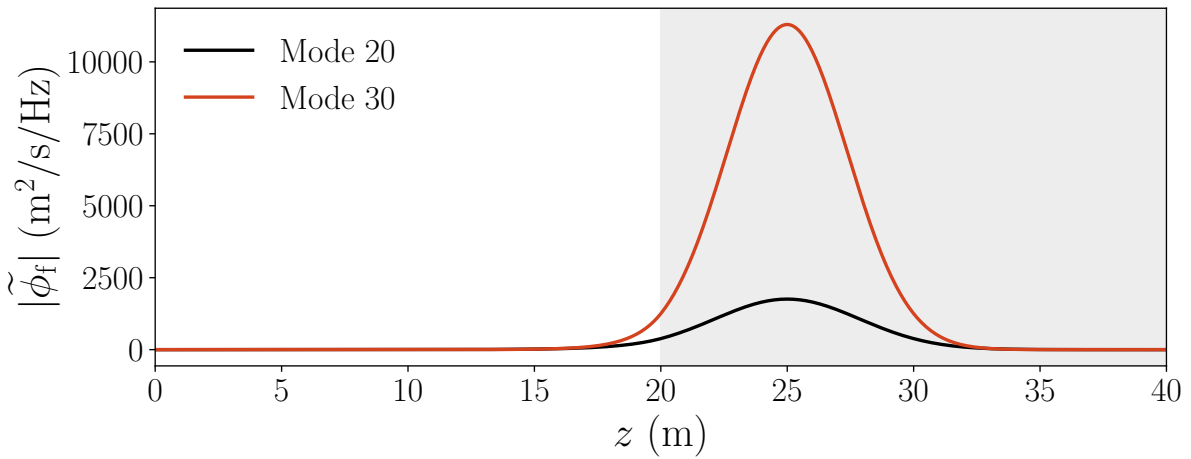

Figure 4.9. Comparison of mode 20 and 30 at $f = 200$ Hz: higher-order modes (red-continuous line), lower-order modes (black-continuous line)

---

[1]Here higher order modes represent the modes with larger $\text{Re}(k_r)$ and $\text{Im}(k_r)$ in Figure 4.4

4.2.5 Modal Dispersion Characteristics

Figure 4.10 presents the first thirteen dispersion curves for the single fluid layer with one PML, as defined in Figure 4.1, obtained from the complex-valued eigenvalues computed by the numerical root-finding algorithm for f ranging from 0 to 30 Hz. The left column shows the imaginary part, and the left column shows the real part. The complex-valued roots are found numerically via the root-finder; some points are missing; however, the main dispersion branches are clearly captured and sufficient for the present discussion. In addition, Figure 4.11 shows the group and phase velocities of the top 10 modes, ranked by $\mathrm{Re}(k_r)$ at the terminal frequency, computed using Equation (2.35). As can be observed from Figures 4.10 and 4.11:

1. The dispersion curves exhibit large slopes, indicating that all modes experience high group velocities across the ω range.

2. As shown in Figure (4.11), with increasing frequency, the group velocity decreases, and phase velocity increases. This finding is opposite to the profile of the group and phase velocity of the physical modes, which is indicated by Figure 2.8. The phase velocity of all modes is smaller than the group velocity, which follows the definition of *anomalous dispersion* given by Miklowitz in [14].
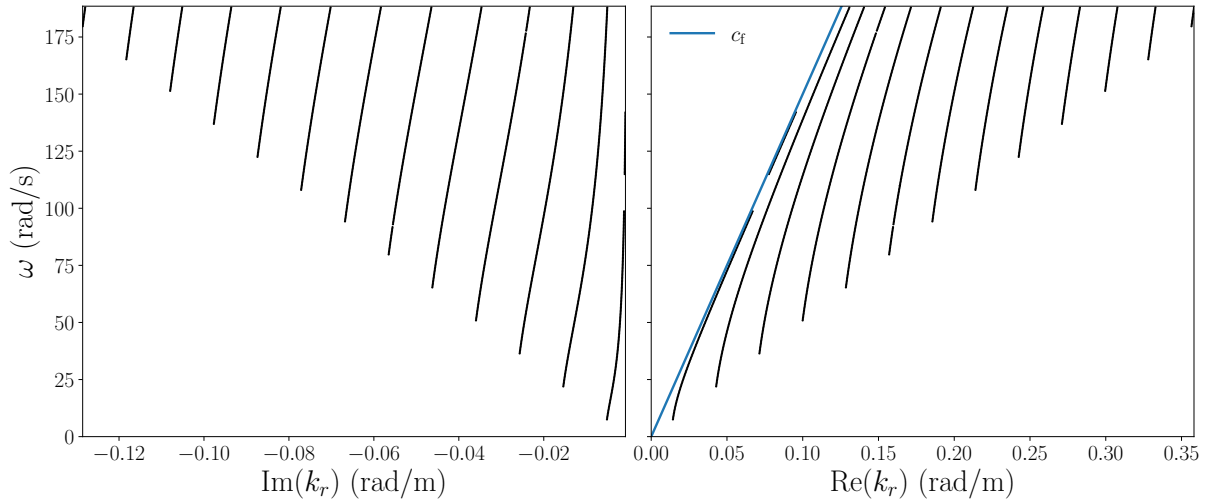

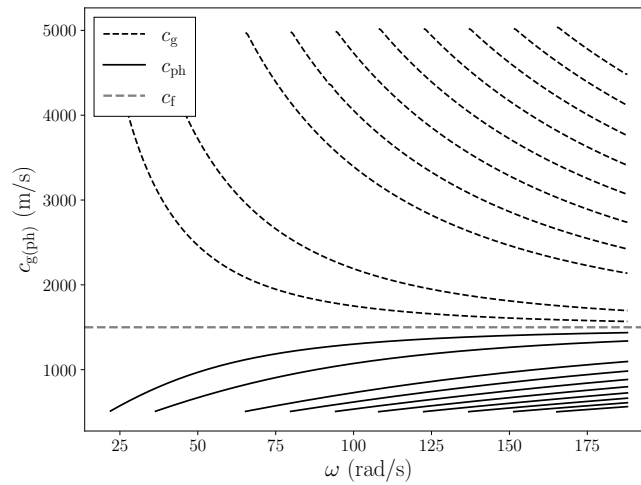**Figure 4.10.** Dispersion curves for one acoustic layer with one PML

Figure 4.11. Group and phase velocity spectra of the top 10 modes ranked by $\mathrm{Re}(k_r)$ at the last frequency.

4.3 Summary

This Chapter provides a study of the normal-mode solution of a single acoustic domain with a perfectly matched layer (PML) in Figure 4.1, via the semi-analytical method. In particular, the key conclusions are summarized as follows:

1. The roots of the dispersion relation Equation (4.13) were detected successfully by the root-finder for two considered frequencies: 50 Hz and 200 Hz. First, they are located around a hyperbolic line. Second, for a single acoustic layer with PML, the form dispersion relation is not dependent on polynomial orders; therefore, the eigenvalues will not be subject to different choices of the complex-stretch function in the semi-analytical solution.

2. The spatial profile of modes that are considered here *share some nonphysical characteristics*. First, they grow exponentially in the physical domain before being attenuated in the PML. Physically, their energy starts to amplify inside the PML domain.

3. The eigenvectors (modes) will differ between values of m_{PML}. The mode will have a discontinuous slope at the interface of the regular and PML domains, if $m_{\mathrm{PML}} = 0$ is chosen. For this reason, a linear attenuation function in the PML domain is not suggested, because the violation of C^1 continuity is equivalent to discontinuous velocity, which is not acceptable from a physical perspective. For this reason, $m_{\mathrm{PML}} > 0$ will be assumed in the remaining cases.

4. Using $m_{\mathrm{PML}} = 0$ violates orthogonality: it violates the slope continuity of the eigenvector at the interface between the PML and physical domain. As a result, the boundary terms in Equation (4.23) will not be eliminated when deriving the conjugate modes via the method in [26]. Finally, the cross orthogonality of the mode and its conjugate eigenvector will be violated. Again, $m_{\mathrm{PML}} > 0$ is suggested for the application of complex stretch in the semi-analytical solution, because it maintains the C^1 continuity of the eigenvector at $z = Z_1$.

5. For higher-order PML polynomials ($m_{\mathrm{PML}} > 1$), the use of `np.trapz` may lead to inaccuracies in evaluating orthogonality integrals, since the trapezoidal rule is only first-order accurate and becomes unreliable when the integrand exhibits strong variations. Mathematically, the orthogonality is still valid, but the numerical integration may fail to capture it accurately. This limitation suggests that more advanced quadrature schemes should be considered in future work.

6. Bérenger modes exhibit *anomalous dispersion*. They display unrealistically high group velocities across all frequencies, and, moreover, their group velocities exceed the corresponding phase velocities, which is physically invalid.

5

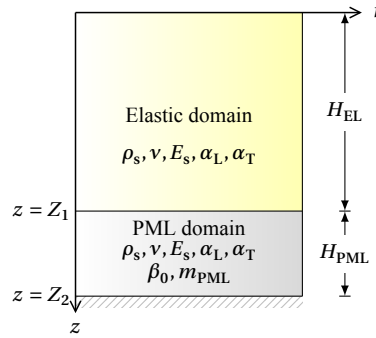# Modal Solution of a Single Elastic Domain with a PML

Figure 5.1. Schematic of a single elastic domain with one PML

Table 5.1. Basic parameters used for numerical examples in Chapter 5

Elastic layer thickness	H_{EL}	5	m
PML layer thickness	H_{PML}	5	m
Solid density	ρ_s	1700	kg/m^3
Young's modulus	E_s	0.7	MPa
Poisson's ratio	ν	0.4	-
Attenuation coefficient	β_0	5	-
PML order	m_{PML}	2	-

This chapter compares the Thin-Layer method and a semi-analytical approach regarding their modal solutions for a single elastic waveguide with a PML. Figure 5.1 shows the statement of the problem, where a single elastic layer has a thickness of H_{EL} and is above a PML with a thickness of H_{PML}. Besides, the geometry dimensions, material properties, and PML parameters used in this chapter are displayed in Table 5.1. Furthermore, they remain fixed across all numerical examples in this chapter. The methodology of this chapter is briefly given as:

{5.1} Formulate the eigenvalue problem via the semi-analytical method and TLM.

{5.2} Identify the roots for two different loading frequencies of the system, using a quadratic complex-stretched functions in the PML domain.

{5.3} Check the orthogonality condition of eigenvectors of semi-analytical solutions.

{5.4} Compare the eigenvalues and modes computed from TLM and semi-analytical method. The number of layers in the PML domain is treated as a variable for the Thin-layer method. The comparison is performed for different numbers of layers.

5.1 Formulation of the eigenvalue problem

5.1.1 Continuous solution

Following the same notations in Chapter 3, we will start from the Helmholtz equations in elastodynamics, in the elastic domain:

$$\nabla^2 \widetilde{\phi}_{s,1}(r,z;\omega) + k_L^2\, \widetilde{\phi}_{s,1}(r,z;\omega) = 0 \qquad\qquad 0 < z < Z_1, \tag{5.1}$$

$$\nabla^2 \widetilde{\psi}_{s,1}(r,z;\omega) - \frac{\widetilde{\psi}_{s,1}(r,z;\omega)}{r^2} + k_T^2\, \widetilde{\psi}_{s,1}(r,z;\omega) = 0, \qquad\qquad 0 < z < Z_1, \tag{5.2}$$

where the Laplacian operator ∇ is:

$$\nabla^2 = 1/r\,\partial_r(r\partial_r)\mathbf{e}_r + \partial_z^2 \mathbf{e}_z. \tag{5.3}$$

The coordinate z is assumed to be stretched into a complex-valued $\bar{z}$ in the PML domain using Equation (4.4)

$$z \to \bar{z} = z - \mathrm{i}\beta_0 H_{\mathrm{PML}}\left(\frac{z - H_{\mathrm{EL}}}{H_{\mathrm{PML}}}\right)^3 \qquad Z_1 < z < Z_2 \tag{5.4}$$

Correspondingly, the Helmholtz equations in the PML domain are:

$$\overline{\nabla}^2 \widetilde{\phi}_{s,2}(r,\bar{z};\omega) + k_L^2\, \widetilde{\phi}_{s,2}(r,\bar{z};\omega) = 0 \qquad\qquad \bar{Z}_1 < \bar{z} < \bar{Z}_2, \tag{5.5}$$

$$\overline{\nabla}^2 \widetilde{\psi}_{s,2}(r,\bar{z};\omega) - \frac{\widetilde{\psi}_{s,2}(r,\bar{z};\omega)}{r^2} + k_T^2\, \widetilde{\psi}_{s,2}(r,\bar{z};\omega) = 0, \qquad\qquad \bar{Z}_1 < \bar{z} < \bar{Z}_2. \tag{5.6}$$

$\overline{\nabla}^2$ is modified Laplacian operator with complex stretched $\bar{z}$:

$$\overline{\nabla}^2 = 1/r\,\partial_r(r\partial_r)\mathbf{e}_r + 1/\varepsilon(z)\cdot\partial_z(\partial_z/\varepsilon(z))\mathbf{e}_z. \tag{5.7}$$

The expressions of all potential fields in the elastic domain read:

$$\widetilde{\phi}_{s,1} = \left[A_1 \exp\left(\mathrm{i}\gamma_L z\right) + A_2 \exp\left(-\mathrm{i}\gamma_L z\right)\right] H_0^{(2)}(k_r r) \qquad\qquad 0 < z < Z_1 \tag{5.8}$$

$$\widetilde{\psi}_{s,1} = \left[A_3 \exp\left(\mathrm{i}\gamma_T z\right) + A_4 \exp\left(-\mathrm{i}\gamma_T z\right)\right] H_1^{(2)}(k_r r), \qquad\qquad 0 < z < Z_1 \tag{5.9}$$

On the other hand, the potential fields in the PML domain are:

$$\widetilde{\phi}_{s,2} = \left[A_5 \exp\left(\mathrm{i}\gamma_L \bar{z}\right) + A_6 \exp\left(-\mathrm{i}\gamma_L \bar{z}\right)\right] H_0^{(2)}(k_r r), \qquad\qquad \overline{Z}_1 < \bar{z} < \overline{Z}_2 \tag{5.10}$$

$$\widetilde{\psi}_{s,2} = \left[A_7 \exp\left(\mathrm{i}\gamma_T \bar{z}\right) + A_8 \exp\left(-\mathrm{i}\gamma_T \bar{z}\right)\right] H_1^{(2)}(k_r r). \qquad\qquad \overline{Z}_1 < \bar{z} < \overline{Z}_2 \tag{5.11}$$

The general solutions here were modified, aimed at

1. avoiding the overflows of the exponential terms

2. a stable mapping for calculating the determinant of the matrix of coefficients, as suggested by Jensen in [11]

$$\widetilde{\phi}_{s,1} = \left[A_2 \exp\left(-\mathrm{i}\gamma_L z\right) + A_1 \exp\left(\mathrm{i}\gamma_L(z - Z_1)\right)\right] H_0^{(2)}(k_r r), \qquad\qquad 0 < z < Z_1 \tag{5.12}$$

$$\widetilde{\psi}_{s,1} = \left[A_4 \exp\left(-\mathrm{i}\gamma_T z\right) + A_3 \exp\left(\mathrm{i}\gamma_T(z - Z_1)\right)\right] H_1^{(2)}(k_r r), \qquad\qquad 0 < z < Z_1 \tag{5.13}$$

$$\widetilde{\phi}_{s,2} = \left[A_6 \exp\left(-\mathrm{i}\gamma_L(\bar{z} - \overline{Z}_1)\right) + A_5 \exp\left(\mathrm{i}\gamma_L(\bar{z} - \overline{Z}_2)\right)\right] H_0^{(2)}(k_r r), \qquad\qquad \overline{Z}_1 < \bar{z} < \overline{Z}_2 \tag{5.14}$$

$$\widetilde{\psi}_{s,2} = \left[A_8 \exp\left(-\mathrm{i}\gamma_T(\bar{z} - \overline{Z}_1)\right) + A_7 \exp\left(\mathrm{i}\gamma_T(\bar{z} - \overline{Z}_2)\right)\right] H_1^{(2)}(k_r r), \qquad\qquad \overline{Z}_1 < \bar{z} < \overline{Z}_2 \tag{5.15}$$

The post-processed displacement field vector $\tilde{\mathbf{u}}_{s,1}$ in the elastic layer is written as below:

$$\tilde{\mathbf{u}}_{s,1} = \left(\partial_r \widetilde{\phi}_{s,1} - \partial_z \widetilde{\psi}_{s,1}\right)\mathbf{e}_r + \left(\partial_z \widetilde{\phi}_{s,1} + \partial_r \widetilde{\psi}_{s,1} + \widetilde{\psi}_{s,1}/r\right)\mathbf{e}_z. \tag{5.16}$$

Incorporating the complex stretch, field vector $\tilde{\mathbf{u}}_{s,2}$ in the PML is

$$\tilde{\mathbf{u}}_{s,2} = \left(\partial_r \widetilde{\phi}_{s,2} - \partial_z \widetilde{\psi}_{s,2}/\varepsilon(z)\right)\mathbf{e}_r + \left(\partial_z \widetilde{\phi}_{s,2}/\varepsilon(z) + \partial_r \widetilde{\psi}_{s,2} + \widetilde{\psi}_{s,2}/r\right)\mathbf{e}_z. \tag{5.17}$$

The vertical stress fields $\widetilde{\sigma}_{zz,i}$ $(i=1,2)$ are:

$$\widetilde{\sigma}_{zz,1} = \lambda_s \cdot \left(\partial_r^2 \widetilde{\phi}_{s,1} + \frac{1}{r}\partial_r \widetilde{\phi}_{s,1}\right) + (\lambda_s + 2\mu_s)\partial_z \widetilde{\phi}_{s,1} + 2\mu_s \cdot \left(\partial_z \partial_r \widetilde{\psi}_{s,1} + \frac{1}{r}\partial_z \widetilde{\psi}_{s,1}\right). \tag{5.18}$$

$$\widetilde{\sigma}_{zz,2} = \lambda_s \cdot \left(\partial_r^2 \widetilde{\phi}_{s,2} + \frac{1}{r}\partial_r \widetilde{\phi}_{s,2}\right) + (\lambda_s + 2\mu_s) \cdot \frac{1}{\varepsilon(z)}\partial_z \left(\frac{\partial_z \widetilde{\phi}_{s,2}}{\varepsilon(z)}\right) + 2\mu_s \cdot \left(\frac{1}{\varepsilon(z)}\partial_z \partial_r \widetilde{\psi}_{s,2} + \frac{1}{r}\partial_z \widetilde{\psi}_{s,2}\right). \tag{5.19}$$

The shear stress fields $\widetilde{\sigma}_{zr,i}$ $(i=1,2)$ are:

$$\widetilde{\sigma}_{zr,1} = \mu_s \left(2\partial_r \partial_z \widetilde{\phi}_{s,1} - \partial_z^2 \widetilde{\psi}_{s,1} + \partial_r^2 \widetilde{\psi}_{s,1} + \frac{1}{r}\partial_r \widetilde{\psi}_{s,1} - \frac{1}{r^2}\widetilde{\psi}_{s,1}\right) \tag{5.20}$$

$$\widetilde{\sigma}_{zr,2} = \mu_s \left(\frac{1}{\varepsilon(z)} \cdot 2\partial_r \partial_z \widetilde{\phi}_{s,2} - \frac{1}{\varepsilon(z)}\partial_z \left(\frac{\partial_z \widetilde{\psi}_{s,2}}{\varepsilon(z)}\right)\partial_r^2 \widetilde{\psi}_{s,2} + \frac{1}{r}\partial_r \widetilde{\psi}_{s,2} - \frac{1}{r^2}\widetilde{\psi}_{s,2}\right). \tag{5.21}$$

For the system in Figure 5.1, the following boundary conditions must be satisfied:

$$\widetilde{\sigma}_{zz,1}(0,r,\omega) = 0 \qquad\qquad \widetilde{\sigma}_{zr,1}(0,r,\omega) = 0 \tag{5.22}$$

$$\tilde{u}_{s,z,2}(\overline{Z}_2,r,\omega) = 0 \qquad\qquad \tilde{u}_{s,r,2}(\overline{Z}_2,r,\omega) = 0 \tag{5.23}$$

$$\tilde{u}_{s,z,1}(Z_1,r,\omega) = \tilde{u}_{s,z,2}(\overline{Z}_1,r,\omega) \qquad \tilde{u}_{s,r,1}(Z_1,r,\omega) = \tilde{u}_{s,r,2}(\overline{Z}_1,r,\omega) \tag{5.24}$$

$$\widetilde{\sigma}_{zz,1}(Z_1,r,\omega) = \widetilde{\sigma}_{zz,2}(\overline{Z}_1,r,\omega) \qquad \widetilde{\sigma}_{zr,1}(Z_1,r,\omega) = \widetilde{\sigma}_{zr,2}(\overline{Z}_1,r,\omega) \tag{5.25}$$

Therefore, a system of equations $\mathbf{MA} = 0$ can be formed after substituting all fields into the boundary conditions. The detailed form of $\mathbf{M}$ is provided in Section A.3 of Appendix A.

Let the determinant of the coefficient matrix $\mathbf{M}$ be zero, which gives the dispersion relation of this scenario:

$$\det \mathbf{M} = 0 \tag{5.26}$$

The roots of Equation (5.26) in the complex k_r plane give all eigenvalues k_r. For any k_{rp}, its corresponding eigenvector $\widetilde{\Phi}_{sp,i}(z)$ and $\widetilde{\Psi}_{sp,i}(z)$ will be computed by imposing an inhomogeneous interface condition.

5.1.2 Discrete solution

Following the implementations introduced by Kausel and de Oliveira Barbosa, the layer thickness in the PML should be modified after complex stretch (see Figure 5.2) in Equation (2.51) when $m_{\text{PML}} = 2$, which is:

$$\bar{h}_\ell = \bar{z}_\ell - \bar{z}_{\ell-1} = H \left\{ \frac{1}{N_{\text{PML}}} - \mathrm{i}\beta_0 \left[\left(\frac{\ell}{N_{\text{PML}}}\right)^3 - \left(\frac{\ell-1}{N_{\text{PML}}}\right)^3\right] \right\}, \tag{5.27}$$

Due to the complex stretch in the PML, the elemental matrix for ℓ–th layer in the PML domain should be modified as:

$$\overline{\mathbf{A}}_\ell = \frac{\bar{h}_\ell}{h_\ell}\mathbf{A}_\ell, \quad \overline{\mathbf{G}}_\ell = \frac{h_\ell}{\bar{h}_\ell}\mathbf{G}_\ell, \quad \overline{\mathbf{M}}_\ell = \frac{\bar{h}_\ell}{h_\ell}\mathbf{A}_\ell, \quad \overline{\mathbf{B}}_\ell = \mathbf{B}_\ell \tag{5.28}$$

Finally, the generalized discrete eigenvalue problem of P-SV modes in the elastic waveguide after the assembly of the matrix in each layer [12]:

$$\left(k_{rp}^2\overline{\mathbf{A}}+\overline{\mathbf{C}}\right)\left[\begin{array}{c}\boldsymbol{\phi}_{rp}\\k_{rp}\boldsymbol{\phi}_{zp}\end{array}\right]=\left[\begin{array}{c}\mathbf{0}\\\mathbf{0}\end{array}\right] \tag{5.29}$$

As shown previously, they satisfy the following orthogonality relations [12]:

$$\mathbf{Y}^T\overline{\mathbf{A}}\mathbf{Z}=\mathbf{K}_{\mathrm{r}},\quad\mathbf{Y}^T\overline{\mathbf{C}}\mathbf{Z}=-\mathbf{K}_{\mathrm{r}}^3, \tag{5.30}$$

The eigenvalues k_{rp} and unnormalized eigenvectors are directly calculated by `np.linalg.eig` in Python. In the next stage, eigenvectors will be normalized by the orthogonality relation $\mathbf{Y}^T\overline{\mathbf{A}}\mathbf{Z}=\mathbf{K}_{\mathrm{r}}$. Besides, the roots with positive imaginary part will be excluded to select the mode that decays in the range direction [12].

5.2 Numerical results and discussions

In this section, the continuous and discrete modal solutions of a linear isotropic elastic layer with one PML will be compared, including their (1) eigenvalues, (2) eigenvectors, and (3) orthogonality. For completeness, we will consider modal solutions for $f = 50\,\mathrm{Hz}$, $f = 200\,\mathrm{Hz}$. Additionally, different attenuation rates α_{s} in the semi-analytical solution, which correspond to material damping ξ_{s} in the Thin-layer method, will be considered. In this section, the numerical results for Group 1.2 is provided and discussed, the results of remaining cases are provided in Appendix.

Table 5.2. Attenuation rates and frequencies used in six cases in Chapter 5

Groups	Attenuation rate		Frequency	
Group 1.1	α_{s}	0 dB/λ	f	50 Hz
Group 1.2	α_{s}	1.5 dB/λ	f	50 Hz
Group 2.1	α_{s}	0 dB/λ	f	200 Hz
Group 2.2	α_{s}	1.5 dB/λ	f	200 Hz

There are 300 layers in the physical domain; therefore, the thickness of the thin layer in the regular domain is fixed to be $1/60$ m. As mentioned, the comparison of continuous and discrete modal solutions will be carried out for different values of h_ℓ

1. $h_\ell = 0.25$ m. In other words, assume a PML with *moderate thickness* (See Figure 5.3a).

2. $h_\ell = 0.01$ m. Under this scenario, we have PML with *minimal thickness* (See Figure 5.3b).
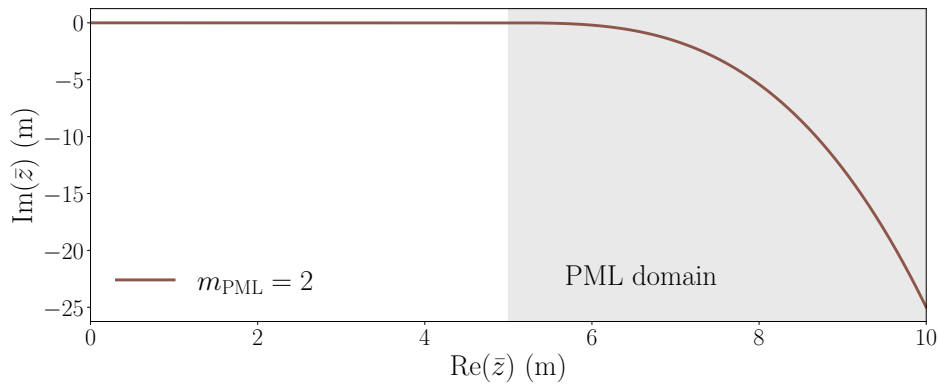

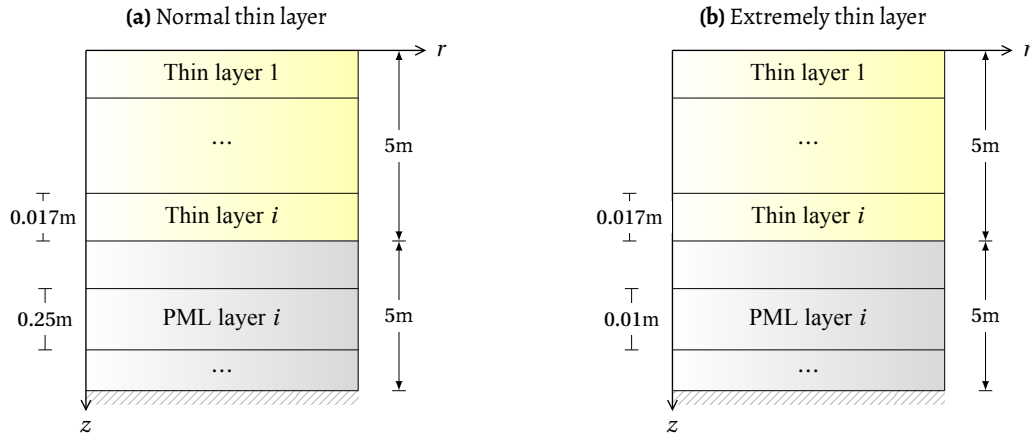**Figure 5.2.** Complex-stretched coordinate $\bar{z}$ in Chapter 5.

Figure 5.3. Schematics of discretizations in TLM with different h_ℓ: (a) 0.25 m, (b) 0.01m.

5.2.1 Eigenvalues

The comparison between eigenvalues for all cases listed in Table 5.2 will be presented. The eigenvalues are compared first globally in the left column of the figures, followed by zoomed-in versions highlighting the eigenvalues that agree perfectly with each other. The first row compares $h_\ell = 0.25$ m, while the second row presents the results for $h_\ell = 0.01$ m. The following observations can be made:

1. For all cases considered here, a small subset of the TLM modes are perfectly consistent with the semi-analytical solution. Beyond this subset, the eigenvalues of the TLM have large imaginary part. In contrast, the semi-analytical eigenvalues are distributed around two hyperbolic curves associated with P-wave and SV-wave type modes.

2. The overall comparison (left-column) and zoomed-in comparison (right column) both suggest that decreasing h_ℓ brings the eigenvalues from two methods into closer agreement.

5.2.2 Eigenvectors

For eigenvalues in perfect agreement, their normalized eigenvectors are compared in Figure 5.5. The normalization for discrete and continuous solutions is based on Equation (5.31) and (5.30), respectively. However, it is subjected to the following modification in the PML domain due to the complex stretch of dz to $d\bar{z} = \varepsilon(z)dz$:

$$
\Gamma_{pq,2} = \Gamma_{p,2}\delta_{pq} = \int_{Z_1}^{Z_2} \varepsilon(z)\left(\zeta_s\, k_p\, \tilde{u}_{s,r,2,p}(\bar{z})\frac{\tilde{u}_{s,r,2,q}(\bar{z})}{k_{rq}} - \eta_s\cdot\tilde{u}_{s,r,2,p}(\bar{z})\frac{\tilde{\sigma}_{s,zz,2,q}(\bar{z})}{k_{rp}} \right.
$$
$$
\left. +\tilde{u}_{s,z,2,p}(\bar{z})\frac{\tilde{\sigma}_{s,zr,2,q}(\bar{z})}{k_{rq}}\right)dz, \tag{5.31}
$$

where $\zeta_s = \rho_s\cdot\left[c_L^4 - (c_L^2 - 2\cdot c_T^2)^2\right]\big/c_L^2$ and $\eta_s = \left(c_L^2 - 2c_T^2\right)\big/c_L^2$.

The observations are made as follows:

1. The spatial profiles of modes obtained from the two approaches match each other exactly.

2. Modes demonstrate an exponentially increasing profile initially. As they reach the lower part of the PML, their modal amplitude are attenuated, attributed to the relatively high value of the quadratic attenuation function $\beta(s)$ near the fixed boundary of the PML domain ($z = Z_2$).
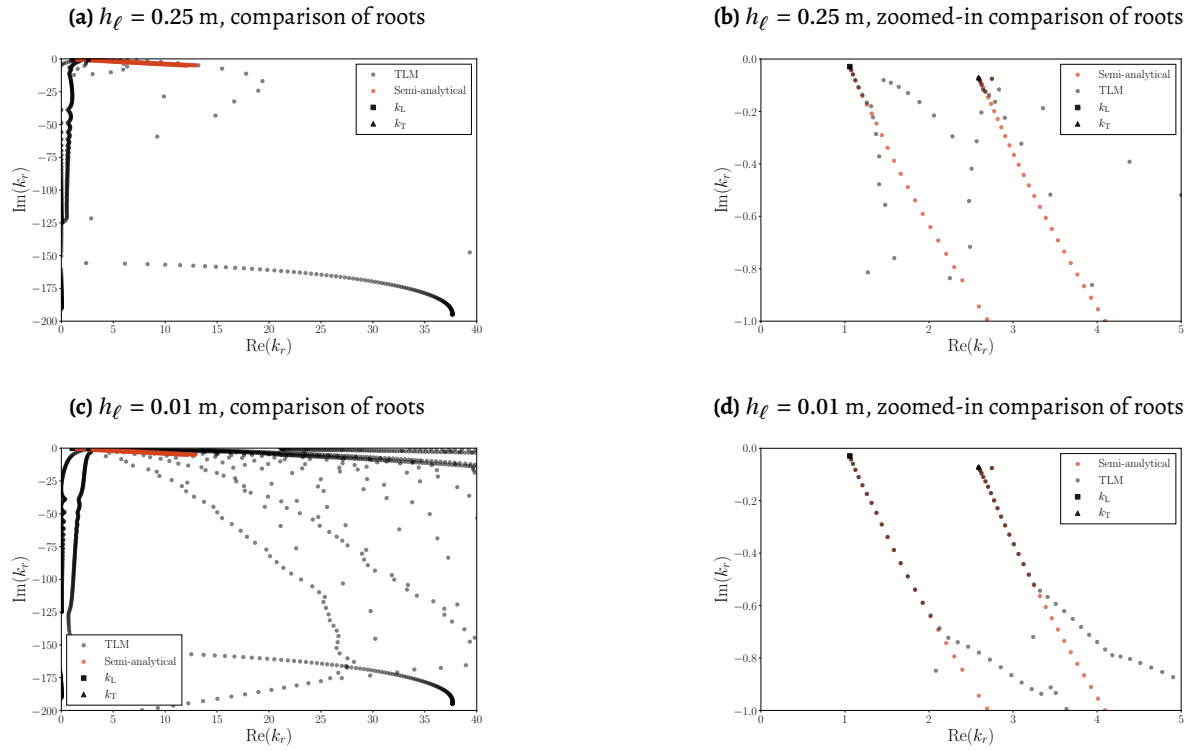
(a) $h_\ell = 0.25$ m, comparison of roots

(b) $h_\ell = 0.25$ m, zoomed-in comparison of roots

(c) $h_\ell = 0.01$ m, comparison of roots

(d) $h_\ell = 0.01$ m, zoomed-in comparison of roots

Figure 5.4. Comparison of eigenvalues obtained via semi-analytical approach(red circles) and TLM (black crosses) for $f = 50$Hz, $\alpha_s = 1.5$ dB$/\lambda$: (a) and (b): $h_\ell = 0.25$ m; (c) and (d): $h_\ell = 0.01$ m.
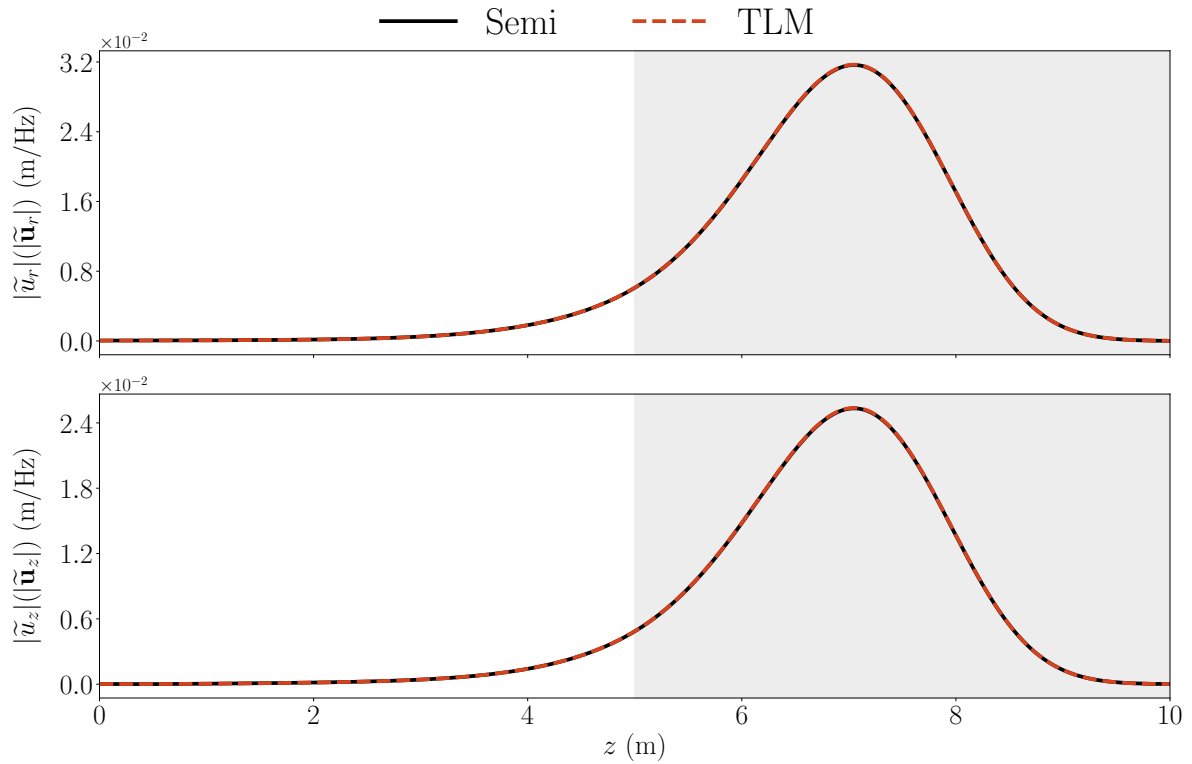

Figure 5.5. Comparison of eigenvectors obtained via semi-analytical approach (black-continuous line) and TLM (red-dashed line), and grey domain indicates the PML for $f = 50$Hz, $\alpha_s = 1.5$ dB$/\lambda$

5.2.3 Modal orthogonality

Figure 5.6 demonstrates the value of $|\Gamma_{pq}|$ of the first forty normalized modes computed from the semi-analytical solution for $f = 50$ Hz and $\alpha_{\mathrm{s}} = 1.5dB/\lambda$. The vertical axis corresponds to mode number p, and the horizontal axis to mode number q. In all cases, the off-diagonal terms are zero, indicating that the modes are orthogonal.

On the other hand, the $\log_{10}|\Gamma_{pq}|$ at 50 Hz between modes obtained via TLM is displayed in Figure 5.7. The figure in the left column represents results when $h_\ell = 0.25$ m, where an acceptable orthogonality can be found via zero off-diagonal elements; However, the orthogonality is violated if a $h_\ell = 0.01$ m is chosen, indicated by non-zero off diagonal elements in 5.7b. From this point of view, small h_ℓ in the TLMs with PML should not be suggested due to the violated orthogonality. Modal orthogonality plots at other frequencies are provided in Appendix D.
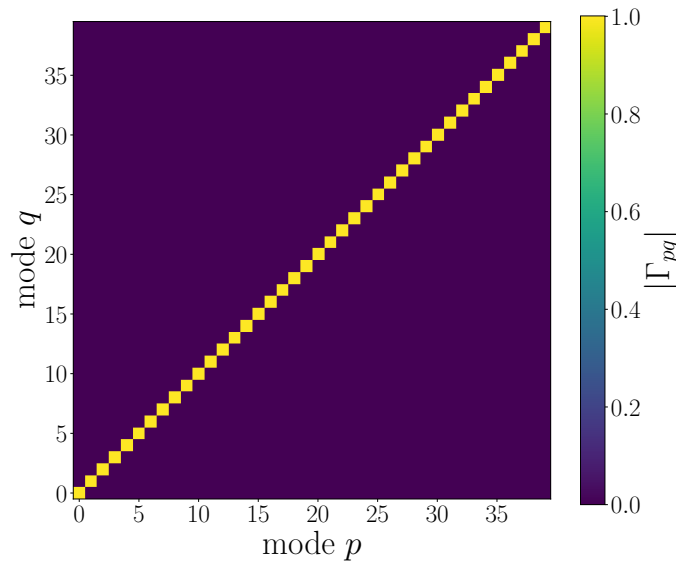

Figure 5.6. Orthogonality heatmap of first forty modes at $f = 50$ Hz and $\alpha_{\mathrm{s}} = 1.5dB/\lambda$.

(a) $\alpha_{\mathrm{s}} = 1.5dB/\lambda$, $f = 50$ Hz, $h_\ell = 0.25$ m   **(b)** $\alpha_{\mathrm{s}} = 1.5dB/\lambda$, $f = 50$ Hz, $h_\ell = 0.01$ m
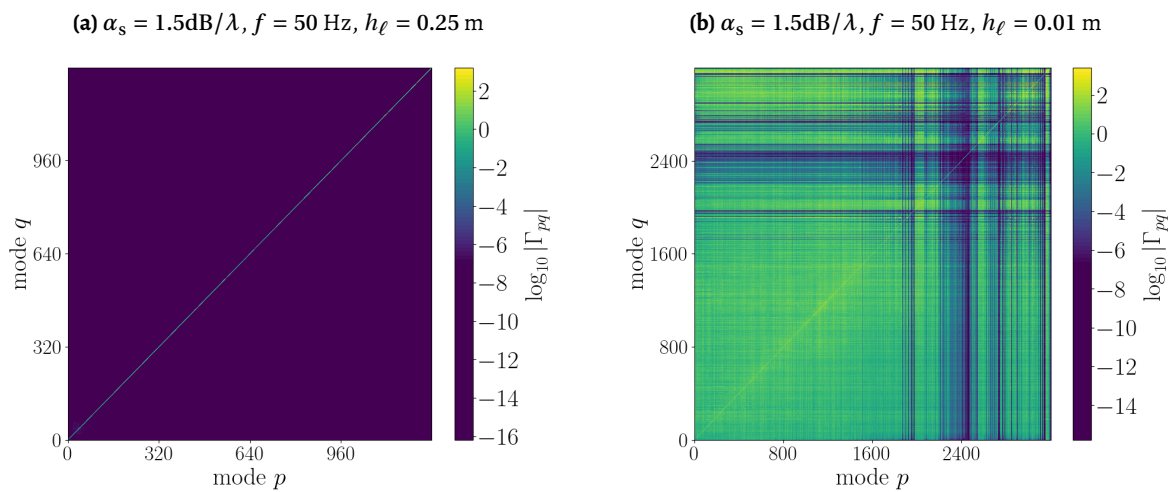

Figure 5.7. Orthogonality heatmaps of all modes obtained via TLM: left column: good orthogonality when $h_\ell = 0.25$ m, right column: violated orthogonality when $h_\ell = 0.01$ m.

5.2.4 Dispersion characteristics

The forty-six selected curves in Figure 5.8 illustrate the dispersion characteristics of the single elastic layer with one PML (see Figure 5.1) obtained via the semi-analytical solution, for frequencies ranging from 0 to 50 Hz. The black curves represent the first twenty-one modes (ranked by ascending $\mathrm{Re}(k_r)$) near the k_L branch, while the red curves represent the remaining twenty-five modes associated with the k_T branch. As can be observed:

1. Figure 5.8 and 5.9 demonstrate that all modes experience high group velocities across all frequencies.

2. As shown in Figure 5.9a and 5.9b: With increasing ω, the decreasing group velocity. Furthermore, the first two spectra (from left to right) of group velocities in Figure 5.9a exhibit non-monotonic variation in certain frequency intervals, and they touch each other. These findings are opposite to the profile of the group and phase velocity of the physical modes, which is indicated by Figure 2.8.

3. The phase velocities are lower than the group velocity, which follows the definition of *anomalous dispersion* given by Miklowitz in [14]. This also reveals the non-physical character of Bérenger modes.
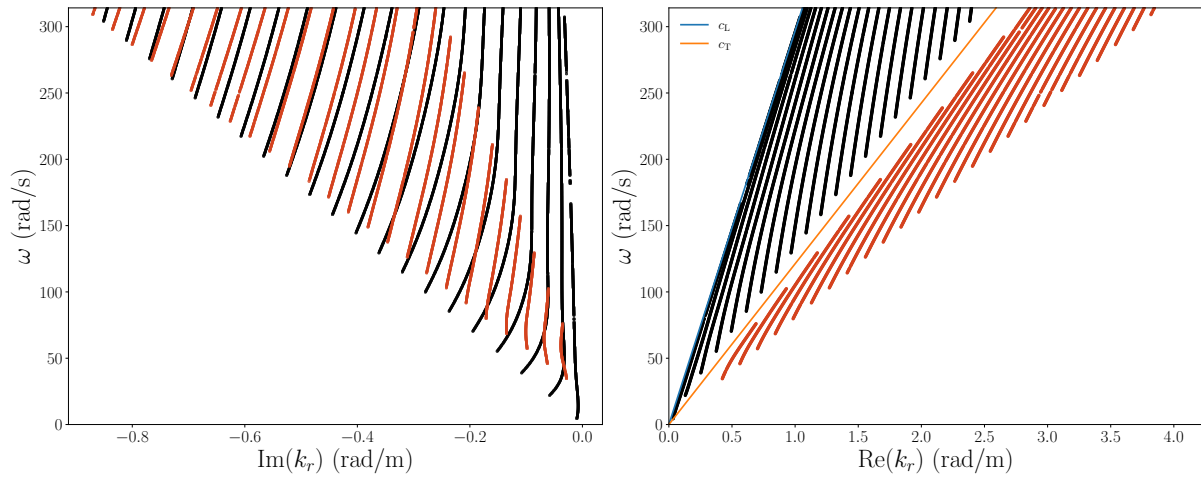

Figure 5.8. Dispersion curves of the first twenty-one Bérenger modes near the k_L branch (black continuous lines) and the first twenty-five modes (red continuous lines) near the k_T branch (ranked by ascending $\mathrm{Re}(k_r)$).

(a) Bérenger modes near k_L branch   **(b)** Bérenger modes near k_T branch
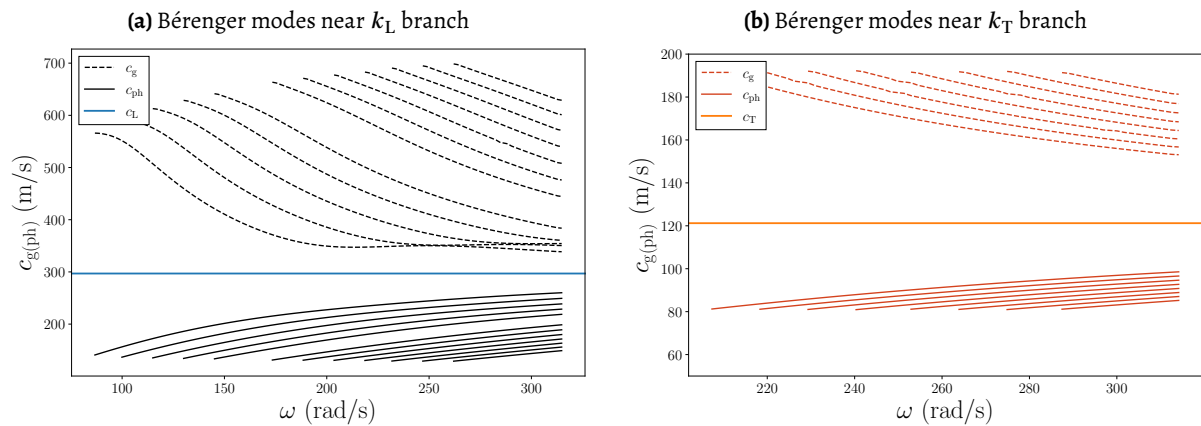
Figure 5.9. Group and phase velocity spectra of the last twelve Bérenger modes near the k_L branch (black lines) and the last eigen Bérenger modes near the k_L branch (red lines).

5.3 Summary

This chapter compares the continuous and discrete modal solutions of the elastic waveguide with PML shown in Figure 5.1. The primary conclusions are summarized as follows:

1. Unlike the single elastic waveguide, the eigenvalues obtained from semi-analytical and TLM suggest significant differences for the case with one perfectly matched layer. Overall, most of the modes from TLM are evanescent with a big imaginary parts. However, the eigenvalues obtained from the semi-analytical solution are distributed along a hyperbolic line in the complex k_r plane near the real axis. Two categories of solutions are convergent to each other if the h_ℓ is tiny.

2. The matched eigenvalues' related modes are in excellent agreement. Furthermore, they share precisely the same characteristics regarding spatial profiles with the Bérenger modes of one acoustic layer with one PML: An intensely exponential increasing before decreasing near the end of the PML domain. Consequently, the central part of their non-zero parts is found inside the PML domain.

3. The modal orthogonality between the normalized Bérenger modes of the semi-analytical modes is well observed, although a relatively small dz is still suggested to give accurate results.

4. For the TLM approach, the modes are acceptable when $h_\ell = 0.25$ m is used. However, the orthogonality condition deteriorates if h_ℓ is reduced to $h_\ell = 0.01$ m. Therefore, it is not suggested to use too many layers in the TLM solition with PML for maintaining cross-orthogonality.

5. For the single elastic layer with PML, obtained Berenger modes via semi-analytical solution demonstrate anomalous dispersion characteristics: (1) A large group velocity across all frequencies, and the group velocity is always larger than the phase velocity. (2) The *non-monotonic variation* of the group velocity spectras are found for two modes near the k_L branch. These anomalous dispersion characteristics imply the non-physical nature of the Bérenger modes, which are introduced by the nonphysical perfectly matched layer.

6

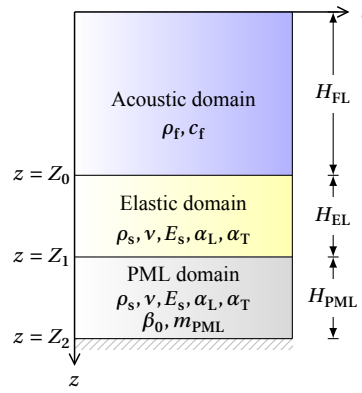# Modal Solution of one Acousto-elastic Domain with a PML via Semi-analytical method

Figure 6.1. Schematic of an acousto-elastic layer with one PML.

Table 6.1. Basic parameters used for numerical examples in Chapter 6

Fluid layer thickness	H_{FL}	20	m
Elastic layer thickness	H_{EL}	5	m
PML layer thickness	H_{PML}	5	m
Fluid density	ρ_f	1000	kg/m^3
Fluid Media Wave Speed	c_f	1500	kg/m^3
Solid density	ρ_s	1700	kg/m^3
Young's modulus	E_s	0.7	MPa
Poisson's ratio	ν	0.4	–
Attenuation rate	α_s	1.5	dB/λ
Attenuation coefficient	β_0	5	–
PML order	m_{PML}	2	–

This chapter provides a semi-analytical modal solution for the system depicted in Figure 6.1. As shown in the figure, the physical domain consists of a coupled acousto-elastic layer, where the acoustic layer has a height of H_{FL} and the elastic domain has a height of H_{EL}. This two-layered system is extended with a PML having a height of H_{PML}. The PML is assumed to be an elastic layer with material properties consistent with those of the elastic domain above it.

The eigenvalue problem is formulated analytically. Subsequently, the roots of the dispersion relation are found numerically through a root-finding algorithm. The eigenvectors are then computed and normalized based on orthogonality relations. Besides, the cross-orthogonality between the normalized modes is examined. Finally, the dispersion characteristics of modes will be discussed.

6.1 Formulation of eigenvalue problem

6.1.1 Acoustic domain

In an *axisymmetric cylindrical coordinate system*, the Helmholtz equation in the acoustic layer is given as:

$$\nabla^2 \widetilde{\phi}_{f,1} + \frac{\omega^2}{c_f^2} \widetilde{\phi}_{f,1} = 0 \qquad\qquad 0 < z < Z_0 \qquad\qquad (6.1)$$

where the Laplacian operator ∇^2 is:

$$\nabla^2 = 1/r \partial_r (r \partial_r) \mathbf{e}_r + \partial_z^2 \mathbf{e}_z. \qquad\qquad (6.2)$$

The general solution of this Equation (6.1) is given as:

$$\widetilde{\phi}_{f,1}(r,z,\omega) = H_0^{(2)}(k_r r) \left[A_1 \exp\left(i\gamma_f z \right) + A_2 \exp\left(-i\gamma_f(z - Z_0) \right) \right] \qquad\qquad (6.3)$$

where $\gamma_f(\omega) = \sqrt{\omega^2/c_f^2 - k_r^2}$.

Besides, the velocity and pressure fields are based on the potential field $\widetilde{\phi}_{f,1}$:

$$\widetilde{p}_{f,1}(r,z,\omega) = -i\omega \rho_f \widetilde{\phi}_{f,1} \qquad\qquad (6.4)$$

The velocity field is given as

$$\widetilde{\mathbf{v}}_1(r,z,\omega) = \nabla \widetilde{\phi}_{f,1} \qquad\qquad (6.5)$$

$$\nabla = \partial_r \mathbf{e}_r + \partial_z \mathbf{e}_z. \qquad\qquad (6.6)$$

6.1.2 Elastic domain

The Helmholtz equations of *the elastic domain* read:

$$\nabla^2 \widetilde{\phi}_{s,2} + \frac{\omega^2}{c_L^2} \widetilde{\phi}_{s,2} = 0 \qquad\qquad Z_0 < z < Z_1. \qquad\qquad (6.7)$$

$$\nabla^2 \widetilde{\psi}_{s,2} - \frac{\widetilde{\psi}_{s,2}}{r^2} + \frac{\omega^2}{c_T^2} \widetilde{\psi}_{s,2} = 0, \qquad\qquad Z_0 < z < Z_1. \qquad\qquad (6.8)$$

where the Laplacian operator ∇^2 is:

$$\nabla^2 = 1/r \partial_r (r \partial_r) + \partial_z^2. \qquad\qquad (6.9)$$

Again, the general solution of the Helmholtz equations in the elastic domain is given as:

$$\widetilde{\phi}_{s,2}(r,z,\omega) = H_0^{(2)}(k_r r) \left[A_3 \exp\left(i\gamma_L(z - Z_0) \right) + A_4 \exp\left(-i\gamma_L(z - Z_1) \right) \right] \qquad\qquad (6.10)$$

$$\widetilde{\psi}_{s,2}(r,z,\omega) = H_0^{(1)}(k_r r) \left[A_5 \exp\left(i\gamma_T(z - Z_0) \right) + A_6 \exp\left(-i\gamma_T(z - Z_1) \right) \right] \qquad\qquad (6.11)$$

where $\gamma_L(\omega) = \sqrt{\omega^2/c_L^2 - k_r^2}$ and $\gamma_T(\omega) = \sqrt{\omega^2/c_T^2 - k_r^2}$.

The post-processed displacement field vector $\tilde{\mathbf{u}}_{\mathrm{s},1}$ in the elastic layer read:

$$\tilde{\mathbf{u}}_{\mathrm{s},2} = \left(\partial_r \widetilde{\phi}_{\mathrm{s},2} - \partial_z \widetilde{\psi}_{\mathrm{s},2} \right) \mathbf{e}_r + \left(\partial_z \widetilde{\phi}_{\mathrm{s},2} + \partial_r \widetilde{\psi}_{\mathrm{s},2} + \widetilde{\psi}_{\mathrm{s},2}/r \right) \mathbf{e}_z. \tag{6.12}$$

The vertical stress field $\widetilde{\sigma}_{zz,2}$ in the elastic domain is given as:

$$\widetilde{\sigma}_{zz,2} = \lambda_{\mathrm{s}} \cdot \left(\partial_r^2 \widetilde{\phi}_{\mathrm{s},2} + \frac{1}{r} \partial_r \widetilde{\phi}_{\mathrm{s},2} \right) + (\lambda_{\mathrm{s}} + 2\mu_{\mathrm{s}}) \, \partial_z \widetilde{\phi}_{\mathrm{s},2} + 2\mu_{\mathrm{s}} \cdot \left(\partial_z \partial_r \widetilde{\psi}_{\mathrm{s},2} + \frac{1}{r} \partial_z \widetilde{\psi}_{\mathrm{s},2} \right). \tag{6.13}$$

The shear stress field $\widetilde{\sigma}_{zr,2}$ in the elastic domain is given as:

$$\widetilde{\sigma}_{zr,2} = \mu_{\mathrm{s}} \left(2\partial_r \partial_z \widetilde{\phi}_{\mathrm{s},2} - \partial_z^2 \widetilde{\psi}_{\mathrm{s},2} + \partial_r^2 \widetilde{\psi}_{\mathrm{s},2} + \frac{1}{r} \partial_r \widetilde{\psi}_{\mathrm{s},2} - \frac{1}{r^2} \widetilde{\psi}_{\mathrm{s},2} \right) \tag{6.14}$$

6.1.3 PML domain

The Helmholtz equations in the PML domain reads:

$$\overline{\nabla}^2 \widetilde{\phi}_{\mathrm{s},3} + \frac{\omega^2}{c_{\mathrm{L}}^2} \widetilde{\phi}_{\mathrm{s},3} = 0 \qquad\qquad Z_1 < z < Z_2. \tag{6.15}$$

$$\overline{\nabla}^2 \widetilde{\psi}_{\mathrm{s},3} - \frac{\widetilde{\psi}_{\mathrm{s},3}}{r^2} + \frac{\omega^2}{c_{\mathrm{T}}^2} \widetilde{\psi}_{\mathrm{s},3} = 0, \qquad\qquad Z_1 < z < Z_2. \tag{6.16}$$

where the Laplacian operator $\overline{\nabla}^2$ is:

$$\overline{\nabla}^2 = 1/r \partial_r (r \partial_r) + 1/\varepsilon(z) \cdot \partial_z (\partial_z / \varepsilon(z)). \tag{6.17}$$

Using quadratic polynomial attenuation function $\beta(z)$ in the PML domain, the complex stretch function $\varepsilon(z)$ reads

$$\varepsilon(z) = 1 - 3\mathrm{i}\beta_0 \left(\frac{z - Z_1}{H_{\mathrm{PML}}} \right)^2 \tag{6.18}$$

Therefore, the general solutions of the Helmholtz equations in the PML domain are:

$$\widetilde{\phi}_{\mathrm{s},3}(r, \bar{z}, \omega) = H_0^{(2)}(k_r r) \left[A_7 \exp\left(\mathrm{i}\gamma_{\mathrm{L}}(\bar{z} - \overline{Z}_1) \right) + A_8 \exp\left(-\mathrm{i}\gamma_{\mathrm{L}}(\bar{z} - \overline{Z}_2) \right) \right] \tag{6.19}$$

$$\widetilde{\psi}_{\mathrm{s},3}(r, \bar{z}, \omega) = H_0^{(1)}(k_r r) \left[A_9 \exp\left(\mathrm{i}\gamma_{\mathrm{T}}(\bar{z} - \overline{Z}_1) \right) + A_{10} \exp\left(-\mathrm{i}\gamma_{\mathrm{T}}(\bar{z} - \overline{Z}_2) \right) \right] \tag{6.20}$$

Where $\bar{z}$ denotes the complex-stretched coordinate in the PML domain:

$$\bar{z} = z - \mathrm{i}\beta_0 H_{\mathrm{PML}} \left(\frac{z - H_{\mathrm{EL}}}{H_{\mathrm{PML}}} \right)^3 \qquad Z_1 < z < Z_2 \tag{6.21}$$

Incorporating the complex stretch, field vector $\tilde{\mathbf{u}}_{\mathrm{s},3}$ in the PML is

$$\tilde{\mathbf{u}}_{\mathrm{s},3} = \left(\partial_r \widetilde{\phi}_{\mathrm{s},3} - \partial_z \widetilde{\psi}_{\mathrm{s},3}/\varepsilon(z) \right) \mathbf{e}_r + \left(\partial_z \widetilde{\phi}_{\mathrm{s},3}/\varepsilon(z) + \partial_r \widetilde{\psi}_{\mathrm{s},3} + \widetilde{\psi}_{\mathrm{s},3}/r \right) \mathbf{e}_z. \tag{6.22}$$

Furthermore, the vertical stress field $\widetilde{\sigma}_{zz,3}$ is given as:

$$\widetilde{\sigma}_{zz,3} = \lambda_{\mathrm{s}} \cdot \left(\partial_r^2 \widetilde{\phi}_{\mathrm{s},3} + \frac{1}{r} \partial_r \widetilde{\phi}_{\mathrm{s},3} \right) + (\lambda_{\mathrm{s}} + 2\mu_{\mathrm{s}}) \cdot \frac{1}{\varepsilon(z)} \partial_z \left(\frac{\partial_z \widetilde{\phi}_{\mathrm{s},3}}{\varepsilon(z)} \right) + 2\mu_{\mathrm{s}} \cdot \left(\frac{1}{\varepsilon(z)} \partial_z \partial_r \widetilde{\psi}_{\mathrm{s},3} + \frac{1}{r} \partial_z \widetilde{\psi}_{\mathrm{s},3} \right). \tag{6.23}$$

Finally, the shear stress field $\widetilde{\sigma}_{zr,3}$ is given as:

$$\widetilde{\sigma}_{zr,3} = \mu_{\mathrm{s}} \left(\frac{1}{\varepsilon(z)} \cdot 2\partial_r \partial_z \widetilde{\phi}_{\mathrm{s},3} - \frac{1}{\varepsilon(z)} \partial_z \left(\frac{\partial_z \widetilde{\psi}_{\mathrm{s},3}}{\varepsilon(z)} \right) \partial_r^2 \widetilde{\psi}_{\mathrm{s},3} + \frac{1}{r} \partial_r \widetilde{\psi}_{\mathrm{s},3} - \frac{1}{r^2} \widetilde{\psi}_{\mathrm{s},3} \right). \tag{6.24}$$

6.1.4 Boundary and interface conditions

Modes of the system in Figure 6.1 are supposed to satisfy the following boundary and interface conditions:

$$\widetilde{p}_{\text{f},1}(r,0,\omega) = 0, \tag{6.25}$$

$$\widetilde{\sigma}_{zr,2}(r,Z_0,\omega) = 0, \tag{6.26}$$

$$\widetilde{p}_{\text{f},1}(r,Z_0,\omega) = -\widetilde{\sigma}_{zz,2}(r,Z_0,\omega), \qquad \widetilde{v}_{z,1}(r,Z_0,\omega) = \mathrm{i}\omega u_{\text{s},2,z}(r,Z_0,\omega), \tag{6.27}$$

$$\widetilde{u}_{z,2}(r,Z_1,\omega) = \widetilde{u}_{z,3}(r,\overline{Z}_1,\omega), \qquad \widetilde{u}_{r,2}(r,Z_1,\omega) = \widetilde{u}_{r,3}(r,\overline{Z}_1,\omega), \tag{6.28}$$

$$\widetilde{\sigma}_{zz,2}(r,Z_1,\omega) = \widetilde{\sigma}_{zz,3}(r,\overline{Z}_1,\omega), \qquad \widetilde{\sigma}_{zr,2}(r,Z_1,\omega) = \widetilde{\sigma}_{zr,3}(r,\overline{Z}_1,\omega), \tag{6.29}$$

$$\widetilde{u}_{z,3}(r,\overline{Z}_2,\omega) = 0, \qquad \widetilde{u}_{r,3}(r,\overline{Z}_2,\omega) = 0. \tag{6.30}$$

The substitution of all assumed general solutions into the ten boundary conditions will give the following system of equations:

$$\mathbf{MA} = \mathbf{0}. \tag{6.31}$$

Then the dispersion relation is given by setting the determinant of the $\mathbf{M}$ to zero:

$$\det \mathbf{M} = 0. \tag{6.32}$$

The detailed form of the matrix M is provided in Section A.4 of Appendix A.

6.2 Numerical values and discussions

This section will consider f = 50 Hz, 100 Hz, and 150 Hz. The material properties of the considered system are listed in Table 6.1; they are fixed in the numerical examples.

6.2.1 Eigenvalues

The root-finding algorithm has successfully detected the roots of Equation (6.32). We provide a zero-contour plot of the real and imaginary part of det $\mathbf{M}$ as Figure 6.2. The figure suggests the roots of the dispersion relations have been detected at f = 50 Hz. Besides, the spectrum of the eigenvalues at the three considered frequencies, the primary observations are made as follows:

1. Three types of modes can be identified. First, evanescent modes are found near the imaginary axis. Second, propagative modes are observed near the real axis. FinBérengerrenger modes are distributed along two hyperbolas.

2. With increasing frequency, the number of propagating modes increases. Furthermore, Bérenger modes migrate along translated hyperbolic curves that pass through the enhanced values of k_{L} and k_{T}, respectively.
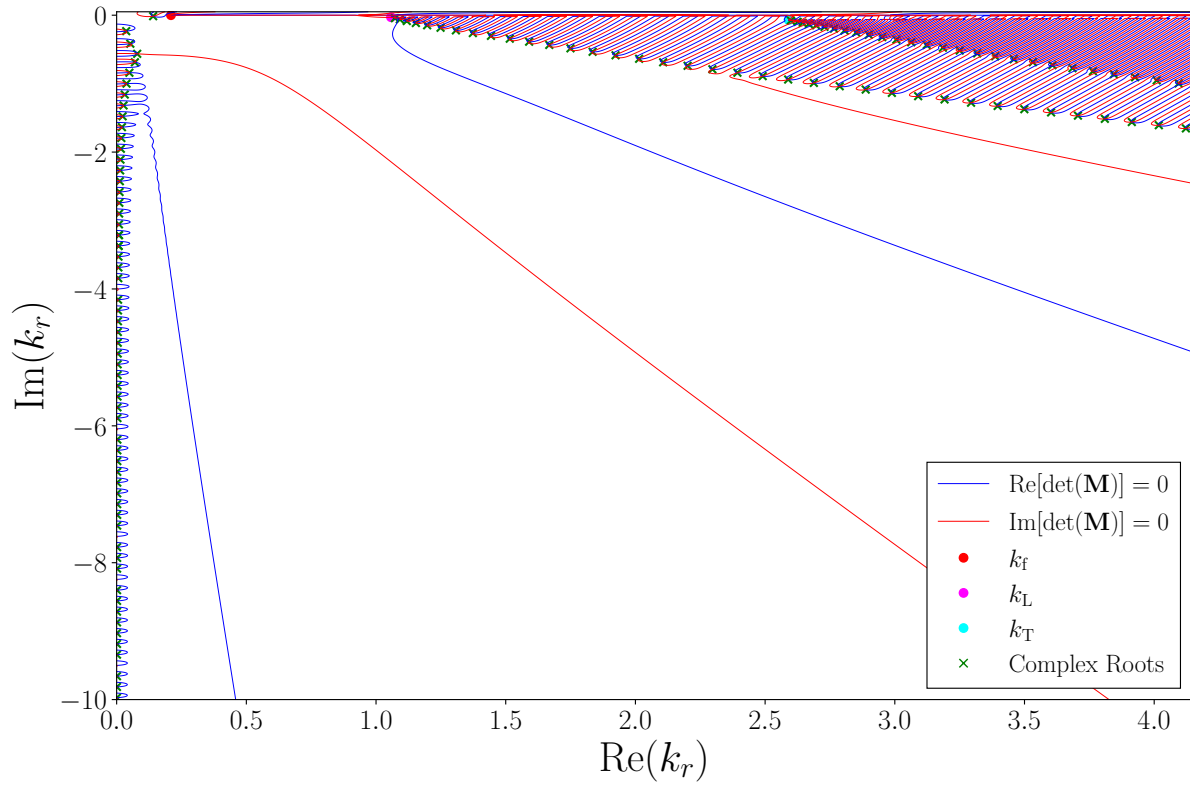
Figure 6.2. Zero-contour plot of $\det(k_r)$ for $f = 50$Hz

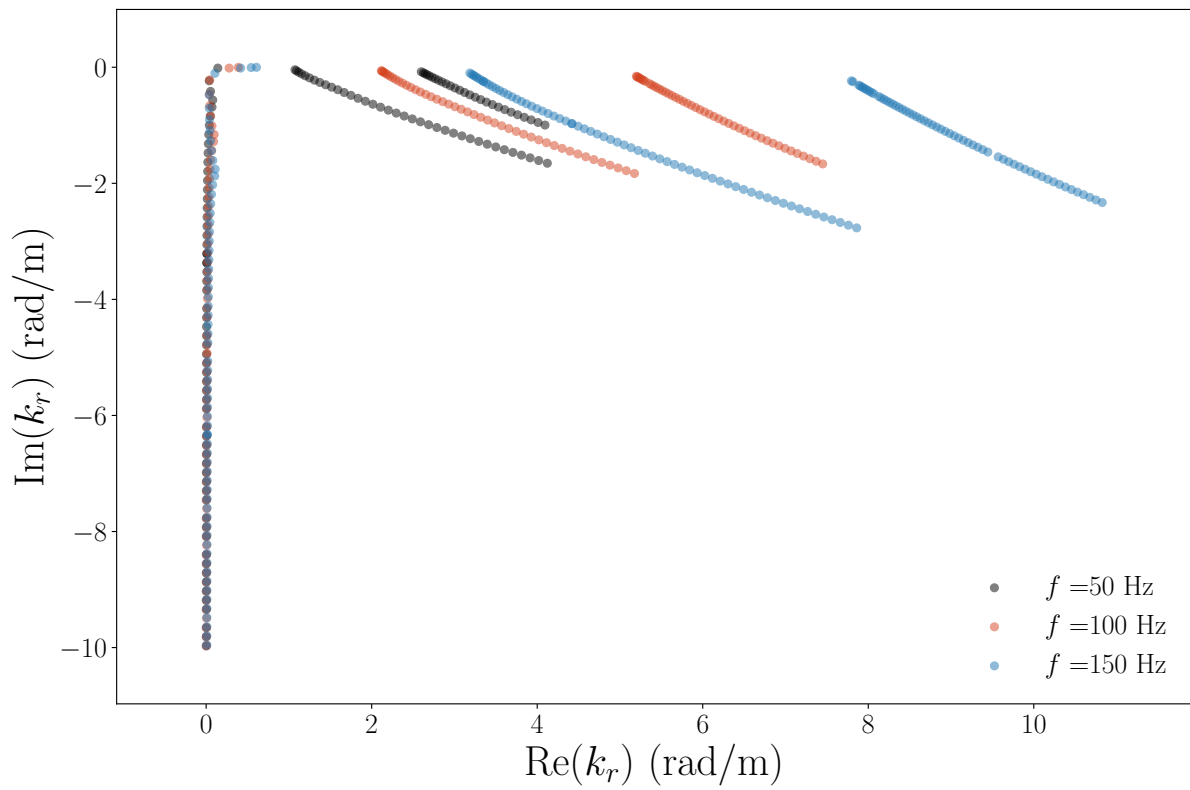**Figure 6.3.** Spectrum of roots at $f = 50$ Hz (black circles), $f = 100$ Hz (red circles) and $f = 150$ Hz (blue circles)

6.2.2 Modal orthogonality

The orthogonality for the acousto-elastic waveguide was given as Equation (3.25) in [21], which can be modified to include the acoustic layer:

$$
\Gamma_{pq} = \Gamma_p \delta_{pq} = \underbrace{- \int_0^{Z_0} \frac{\tilde{v}_{1,r,q}(z)}{i\omega k_{r,q}} \tilde{p}_{f,1}(z)\, dz}_{\text{Fluid layer}}
$$

$$
\underbrace{+ \int_{Z_0}^{Z_1} \zeta_s\, k_p\, \tilde{u}_{s,r,p}(z) \frac{\tilde{u}_{s,r,q}(z)}{k_{r,q}} + \eta_s \cdot u_{s,r,p}(z) \frac{\sigma_{s,zz,q}(z)}{k_{r,p}} - u_{s,z,p}(z) \frac{\sigma_{s,zr,q}(z)}{k_{r,q}}\, dz}_{\text{Elastic layer}} \qquad (6.33)
$$

$$
\underbrace{+ \int_{Z_1}^{Z_2} \zeta_s\, k_p\, \tilde{u}_{s,r,p}(z) \frac{\tilde{u}_{s,r,q}(z)}{k_{r,q}} + \eta_s \cdot u_{s,r,p}(z) \frac{\sigma_{s,zz,q}(z)}{k_{r,p}} - u_{s,z,p}(z) \frac{\sigma_{s,zr,q}(z)}{k_{r,q}}\, d\bar{z}}_{\text{PML}}
$$

The difference between the second and third integration comes from the complex-stretch function $\varepsilon(z)$:

$$
dz \rightarrow d\bar{z} = \varepsilon(z)dz \qquad (6.34)
$$

The values of $(|\Gamma_{pq}|)$ in Equation (6.33) are shown shown in Figure 6.5, the horizontal axis is p and the vertical axis represents q. Figure 6.5 illustrates that the first 100 modes are orthogonal when $f = 50$ Hz by the zero off-diagonal elements. The orthogonality condition for the remaining two frequencies are given in Appendix E.
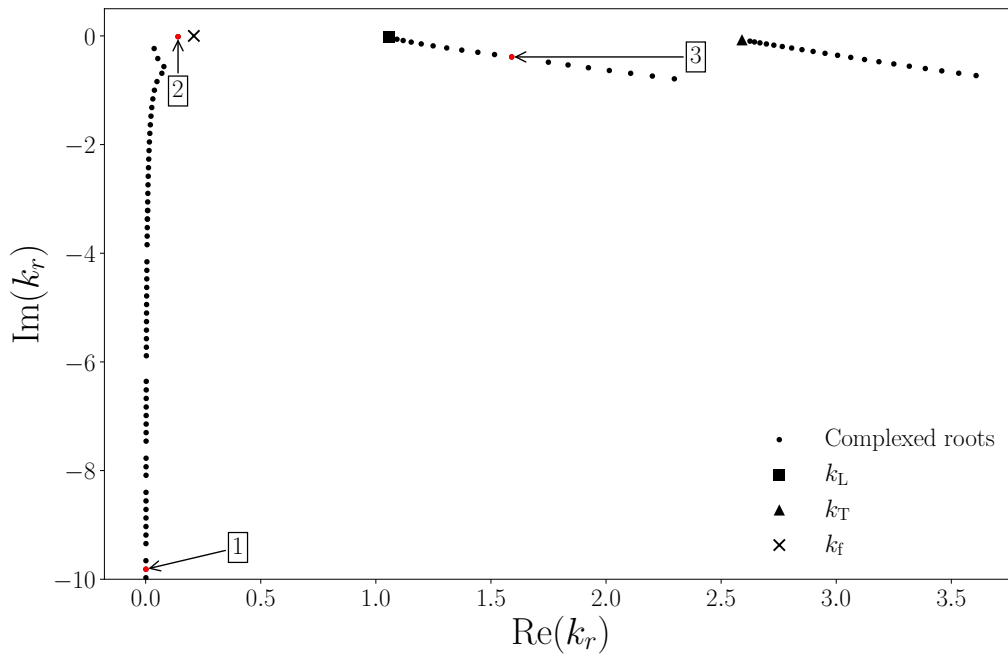
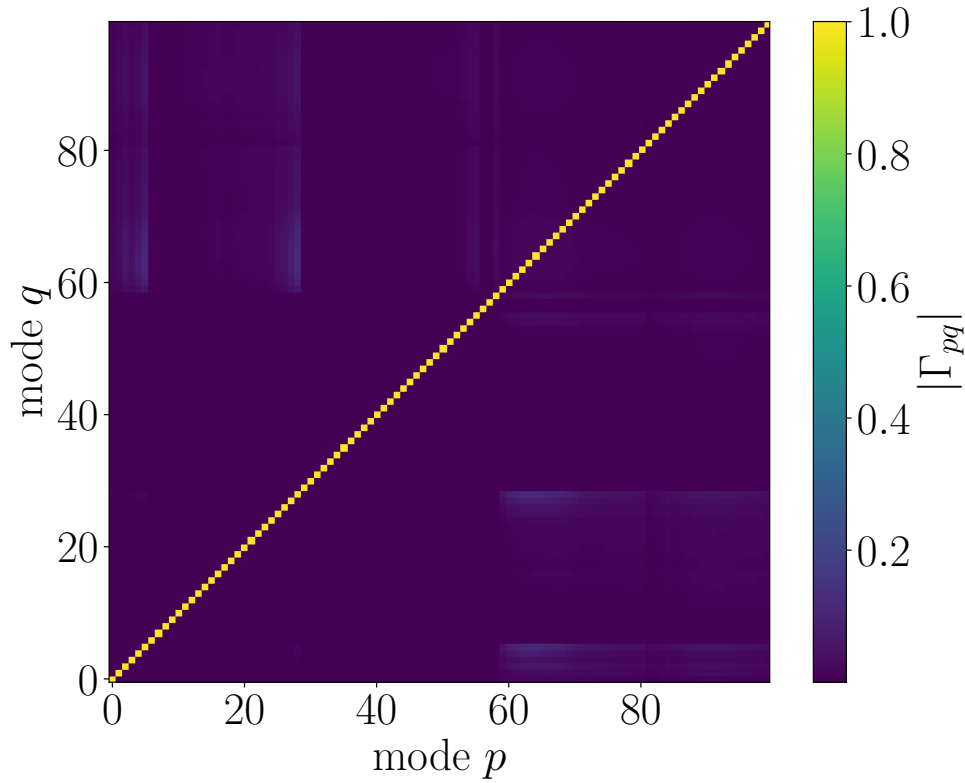**Figure 6.4.** Roots of Equation (6.32) at $f = 50$ Hz.

Figure 6.5. Orthogonality of the first 100 modes of the acousto-elastic layer with one PML at $f = 50$ Hz.

6.2.3 Eigenvectors

All eigenvectors will be normalized such that $\left|\Gamma_{pp}\right| = 1$. The following figure shows the modal amplitude of the pressure field and vertical displacement field for three modes. The result of 50 Hz is provided in Figure 6.6 and 6.6, but similar observations of *modal behavior* were found for 100 Hz and 150 Hz (provided in Appendix E), as given below:

1. *Evanescent modes* exhibit harmonic amplitude in the acoustic domain but sharp amplitude growth in the elastic domain, with proper attenuation in the PML before reaching boundaries. Their eigenvalues have large imaginary parts and nearly zero real parts. In the fluid domain, the real wavenumber k_{f} yields real vertical wavenumber $\gamma_{\mathrm{f}} = \sqrt{k_{\mathrm{f}}^2 - k_r^2}$, producing harmonic behavior. In the elastic domain, complex wavenumbers k_{L} and k_{T} generate large imaginary parts in γ_{L} and γ_{T}, causing exponential amplitude growth. Physically, their radial wavenumber with small real parts in the elastic layer creates steep incident angles, becoming leaky before attenuation in the PML.

2. The eigenvalues of *propagating modes* are near the real axis. Therefore, the vertical wavenumber γ_{f} is a small real number in the fluid domain, leading to harmonic behavior. Due to smaller incident angles, their modal amplitude remains non-leaky in the elastic domain. In the PML domain, modal amplitudes are successfully attenuated before reaching the boundary.

3. The modal shape of Bérenger modes exhibits the aforementioned non-physical behaviors: a significant modal amplitude in the PML.
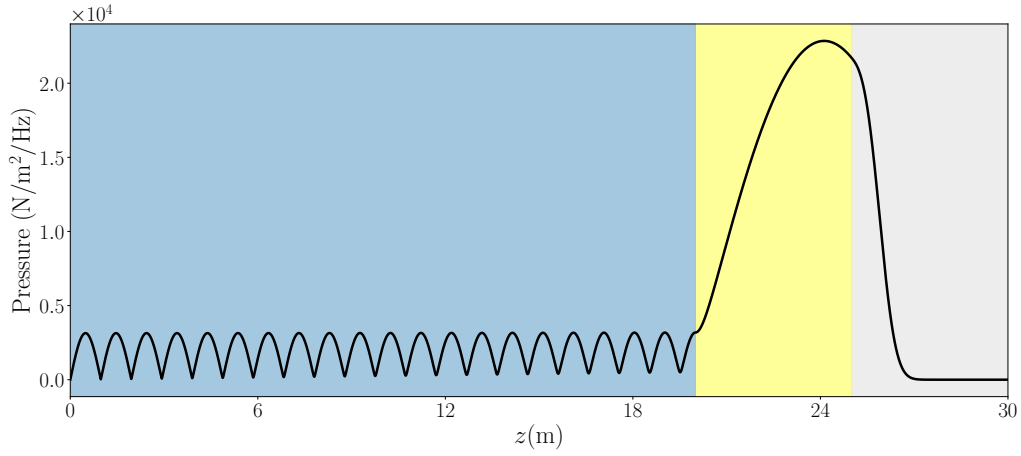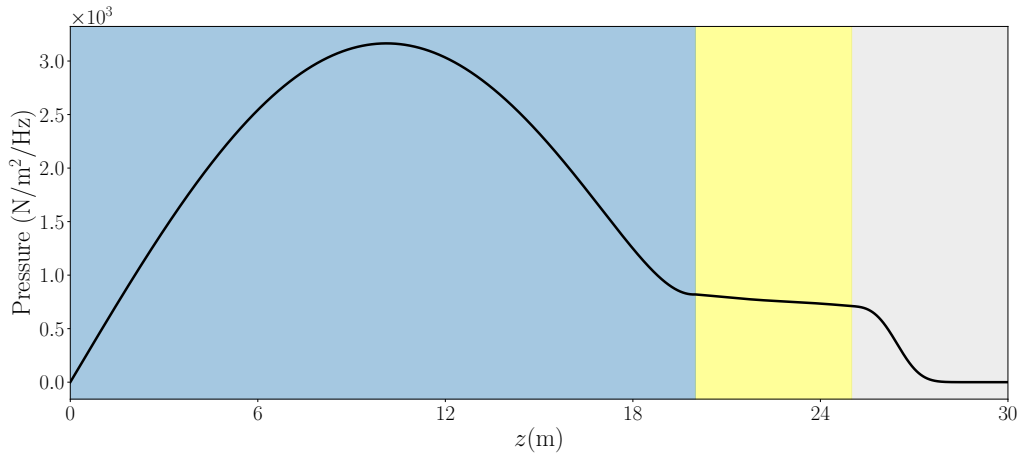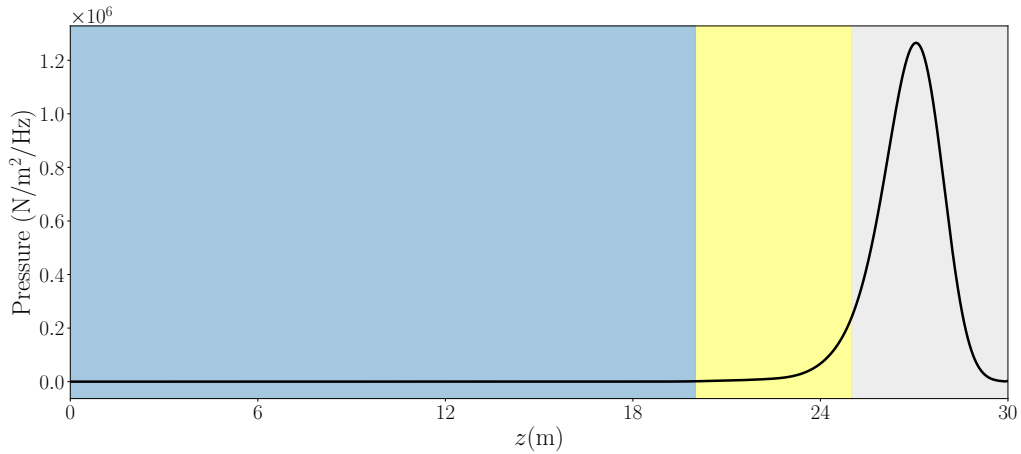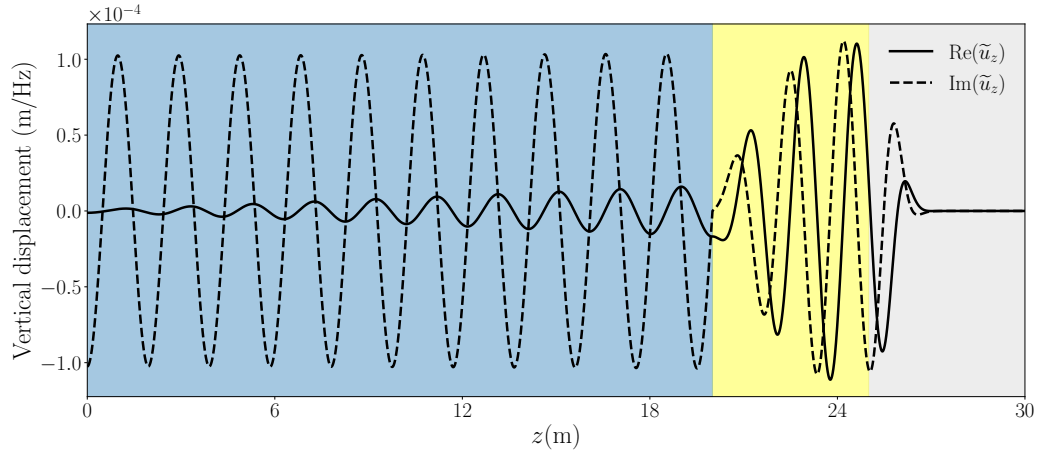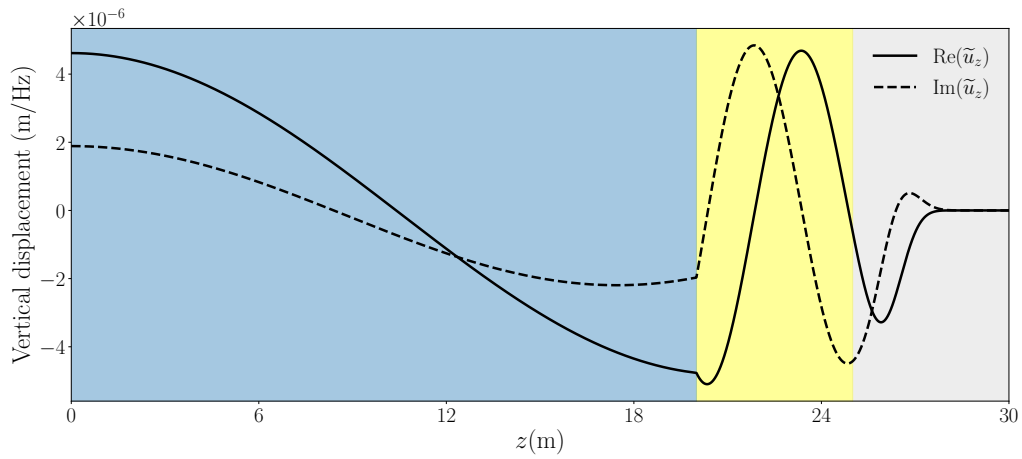
(a) $f = 50$ Hz, vertical pressure eigenfunction for wavenumber **1** as marked in Figure 6.4

(b) $f = 50$ Hz, vertical pressure eigenfunction for wavenumber **2** as marked in Figure 6.4

(c) $f = 50$ Hz, vertical pressure eigenfunction for wavenumber **3** as marked in Figure 6.4

Figure 6.6. Pressure field distributions for three types of modes at frequency $f = 50$ Hz. The computational domain consists of the acoustic region (blue), the elastic region (yellow), and the perfectly matched layer (PML) region (grey).
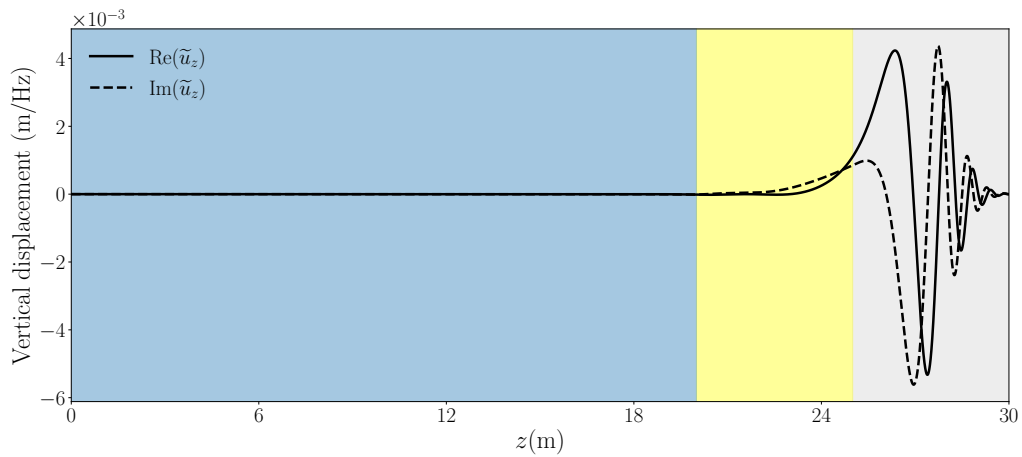
(a) $f = 50$ Hz, vertical displacement eigenfunction for wavenumber **2** as marked in Figure 6.4

(b) $f = 50$ Hz, vertical displacement eigenfunction for wavenumber **2** as marked in Figure 6.4

(c) $f = 50$ Hz, vertical displacement eigenfunction for wavenumber **2** as marked in Figure 6.4

Figure 6.7. Vertical displacement field distributions for three types of modes at frequency $f = 50$ Hz. The computational domain consists of the acoustic region (blue), the elastic region (yellow), and the perfectly matched layer (PML) region (grey).

6.2.4 Dispersion characteristics

Evanescent and propagating modes

The dispersion curves of the evanescent and propagating modes are shown in the figure below. The left panel shows the wavenumbers of the evanescent modes with $\text{Re}(k_r) \approx 0$. As can be observed from Figure 6.8, with increasing frequency, these modes are evanescent up to a certain frequency, which is called the cut-off frequency; after which they become propagating modes. Furthermore, the dispersion curves in the right figure of Figure 6.8 implies that the group velocities are smaller than the phase velocity; Furthermore, the increasing group velocity and decreasing phase velocity converge to c_f with increasing frequency ω, which obeys the feature of physical modes in Figure 2.8.
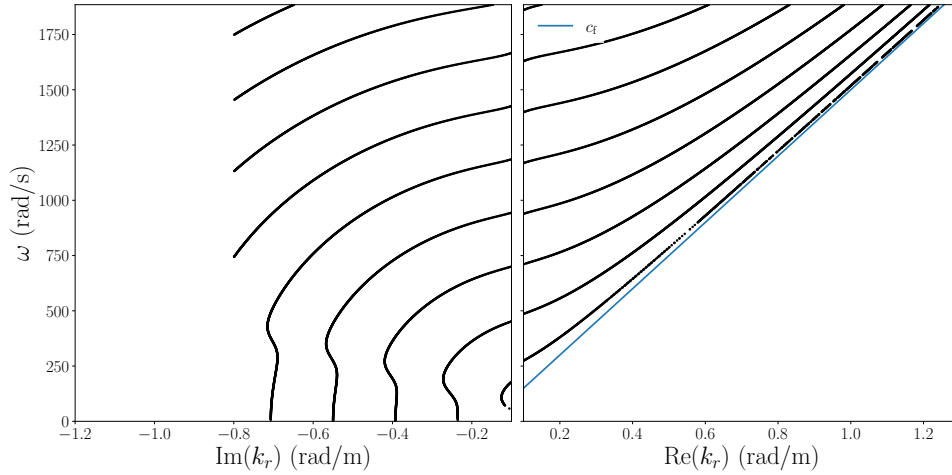

Figure 6.8. Dispersion curves of the acousto-elastic layer: the left and right columns represent purely imaginary-valued (evanescent modes) and purely real-valued wavenumbers (propagating modes), respectively.
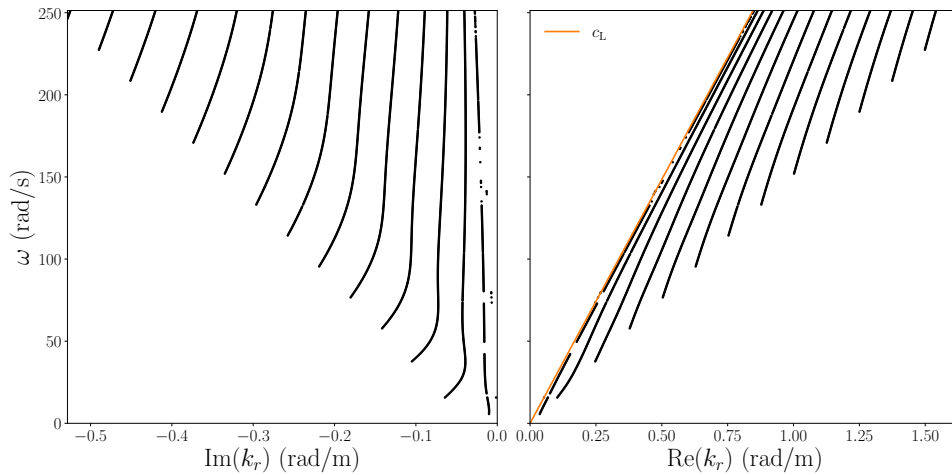
Bérenger modes

Figure 6.9. Dispersion curves of the acousto-elastic layer: the left and right columns represent imaginary and real parts of the complex-valued k_r for the first twelve Bérenger modes near k_L-branch, respectively.
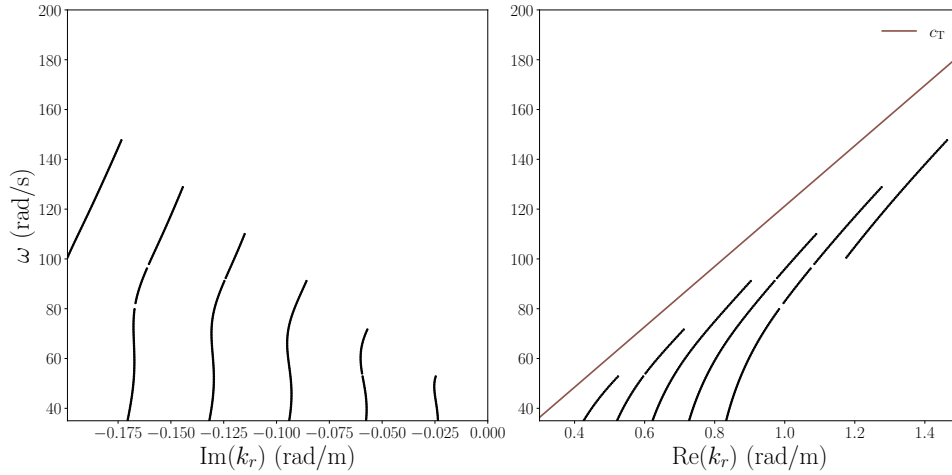
Figure 6.10. Dispersion curves of the acousto-elastic layer: the left and right columns represent imaginary and real parts of the complex-valued k_r for the first six Bérenger modes near k_T-branch, respectively.

The dispersion curves of the Bérenger modes are shown in Figure 6.9 and 6.10. Figure 6.9 shows the real and imaginary parts of the complex-valued k_r for the first thirteen modes (ranked by ascending $\mathrm{Re}(k_r)$) near the k_L branch; whereas 6.10 represent the first six modes near the k_T branch. They simultaneously imply anomalous dispersion characteristics as seen in the previous Chapter: the group velocities are larger than the phase velocity. This observation remarks the non-physical feature of Bérenger modes, which are introduced into the modal basis via the PML formulation.

6.3 Summary

This chapter provides the modal solution of the acousto-elastic domain with one PML. The main findings are summarized as follows:

1. The eigenvalue spectrum obtained from the dispersion relation $\det \mathbf{M} = 0$ reveals three distinct categories of modes:

   (a) *Evanescent modes*: Eigenvalues located near the imaginary axis with large imaginary parts and nearly zero real parts, corresponding to modes that decay exponentially in the radial direction.

   (b) *Propagating modes*: Eigenvalues positioned near the real axis, representing physically meaningful propagating waves in the waveguide.

   (c) *Bérenger modes*: Eigenvalues distributed along hyperbolic curves in the complex plane, arising from the PML implementation and representing non-physical artificial modes.

2. The modal shapes exhibit distinct behaviors across different domains:

   (a) *Evanescent modes*: Exhibit harmonic amplitudes in the acoustic domain, sharp exponential growth in the elastic domain due to complex vertical wavenumbers γ_L and γ_T, and appropriate attenuation in the PML domain.

   (b) *Propagating modes*: Maintain harmonic behavior throughout all domains with small real vertical wavenumbers, leading to non-leaky characteristics and effective attenuation within the PML region.

   (c) *Bérenger modes*: Display non-physical behavior, with negligible energy in the physical domains but concentrated energy within the PML region.

3. The dispersion analysis reveals two distinct types of behavior for the propagating modes:

   (a) *Physical dispersion*: Branches of the dispersion curves with small values of $\text{Re}(k_r)$ exhibit normal dispersive behavior, where group velocities are smaller than phase velocities, and both group and phase velocities converge to c_f at high frequencies.

   (b) *Anomalous dispersion*: Branches of the dispersion curves in which group velocities exceed phase velocities, representing non-physical dispersion characteristics.

4. From a numerical perspective, the normalized modes of the acousto-elastic waveguide system were found to be orthogonal by evaluating the right-hand side of Equation (6.33). The normalized eigenvectors satisfy $|\Gamma_{pp}| = 1$, and excellent cross-orthogonality ($\Gamma_{pq} = 0$ for $p \neq q$) is observed. Nevertheless, the following remarks should be noted:

   (a) *Modal orthogonality is preserved when sufficiently small integration steps $\mathrm{d}z$ are employed.* For higher-order modes, even smaller $\mathrm{d}z$ values are recommended to ensure accurate verification of cross-orthogonality.

   (b) *Although the orthogonality of modes has been derived for both elastic and acoustic layers, a rigorous mathematical proof for the elastic layer with PML is not yet available.* The present numerical results are obtained under the assumption that orthogonality remains valid in this case, thereby allowing the use of the superposition principle to sum the contributions of different layers.

   (c) In this chapter, a PML polynomial order of $m_{\text{PML}} = 2$ was considered. *However, the influence of m_{PML} on orthogonality has not been examined for the (acousto-)elastic layer with PML. A systematic parametric study on the role of m_{PML} is therefore recommended for future research on the (acousto-)elastic layer with PML.*

7

Conclusions and Recommendations

This thesis investigates computational methods for the acousto-elastic domain with perfectly matched layers (PMLs), focusing on the differences between the thin-layer method (TLM) and the semi-analytical method. It begins with a comparative study of the modal solutions for a single elastic layer. This is followed by an in-depth analysis of the modal solutions for an acoustic layer using the semi-analytical approach. Chapter 4 presents a comparative study of the modes of an elastic layer with PMLs using both the semi-analytical method and TLM. Finally, Chapter 5 provides the semi-analytical solution for an acousto-elastic layer with one PML. This chapter summarizes the main conclusions, addressing all research questions, and offers recommendations for future work.

7.1 Conclusions

As mentioned in Chapter 1, the first research objective is the investigation of the differences between the modal solutions of the single elastic layer, which provides a solution to the first supplementary research question:

In the case of a linear isotropic elastic layer, how do the eigenvalues and eigenmodes calculated by the semi-analytical method differ from those obtained using the thin-layer approach? What causes these differences?

From all observations in Chapter 3, it is concluded that the continuous (semi-analytical) and discrete (TLM) modal solutions show consistency for a single elastic domain with PML.

The second research objective focuses on studying modal solutions of an acoustic waveguide with PML using the semi-analytical solution, which have been completed in Chapter 4. The key finding of this chapter focus on the influence of the polynomial order m_{PML} of attenuation function on the modal solutions, which provides the solution the second supplementary research question:

For a fluid layer with a PML, how does the introduction of the PML affect the modal solutions of semi-analytical solutions? In what ways do different PML polynomial orders m_{PML} influence the solutions of eigenvalue problems, namely, eigenvalues, eigenvectors, and orthogonality?

From all observations in Chapter 4, the following conclusions of this research question are given:

1. The PML influences the semi-analytical solutions by introducing Berenger modes.

2. For the single acoustic layer with one PML, the imaginary part of the complex-stretch coordinate $\mathrm{Im}(\bar{z})$ is normalized with respect to m_{PML}. Under this condition, the eigenvalues are not affected by m_{PML} since the dispersion relation is independent of it.

3. The parameter m_{PML} affects the orthogonality of modes. Canceling certain boundary terms in the orthogonality derivation requires continuity of the modal slope at $z = Z_1$. When $m_{\mathrm{PML}} = 0$, the slope becomes discontinuous, leading to residual boundary terms that violate the standard orthogonality assumptions. Numerical results indicate that using $m_{\mathrm{PML}} > 0$ ensures acceptable orthogonality and preserves the theoretical foundation of PML-coupled systems.

The third objective of this thesis is to investigate the differences between the continuous and discrete modal solutions for an elastic layer with an adjacent PML. This objective is addressed in Chapter 5. In this chapter, the discrete and continuous modal solutions of the system shown in Figure 5.1 are compared, following the methodology established in the previous chapters. The conclusions drawn from these observations provide answers to the following research question:

For a linear elastic isotropic layer with one PML, how do the eigenvalues and eigenmodes calculated by the semi-analytical method differ from those obtained using the thin-layer approach? What causes these differences?

The study in Chapter 5 provides the solution to this research question. First, the main differences between two types of modal solutions of an elastic layer with one PML are given as follow

1. *Eigenvalue Distribution:* The semi-analytical solution produces eigenvalues distributed along a hyperbolic line in the complex k_r plane, corresponding to Bérenger modes. In contrast, the TLM approach yields predominantly evanescent modes with significant imaginary components contributing to discrete modal solution convergence.

2. *Modes:* The modes of the semi-analytical and the TLM solution for a single elastic layer with one PML differ, owing to the differences in their eigenvalues. In the thin-layer method, the modal basis mainly consists of evanescent modes with only a few Bérenger modes, while in the semi-analytical solution all modes belong to the Bérenger type.

3. *Orthogonality:* The criteria required to achieve improved orthogonality differ between the two methods. For the semi-analytical solution, enhanced orthogonality can be achieved through a finer discretization of the trapezoidal integration scheme. By contrast, in the thin-layer method, increasing the number of thin layers beyond an appropriate level results in a marked loss of orthogonality.

The differences arise from *the distinct eigenvalue problem formulations*. The thin-layer method produces a discrete eigenvalue problem, yielding a finite number of modes determined by the number of layers, whereas the dispersion relation admits an infinite set of eigenvalues and modes. In the semi-analytical solution, only Berenger modes occur, clustering near a hyperbola in the complex plane. In contrast, the TLM yields two eigenvalue sets—one near the imaginary axis and another near the hyperbola. Increasing the number of layers in the TLM introduces more modes along the hyperbolic locus, bringing the modal distribution closer to the infinite basis of the continuous solution.

In summary, these conclusions provide the answer to the following main research question:

How and why do the modal characteristics of the acoustic or elastic domains with PMLs differ between the semi-analytical solution and the thin-layer method?

Consistent with the answer to research question 3, the differences primarily arise from the eigenvalue distribution, modal characteristics, and cross-orthogonality, which are ultimately caused by the distinction between discrete and continuous eigenvalue problems.

7.2 Recommendations

Based on the conclusions of this thesis, the following recommendations are proposed for extending the fundamental research on computational methods for modes of the acousto-elastic system with PMLs by the author.

1. While the modal solution of a single elastic layer with one PML has been thoroughly studied via a semi-analytical method, a comparative analysis of the semi-analytical solution and TLM for a single acoustic layer or acousto-elastic with PML is recommended to better elucidate the differences between these two computational approaches.

2. In Chapter 3, the influence of the polynomial order m_{PML} on the modal solutions was examined. Based on the conclusions drawn from numerical results and mathematical derivations, it is recommended that $m_{\mathrm{PML}} > 0$ be used for the semi-analytical solution of a fluid layer incorporating PML. However, it remains unclear whether this conclusion can be extended to the remaining cases with PML; therefore, a study on the influence of m_{PML} is recommended for the elastic layer or the acousto-elastic layer with PML in future research, via mathematical derivations and numerical results.

3. Although the polynomial order m_{PML} has been examined in this research, the influence of other PML parameters, namely the attenuation coefficient β_{s} and the height of the PML layer H_{PML}, should also be investigated owing to their impact on the modal solutions. Therefore, a detailed parametric study on these remaining parameters is recommended for future research.

4. As shown in Figure 2.3 in Chapter 2, real ocean environments include bottom layers with discontinuous properties in the vertical direction, representing the interfaces between geological strata. Therefore, the model with a single elastic layer with PML can be extended to the case of *multiple elastic layers* with one PML in future research.

5. In the semi-analytical solutions, the calculations of $|\Gamma_{pq}|$ were performed using the trapezoidal integration scheme, which requires many integration points for higher-order Berenger modes due to their similarity. Among the results of the acoustic layer with PML, the trapezoidal integration scheme does not work well for $m_{\mathrm{PML}} > 1$. It is possible that a more advanced quadrature scheme may be required for this case. Therefore, future research is recommended to explore alternative integration schemes.

6. The cross-orthogonality of the modes that are computed from the thin-layer method is violated when too many thin layers are used. The reasons for this finding is still not unclear. A physical or numerical reasons behind this finding can be investigated furtherly in the future research.

In addition to the development of fundamental research, the following suggestions are provided regarding the practical applications of the two computational methods for the acousto-elastic domain with PML:

1. When the semi-analytical method is used with a polynomial attenuation function in the PML, a positive value of m_{PML} is recommended to maintain the continuity of the eigenvector at the interface between the physical and PML domains, as well as to improve the cross-orthogonality of the modes.

2. Due to the violated cross-orthogonality, it is not suggested to use too many layers in the PML when the Thin-layer method is adopted.

Bibliography

[1] J. D. Achenbach. *Wave Propagation in Elastic Solids*, volume 16 of *Applied Mathematics and Mechanics*. Elsevier, Amsterdam, 1973. First edition: 1973, First paperback edition: 1975, Reprinted multiple times.

[2] K. Aki and P. G. Richards. *Quantitative Seismology: Theory and Methods*. Freeman, New York, 1980.

[3] A. A. Bakr. *The Boundary Integral Equation Method in Axisymmetric Stress Analysis Problems*, volume 14 of *Lecture Notes in Engineering*. Springer-Verlag, Berlin, Heidelberg, New York, Tokyo, 1985.

[4] João Manuel de Oliveira Barbosa, Joonsang Park, and Eduardo Kausel. Perfectly matched layers in the thin layer method. *Computer Methods in Applied Mechanics and Engineering*, 217–220:262–274, 2012.

[5] J.-P. Berenger. A perfectly matched layer for the absorption of electromagnetic waves. *Journal of Computational Physics*, 114(2):185–200, 1994.

[6] M. G. Bostock. On the orthogonality of surface wave eigenfunctions in cylindrical coordinates. *Geophysical Journal International*, 103:763–767, 1990.

[7] W. M. Ewing, W. S. Jardetzky, and F. Press. *Elastic Waves in Layered Media*. McGraw-Hill, New York, 1957. Lamont Geological Observatory Contribution.

[8] M. Gallezot, F. Treyssède, and L. Laguerre. A modal approach based on perfectly matched layers for the forced response of elastic open waveguides. *Journal of Computational Physics*, 356:391–409, 03 2018.

[9] M. Gallezot, F. Treyssède, and L. Laguerre. Contribution of leaky modes in the modal analysis of unbounded problems with perfectly matched layers. *The Journal of the Acoustical Society of America*, 141(1):EL16–EL21, 2017.

[10] Fang Q. Hu. On absorbing boundary conditions for linearized euler equations by a perfectly matched layer. *Journal of Computational Physics*, 129(1):201–219, 1996.

[11] Finn B. Jensen, William A. Kuperman, Michael B. Porter, and Henrik Schmidt. *Computational Ocean Acoustics*. Modern Acoustics and Signal Processing. Springer New York, New York, NY, 2011.

[12] Eduardo Kausel. An explicit solution for the green functions for dynamic loads in layered media. Technical Report R81-13, Massachusetts Institute of Technology (MIT), May 1981. Research Report R81-13, Order No. 699.

[13] S. Kucukcoban and L. F. Kallivokas. Mixed perfectly-matched-layers for direct transient analysis in 2d elastic heterogeneous media. *Computer Methods in Applied Mechanics and Engineering*, 200(1–4):57–76, January 2011.

[14] J. Miklowitz. *The Theory of Elastic Waves and Waveguides*. North-Holland Publishing Company, Amsterdam, 1978.

[15] Joonsang Park. *Wave motion in finite and infinite media using the Thin-Layer Method*. Doctor of science in structures and materials, Massachusetts Institute of Technology (MIT), February 2002. Advisor: Eduardo Kausel.

[16] Yaxi Peng, Apostolos Tsouvalas, Tasos Stampoultzoglou, and Andrei Metrikine. A fast computational model for near- and far-field noise prediction due to offshore pile driving. *Journal of the Acoustical Society of America*, 149(3):1772–1790, 2021.

[17] H. Rogier and D. De Zutter. Berenger and leaky modes in optical fibers terminated with a perfectly matched layer. *Journal of Lightwave Technology*, 20(7):1141–1148, July 2002.

[18] A. Taflove and S. C. Hagness. *Computational Electrodynamics: The Finite-Difference Time-Domain Method*. Artech, Norwood, MA, 2000.

[19] A. TSETAS. *A unified modelling framework for vibratory pile driving methods*. PhD thesis, Delft University of Technology, 2023.

[20] A. Tsouvalas, H. Hendrikse, and A. V. Metrikine. The completeness of the set of modes for various waveguides and its significance for the near-field interaction with vibrating structures. In A. Cunha, E. Caetano, P. Ribeiro, and G. Müller, editors, *Proceedings of the 9th International Conference on Structural Dynamics, EURODYN 2014*, pages Porto, Portugal, 30 June – 2 July 2014. Department of Civil Engineering, Faculty of Engineering and Geosciences, Delft University of Technology, The Netherlands, 2014.

[21] Apostolos Tsouvalas. *Underwater Noise Generated by Offshore Pile Driving*. PhD thesis, Delft University of Technology, Delft, The Netherlands, 2015.

[22] Apostolos Tsouvalas and Andrei V. Metrikine. A semi-analytical model for the prediction of underwater noise from offshore pile driving. *Journal of Sound and Vibration*, 332(13):3232–3257, 2013.

[23] Apostolos Tsouvalas and Andrei V. Metrikine. A three-dimensional vibroacoustic model for the prediction of underwater noise from offshore pile driving. *Journal of Sound and Vibration*, 333(8):2283–2311, 2014.

[24] Apostolos Tsouvalas and Andrei V. Metrikine. Structure-borne wave radiation by impact and vibratory piling in offshore installations: From sound prediction to auditory damage. *Journal of Marine Science and Engineering*, 4(3):44, 2016.

[25] Semyon V. Tsynkov. Numerical solution of problems on unbounded domains. a review. *Applied Numerical Mathematics*, 27(4):465–532, August 1998.

[26] J. Zhu and Y. Zhang. Cross orthogonality between eigenfunctions and conjugate eigenfunctions of a class of modified helmholtz operator for pekeris waveguide. *Journal of Theoretical and Computational Acoustics*, 2018.

A

Semi-analytical Matrices of coefficients

This Appendix provides all matrices of the systems used in the semi-analytical solutions of

1. A single elastic layer

2. An acoustic domain with PML

3. An elastic domain with PML

4. An acousto-elastic domain with PML

A.1 Elastic layer

For a single elastic layer, the structure of the system matrix $\mathbf{M}$ is given as below:

$$\mathbf{M} = \begin{bmatrix} i\left(2\mu_s\gamma_L^2 + \lambda_s k_L^2\right)e^{i\gamma_L Z_1} & i\left(2\mu_s\gamma_L^2 + \lambda_s k_L^2\right) & -2\mu_s k_r\gamma_T e^{i\gamma_T Z_1} & 2\mu_s k_r\gamma_L \\ 2\mu_s k_r\gamma_L e^{i\gamma_L Z_1} & -2\mu_s k_r\gamma_L & -i\mu_s\left(\gamma_T^2 - k_r^2\right)e^{i\gamma_T Z_1} & -i\mu_s\left(\gamma_T^2 - k_r^2\right) \\ -\gamma_L & \gamma_L e^{i\gamma_L Z_1} & -ik_r & -ik_r e^{i\gamma_T Z_1} \\ ik_r & ik_r e^{i\gamma_T Z_1} & \gamma_T & -\gamma_T e^{i\gamma_T Z_1} \end{bmatrix}. \tag{A.1}$$

A.2 Acoustic domain with PML

For an acoustic domain with PML, the structure of the system matrix $\mathbf{M}$ is given as below: The structure of matrices are given as:

$$\mathbf{M} = \begin{bmatrix} i & e^{-i\gamma_f Z_1} & 0 & 0 \\ -ie^{-i\gamma_f Z_1} & i & i & -ie^{-\gamma_f H_{PML}(i+\beta_0)} \\ e^{-i\gamma_f Z_1} & 1 & -1 & -e^{-\gamma_f H_{PML}(i+\beta_0)} \\ 0 & 0 & -i\gamma_f e^{-\gamma_f H_{PML}(i+\beta_0)} & i\gamma_f \end{bmatrix} \tag{A.2}$$

A.3 An Elastic Domain with PML

$$
\mathbf{M} = \begin{bmatrix}
-\left(k_L^2\lambda_s + 2\mu_s\gamma_L^2\right)e^{-i\gamma_L Z_1} & -\left(\lambda_s + 2\mu_s\right)\gamma_L^2 - k_r^2\lambda_s & 2ik_r k_T\mu_s e^{-i\gamma_T Z_1} & -2ik_T k_r\mu_s & 0 & 0 & 0 & 0 \\[2ex]
-2ik_L k_r\mu_s e^{-ik_L Z_1} & 2ik_L k_r\mu_s & \left(k_T^2 - k_r^2\right)\mu_s e^{-ik_T Z_1} & \left(k_T^2 - k_r^2\right)\mu_s & 0 & 0 & 0 & 0 \\[2ex]
-ik_L & ik_L e^{-ik_L Z_1} & -k_r & -k_r e^{-ik_T Z_1} & ik_L e^{-H_{PML}(\beta_0+i)} & -ik_L & k_r e^{-H_{PML}(\beta_0+i)} & k_r \\[2ex]
-k_r & -k_r e^{-ik_L Z_1} & -ik_T & ik_T e^{-ik_T Z_1} & k_r e^{-H_{PML}(\beta_0+i)} & k_r & ik_T e^{-H_{PML}(\beta_0+i)} & -ik_T \\[2ex]
\left(k_L^2 + k_r^2\right)\lambda_s + 2\mu_s k_L^2 & \left[\left(k_L^2 + k_r^2\right)\lambda_s + 2\mu_s k_L^2\right]e^{-ik_L Z_1} & -2ik_T k_r\mu_s & 2ik_r k_T\mu_s e^{-ik_T Z_1} & -\left(k_L^2 + k_r^2\right)\lambda_s - 2\mu_s k_L^2 & -\lambda_s k_L^2 - 2\mu_s k_L^2 - k_r^2\lambda_s & 2ik_T k_r\mu_s e^{-H_{PML}(\beta_0+i)} & -2ik_T k_r\mu_s \\[2ex]
2ik_L k_r\mu_s & -2ik_L k_r\mu_s e^{-ik_L Z_1} & -\mu_s k_T^2 + k_r^2\mu_s & \left(-k_T^2 + k_r^2\right)\mu_s e^{-ik_T Z_1} & -2ik_L k_r\mu_s e^{-H_{PML}(\beta_0+i)} & 2ik_L k_r\mu_s & \left(k_T^2 - k_r^2\right)\mu_s e^{-H_{PML}(\beta_0+i)} & \left(k_T^2 - k_r^2\right)\mu_s \\[2ex]
0 & 0 & 0 & 0 & ik_L & -ik_L e^{-H_{PML}(\beta_0+i)} & k_r & k_r e^{-H_{PML}(\beta_0+i)} \\[2ex]
0 & 0 & 0 & 0 & -k_r & -k_r e^{-H_{PML}(\beta_0+i)} & -ik_T & ik_T e^{-H_{PML}(\beta_0+i)}
\end{bmatrix}
$$

A.4 An acousto-Elastic Domain with PML

$$
\mathbf{M} = \begin{bmatrix}
-\mathrm{i}\omega\rho_{\mathrm{f}} & 0 & 0 & 0 & 0 & -\mathrm{i}\omega\rho_{\mathrm{f}}\mathrm{e}^{\mathrm{i}k_z z_0} & 0 & 0 & 0 & 0 \\[2ex]
0 & -2\mathrm{i}k_{\mathrm{L}}k_r\mu_{\mathrm{s}}\mathrm{e}^{\mathrm{i}k_{\mathrm{L}}(z_0-Z_1)} & \left(k_{\mathrm{T}}^2-k_r^2\right)\mu_{\mathrm{s}}\mathrm{e}^{\mathrm{i}k_{\mathrm{T}}(z_0-Z_1)} & 0 & 0 & 0 & 2\mathrm{i}k_{\mathrm{L}}k_r\mu_{\mathrm{s}} & \left(k_{\mathrm{T}}^2-k_r^2\right)\mu_{\mathrm{s}} & 0 & 0 \\[2ex]
\frac{k_z\mathrm{e}^{\mathrm{i}k_z z_0}}{\omega} & -\mathrm{i}k_{\mathrm{L}}\mathrm{e}^{\mathrm{i}k_{\mathrm{L}}(z_0-Z_1)} & -k_r\mathrm{e}^{\mathrm{i}k_{\mathrm{T}}(z_0-Z_1)} & 0 & 0 & -\frac{k_z}{\omega} & \mathrm{i}k_{\mathrm{L}} & -k_r & 0 & 0 \\[2ex]
-\mathrm{i}\omega\rho_{\mathrm{f}}\mathrm{e}^{\mathrm{i}k_z z_0} & -\left(k_{\mathrm{L}}^2+k_r^2\right)\lambda_{\mathrm{s}}-2\mu_{\mathrm{s}}k_{\mathrm{L}}^2 & 2\mathrm{i}k_{\mathrm{T}}k_r\mu_{\mathrm{s}}\mathrm{e}^{\mathrm{i}k_{\mathrm{T}}(z_0-Z_1)} & 0 & 0 & -\mathrm{i}\omega\rho_{\mathrm{f}} & -\left(2\mu_{\mathrm{s}}+\lambda_{\mathrm{s}}\right)k_{\mathrm{L}}^2-k_r^2\lambda_{\mathrm{s}} & -2\mathrm{i}k_{\mathrm{T}}k_r\mu_{\mathrm{s}} & 0 & 0 \\[2ex]
0 & \mathrm{i}k_{\mathrm{L}} & k_r & -\mathrm{i}k_{\mathrm{L}}\mathrm{e}^{-H_{\mathrm{PML}}(\beta_0+\mathrm{i})} & -k_r\mathrm{e}^{-H_{\mathrm{PML}}(\beta_0+\mathrm{i})} & 0 & -\mathrm{i}k_{\mathrm{L}}\mathrm{e}^{\mathrm{i}k_{\mathrm{L}}(z_0-Z_1)} & k_r\mathrm{e}^{\mathrm{i}k_{\mathrm{T}}(z_0-Z_1)} & \mathrm{i}k_{\mathrm{L}} & -k_r \\[2ex]
0 & -k_r & -\mathrm{i}k_{\mathrm{T}} & k_r\mathrm{e}^{-H_{\mathrm{PML}}(\beta_0+\mathrm{i})} & \mathrm{i}k_{\mathrm{T}}\mathrm{e}^{-H_{\mathrm{PML}}(\beta_0+\mathrm{i})} & 0 & -k_r\mathrm{e}^{\mathrm{i}k_{\mathrm{L}}(z_0-Z_1)} & \mathrm{i}k_{\mathrm{T}}\mathrm{e}^{\mathrm{i}k_{\mathrm{T}}(z_0-Z_1)} & k_r & -\mathrm{i}k_{\mathrm{T}} \\[2ex]
0 & -\left(2\mu_{\mathrm{s}}+\lambda_{\mathrm{s}}\right)k_{\mathrm{L}}^2-k_r^2\lambda_{\mathrm{s}} & 2\mathrm{i}k_{\mathrm{T}}k_r\mu_{\mathrm{s}} & \left(k_{\mathrm{L}}^2+k_r^2\right)\lambda_{\mathrm{s}}+2\mu_{\mathrm{s}}k_{\mathrm{L}}^2 & -2\mathrm{i}k_{\mathrm{T}}k_r\mu_{\mathrm{s}}\mathrm{e}^{-H_{\mathrm{PML}}(\beta_0+\mathrm{i})} & 0 & -\left(k_{\mathrm{L}}^2+k_r^2\right)\lambda_{\mathrm{s}}-2\mu_{\mathrm{s}}k_{\mathrm{L}}^2 & -2\mathrm{i}k_{\mathrm{T}}k_r\mu_{\mathrm{s}}\mathrm{e}^{\mathrm{i}k_{\mathrm{T}}(z_0-Z_1)} & \left(k_{\mathrm{L}}^2+k_r^2\right)\lambda_{\mathrm{s}}+2\mu_{\mathrm{s}}k_{\mathrm{L}}^2 & 2\mathrm{i}k_{\mathrm{T}}k_r\mu_{\mathrm{s}} \\[2ex]
0 & -2\mathrm{i}k_{\mathrm{L}}k_r\mu_{\mathrm{s}} & \left(k_{\mathrm{T}}^2-k_r^2\right)\mu_{\mathrm{s}} & 2\mathrm{i}k_{\mathrm{L}}k_r\mu_{\mathrm{s}}\mathrm{e}^{-H_{\mathrm{PML}}(\beta_0+\mathrm{i})} & \left(-k_{\mathrm{T}}^2+k_r^2\right)\mu_{\mathrm{s}}\mathrm{e}^{-H_{\mathrm{PML}}(\beta_0+\mathrm{i})} & 0 & 2\mathrm{i}k_{\mathrm{L}}k_r\mu_{\mathrm{s}}\mathrm{e}^{\mathrm{i}k_{\mathrm{L}}(z_0-Z_1)} & \left(k_{\mathrm{T}}^2-k_r^2\right)\mu_{\mathrm{s}}\mathrm{e}^{\mathrm{i}k_{\mathrm{T}}(z_0-Z_1)} & -2\mathrm{i}k_{\mathrm{L}}k_r\mu_{\mathrm{s}} & -\mu_{\mathrm{s}}k_{\mathrm{T}}^2+k_r^2\mu_{\mathrm{s}} \\[2ex]
0 & 0 & 0 & \mathrm{i}k_{\mathrm{L}} & k_r & 0 & 0 & 0 & -\mathrm{i}k_{\mathrm{L}}\mathrm{e}^{-H_{\mathrm{PML}}(\beta_0+\mathrm{i})} & k_r\mathrm{e}^{-H_{\mathrm{PML}}(\beta_0+\mathrm{i})} \\[2ex]
0 & 0 & 0 & -k_r & -\mathrm{i}k_{\mathrm{T}} & 0 & 0 & 0 & -k_r\mathrm{e}^{-H_{\mathrm{PML}}(\beta_0+\mathrm{i})} & \mathrm{i}k_{\mathrm{T}}\mathrm{e}^{-H_{\mathrm{PML}}(\beta_0+\mathrm{i})}
\end{bmatrix}
$$

Orthogonality between Eigenvectors and Conjugate Eigenvectors

B.1 Introduction

The cross orthogonality between the eigenvectors and their conjugates has been proved in [26] for a Pekeris waveguides with one PML. In this Appendix, we will give the same derivation for a single acoustic layer with PML, as shown in Figure 4.1.

B.2 The derivation of the conjugate eigenfunction

Assume operator $\mathscr{L}$ as:

$$\mathscr{L} = \frac{1}{\varepsilon(z)}\frac{\mathrm{d}}{\mathrm{d}z}\left[\frac{1}{\varepsilon(z)}\frac{\mathrm{d}}{\mathrm{d}z}\right] + k_{\mathrm{f}}^2 \tag{B.1}$$

where

$$\varepsilon(z) = \begin{cases} 1, & 0 \le z \le Z_1, \\ 1 - \mathrm{i}\beta(z)/\omega & Z_1 \le z \le Z_2. \end{cases} \tag{B.2}$$

Assume $\phi(z)$ and $\varphi(z)$ be the eigenvector and its corresponding conjugate eigenvector and they satisfy the boundary conditions discussed in the previous chapter.

We will start with the derivation of the following internal product:

$$\langle \mathscr{L}\phi, \varphi \rangle = \int_0^{Z_2} \overline{\varphi(z)} \cdot \mathscr{L}\phi(z)\,\mathrm{d}z \tag{B.3}$$

It could be expanded as:

$$\langle \mathscr{L}\phi, \varphi \rangle = \int_0^{Z_1} \overline{\varphi_1}\left[\frac{\mathrm{d}^2\phi_1}{\mathrm{d}z^2} + k_{\mathrm{f}}^2\phi_1\right]\mathrm{d}z + \int_{Z_1}^{Z_2} \overline{\varphi_2}\left[\frac{1}{\varepsilon(z)}\frac{\mathrm{d}}{\mathrm{d}z}\left(\frac{1}{\varepsilon(z)}\frac{\mathrm{d}\phi_2}{\mathrm{d}z}\right) + k_{\mathrm{f}}^2\phi_2\right]\mathrm{d}z$$

$$= \underbrace{\int_0^{Z_1} \overline{\varphi_1}\left[\frac{\mathrm{d}^2\phi_1}{\mathrm{d}z^2}\right]\mathrm{d}z}_{I_1} + \underbrace{\int_{Z_1}^{Z_2} \overline{\varphi_2}\left[\frac{1}{\varepsilon(z)}\frac{\mathrm{d}}{\mathrm{d}z}\left(\frac{1}{\varepsilon(z)}\frac{\mathrm{d}\phi_2}{\mathrm{d}z}\right)\right]\mathrm{d}z}_{I_2} + \underbrace{\int_0^{Z_1} \overline{\varphi_1}k_{\mathrm{f}}^2\phi_1\,\mathrm{d}z}_{I_3} + \underbrace{\int_{Z_1}^{Z_2} \overline{\varphi_2}k_{\mathrm{f}}^2\phi_2\,\mathrm{d}z}_{I_4} \tag{B.4}$$

Apply integration by parts to I_1 and I_2:

$$I_1 = \overline{\varphi_1}\left(\frac{\mathrm{d}\phi_1}{\mathrm{d}z}\right)\Big|_0^{Z_1} - \int_0^{Z_1}\frac{\mathrm{d}\phi_1}{\mathrm{d}z}\cdot\frac{\mathrm{d}\overline{\varphi_1}}{\mathrm{d}z}\,\mathrm{d}z \tag{B.5}$$

$$I_2 = \frac{\overline{\varphi_2}}{\varepsilon^2(z)}\left(\frac{\mathrm{d}\phi_2}{\mathrm{d}z}\right)\Big|_{Z_1}^{Z_2} - \int_{Z_1}^{Z_2}\frac{1}{\varepsilon(z)}\frac{\mathrm{d}\phi_2}{\mathrm{d}z}\cdot\frac{\mathrm{d}}{\mathrm{d}z}\left[\frac{\overline{\varphi_2}}{\varepsilon(z)}\right]\mathrm{d}z \tag{B.6}$$

Applying integration by parts again gives:

$$I_1 = \overline{\varphi_1}\phi_1'\Big|_0^{Z_1} - \phi_1\overline{\varphi_1'}\Big|_0^{Z_1} + \int_0^{Z_1} \phi_1 \frac{\mathrm{d}^2\overline{\varphi_1}}{\mathrm{d}z^2}\,\mathrm{d}z \tag{B.7}$$

$$I_2 = \frac{\overline{\varphi_2}\phi_2'}{\varepsilon^2(z)}\Big|_{Z_1}^{Z_2} - \frac{\phi_2}{\varepsilon(z)}\left[\frac{\overline{\varphi_2}}{\varepsilon(z)}\right]'\Big|_{Z_1}^{Z_2} + \int_{Z_1}^{Z_2} \phi_2 \cdot \frac{\mathrm{d}}{\mathrm{d}z}\left[\frac{1}{\varepsilon(z)}\frac{\mathrm{d}}{\mathrm{d}z}\left(\frac{\overline{\varphi_2}}{\varepsilon(z)}\right)\right]\mathrm{d}z \tag{B.8}$$

As a result, we have

$$\langle \mathscr{L}\phi, \varphi\rangle = I_1 + I_3 + I_2 + I_4$$
$$= \int_0^{Z_1} \phi_1\left[\frac{\mathrm{d}^2}{\mathrm{d}z^2} + k_{\mathrm{f}}^2\right]\overline{\varphi_1}\,\mathrm{d}z + \int_{Z_1}^{Z_2} \phi_2\left[\frac{\mathrm{d}}{\mathrm{d}z}\left(\frac{1}{\varepsilon(z)}\frac{\mathrm{d}}{\mathrm{d}z}\left(\frac{\overline{\varphi_2}}{\varepsilon(z)}\right)\right) + \gamma_{\mathrm{f}}^2\overline{\varphi_2}\right]\mathrm{d}z \tag{B.9}$$
$$+ \text{Boundary Terms}$$

The boundary terms are witten as

$$\overline{\varphi_1(Z_1)}\phi_1'(Z_1) - \overline{\varphi_1(0)}\phi_1'(0) - \phi_1(Z_1)\overline{\varphi_1'(Z_1)} + \phi_1(0)\overline{\varphi_1'(0)} + \overline{\varphi_2(Z_2)}\phi_2'(Z_2)/\varepsilon^2(Z_2)$$
$$- \overline{\varphi_2(Z_1)}\phi_2'(Z_1)/\varepsilon^2(Z_1) - \phi_2(Z_2)/\varepsilon(Z_2)\left(\overline{\varphi_2}/\varepsilon\right)'\Big|_{z=Z_2} + \phi_2(Z_1)/\varepsilon(Z_1)\left(\overline{\varphi_2}/\varepsilon\right)'\Big|_{z=Z_1} \tag{B.10}$$

Applying boundary conditions of both eigenvectors and conjugate eigenvectors:

$$\phi_1(0) = 0 \qquad\qquad \phi_2'(Z_2) = 0 \tag{B.11}$$

$$\overline{\varphi_1(0)} = 0 \qquad\qquad \left(\overline{\varphi_2}/\varepsilon\right)'\Big|_{z=Z_2} = 0 \tag{B.12}$$

Equation (B.10) are furtherly reduced to:

$$\overline{\varphi_1(Z_1)}\phi_1'(Z_1) - \overline{\varphi_2(Z_1)}\phi_2'(Z_1) + \phi_2(Z_1)\left(\overline{\varphi_2}/\varepsilon\right)'\Big|_{z=Z_1} - \phi_1(Z_1)\left(\overline{\varphi_1}/\varepsilon\right)'\Big|_{z=Z_1} \tag{B.13}$$

Due to the continuity of eigenvectors at $z = Z_1$, we have

$$\overline{\varphi_1(Z_1)} = \overline{\varphi_2(Z_1)} \tag{B.14}$$

Therefore, the boundary terms can be furtherly reduced into

$$\overline{\varphi_1(Z_1)}\left[\phi_1'(Z_1) - \phi_2'(Z_1)/\varepsilon^2(Z_1)\right] + \phi_2(Z_1)/\varepsilon(Z_1)\left[\left(\overline{\varphi_1}\right)'\Big|_{z=Z_1} - \left(\overline{\varphi_2}/\varepsilon\right)'\Big|_{z=Z_1}\right] \tag{B.15}$$

When $\varepsilon(z)$ is continuous at $z = Z_1$:

$$\varepsilon(Z_1) = 1 \tag{B.16}$$

As a result, (B.15) are reduced to:

$$\overline{\varphi_1(Z_1)}\left[\phi_1'(Z_1) - \phi_2'(Z_1)\right] + \phi_2(Z_1)\left[\left(\overline{\varphi_1}/\varepsilon\right)'\Big|_{z=Z_1} - \left(\overline{\varphi_2}/\varepsilon\right)'\Big|_{z=Z_1}\right] \tag{B.17}$$

The second term here can be expanded as:

$$\phi_2(Z_1)\left[\left(\overline{\varphi_1}'/\varepsilon\right)\Big|_{z=Z_1} - \left(\overline{\varphi_2}'/\varepsilon\right)\Big|_{z=Z_1} + \left(\overline{\varphi_2}\varepsilon'/\varepsilon^2\right)\Big|_{z=Z_1} - \left(\overline{\varphi_1}\varepsilon'/\varepsilon^2\right)\Big|_{z=Z_1}\right] \tag{B.18}$$

When $\phi'(z)$, $\overline{\varphi(z)}$, ε and ε' are continuous at $z = Z_1$, the boundary terms can be canceled out. We can have the following definition:

$$\langle \mathcal{L}\phi, \varphi \rangle = \int_0^{Z_2} \phi(z) \cdot \left[\frac{\mathrm{d}}{\mathrm{d}z}\left(\frac{1}{\varepsilon(z)} \frac{\mathrm{d}}{\mathrm{d}z}\left(\frac{\overline{\varphi}}{\varepsilon(z)} \right) \right) + \gamma_{\mathrm{f}}^2 \overline{\varphi} \right] \mathrm{d}z \triangleq \int_0^{Z_2} \phi \overline{\mathcal{M}\varphi} \, \mathrm{d}z = \langle \phi, \mathcal{M}\varphi \rangle \tag{B.19}$$

The $\overline{\varphi_i(z)}$ satisfies the following equations of motions:

$$\frac{\mathrm{d}^2 \overline{\varphi_1}}{\mathrm{d}z^2} + \left(k_{\mathrm{f}}^2 - k_r^2 \right)\overline{\varphi_1} = 0 \qquad\qquad 0 < z < Z_1 \tag{B.20}$$

$$\frac{\mathrm{d}}{\mathrm{d}z}\left(\frac{1}{\varepsilon(z)} \frac{\mathrm{d}}{\mathrm{d}z}\left(\frac{\overline{\varphi_2}}{\varepsilon(z)} \right) \right) + \left(k_{\mathrm{f}}^2 - k_r^2 \right)\overline{\varphi_2} = 0 \qquad\qquad Z_1 < z < Z_2 \tag{B.21}$$

The second EoM here can be written in an alternative form:

$$\frac{1}{\varepsilon(z)}\frac{\mathrm{d}}{\mathrm{d}z}\left(\frac{1}{\varepsilon(z)} \frac{\mathrm{d}}{\mathrm{d}z}\left(\frac{\overline{\varphi_2}}{\varepsilon(z)} \right) \right) + \left(k_{\mathrm{f}}^2 - k_r^2 \right)\frac{\overline{\varphi_2}}{\varepsilon(z)} = 0 \qquad\qquad Z_1 < z < Z_2 \tag{B.22}$$

Let $\psi_2(z) = \overline{\varphi_2}/\varepsilon(z)$, we could have

$$\frac{1}{\varepsilon(z)}\frac{\mathrm{d}}{\mathrm{d}z}\left(\frac{1}{\varepsilon(z)} \frac{\mathrm{d}\psi_2}{\mathrm{d}z} \right) + \left(k_{\mathrm{f}}^2 - k_r^2 \right)\psi_2 = 0 \qquad\qquad Z_1 < z < Z_2 \tag{B.23}$$

Besides, ψ is assumed to satisfy the following boundary conditions on the basis of Equation (B.12):

$$\psi_1(0) = 0 \qquad\qquad\qquad \psi_2'\Big|_{z=Z_2} = 0 \tag{B.24}$$

The general solutions of $\overline{\varphi_i(z)}$ are given as:

$$\overline{\varphi_1(z)} = A_1 \exp\left[\mathrm{i}\gamma_{\mathrm{f}}(z - Z_1) \right] + A_2 \exp(-\mathrm{i}\gamma_{\mathrm{f}}z) \qquad\qquad 0 \leq z \leq Z_1 \tag{B.25}$$

$$\overline{\varphi_2(z)} = \left[A_3 \exp\left[\mathrm{i}\gamma_{\mathrm{f}}(\bar{z} - \bar{Z}_2) \right] + A_4 \exp\left[-\mathrm{i}\gamma_{\mathrm{f}}(\bar{z} - \bar{Z}_1) \right] \right]\varepsilon(z) \qquad Z_1 \leq z \leq Z_2 \tag{B.26}$$

B.3 Orthogonality

We first have:

$$\langle \mathcal{L}\phi_p, \varphi_q \rangle = \int_0^{Z_2} \overline{\varphi_p} \cdot \mathcal{L}\phi_q \, \mathrm{d}z = \int_0^{Z_2} \overline{\varphi_p} \cdot k_{rq}^2 \phi_q \, \mathrm{d}z = k_{rq}^2 \int_0^{Z_2} \overline{\varphi_p} \cdot \phi_q \, \mathrm{d}z, \tag{B.27}$$

We also have:

$$\langle \phi_p, M\varphi_i \rangle = \int_0^{Z_2} \overline{\mathcal{M}\varphi_p} \cdot \phi_q \, \mathrm{d}z = \int_0^{Z_2} k_{rp}^2 \overline{\varphi_p} \cdot \phi_q \, \mathrm{d}z = k_{rp}^2 \int_0^{Z_2} \overline{\varphi_p} \cdot \phi_q \, \mathrm{d}z, \tag{B.28}$$

Since $\langle \mathcal{L}\phi_p, \varphi_q \rangle = \langle \phi_p, M\varphi_i \rangle$, we will have:

$$k_{rp}^2 \int_0^{Z_2} \overline{\varphi_p} \cdot \phi_q \, \mathrm{d}z = k_{rq}^2 \int_0^{Z_2} \overline{\varphi_p} \cdot \phi_q \, \mathrm{d}z \tag{B.29}$$

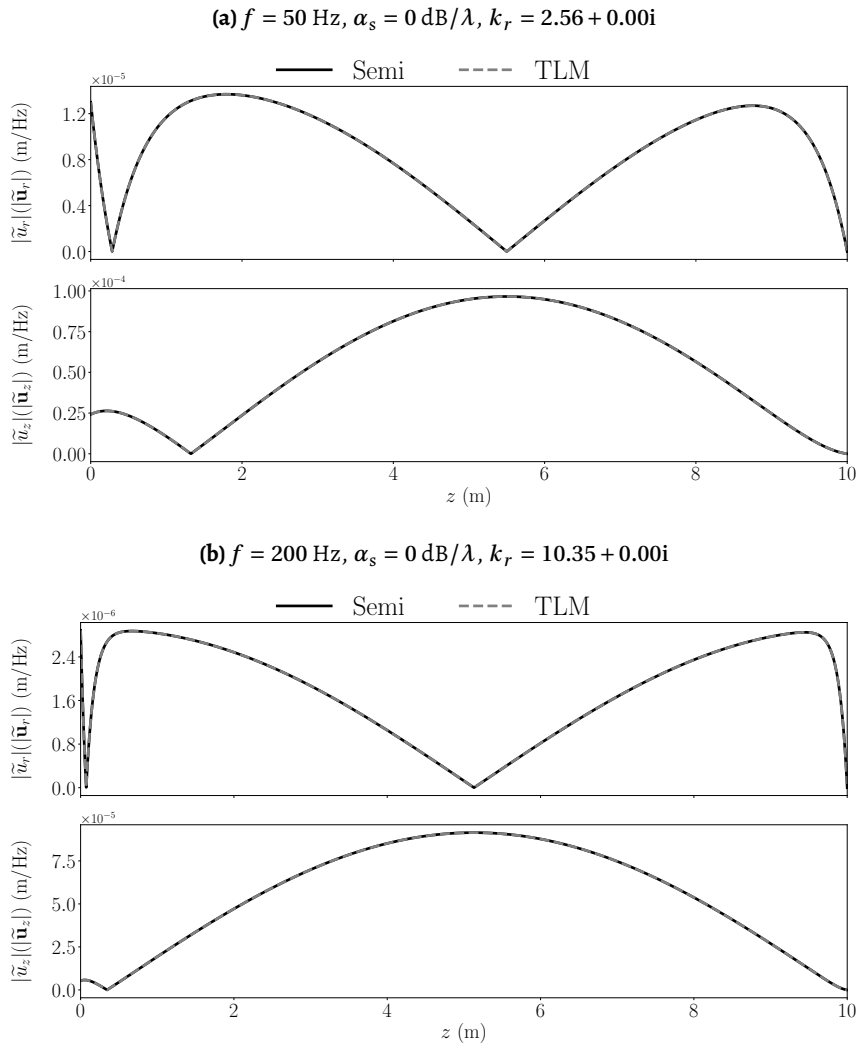The orthogonality between the eigenvector and its conjugate eigenvector is finally given as:

$$\left(k_{rp}^2 - k_{rq}^2 \right)\int_0^{Z_2} \overline{\varphi_p} \cdot \phi_q \, \mathrm{d}z = 0 \tag{B.30}$$

C

Additional Comparison of Modes for a Single Elastic Domain

This Appendix provides the additional comparisons of continuous and discrete modal solutions of a single elastic layer in Chapter 3.
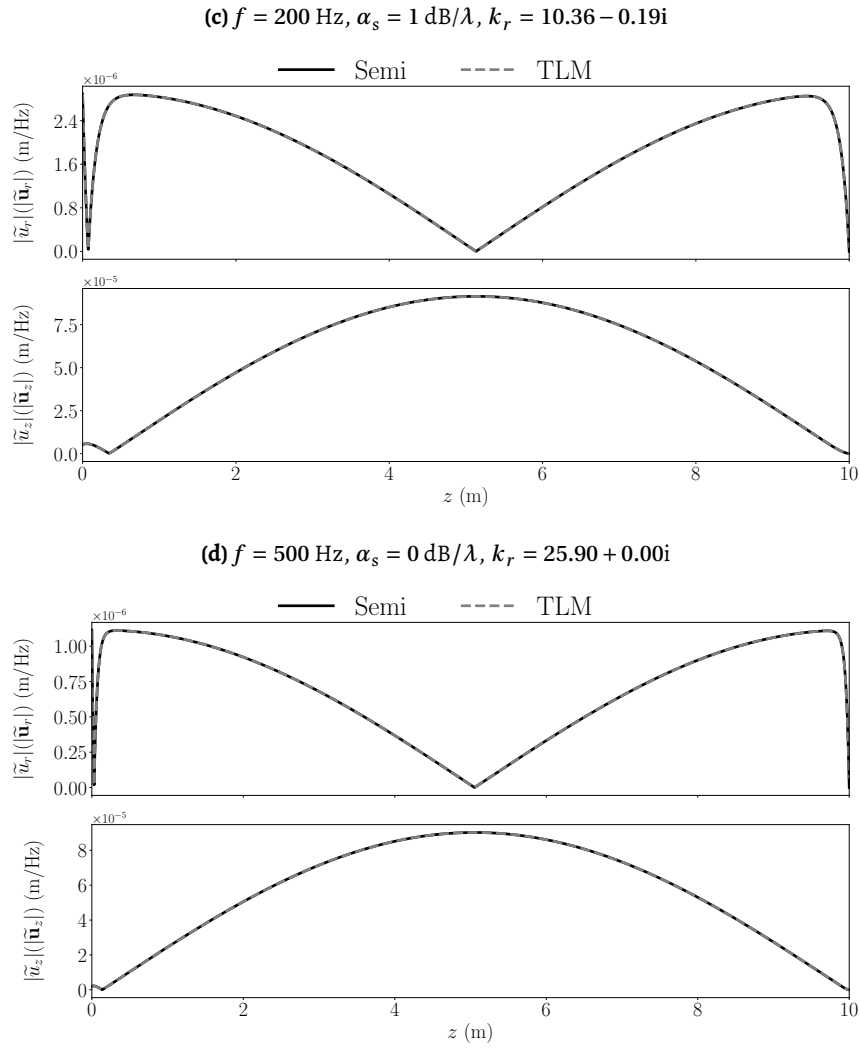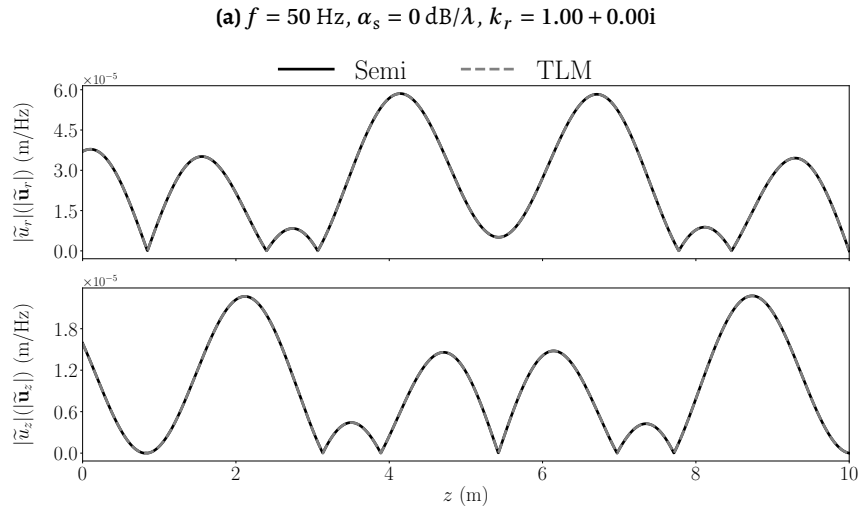
C.1 SV wave type modes

(a) $f = 50\ \text{Hz},\ \alpha_s = 0\ \text{dB}/\lambda,\ k_r = 2.56 + 0.00\text{i}$

(b) $f = 200\ \text{Hz},\ \alpha_s = 0\ \text{dB}/\lambda,\ k_r = 10.35 + 0.00\text{i}$

(c) $f = 200\,\text{Hz}$, $\alpha_\text{s} = 1\,\text{dB}/\lambda$, $k_r = 10.36 - 0.19\text{i}$

(d) $f = 500\,\text{Hz}$, $\alpha_\text{s} = 0\,\text{dB}/\lambda$, $k_r = 25.90 + 0.00\text{i}$

Figure C.1. Comparison of selected normalized SV wave type modes obtained from semi-analytical (black-continuous line) and TLM solutions (grey-dashed line) for different cases: (a) $f = 50\,\text{Hz}$, $\alpha_\text{s} = 0\,\text{dB}/\lambda$, (b) $f = 200\,\text{Hz}$, $\alpha_\text{s} = 0\,\text{dB}/\lambda$, (c) $f = 200\,\text{Hz}$, $\alpha_\text{s} = 1\,\text{dB}/\lambda$, (d) $f = 500\,\text{Hz}$, $\alpha_\text{s} = 0\,\text{dB}/\lambda$.

C.2 P wave type modes

(a) $f = 50\,\text{Hz}$, $\alpha_\text{s} = 0\,\text{dB}/\lambda$, $k_r = 1.00 + 0.00\text{i}$

(a) $f = 200\,\text{Hz}$, $\alpha_s = 0\,\text{dB}/\lambda$, $k_r = 4.22 + 0.00\text{i}$

(b) $f = 200\,\text{Hz}$, $\alpha_s = 1\,\text{dB}/\lambda$, $k_r = 4.22 - 0.08\text{i}$

(c) $f = 500\,\text{Hz}$, $\alpha_s = 0\,\text{dB}/\lambda$, $k_r = 10.57 + 0.00\text{i}$
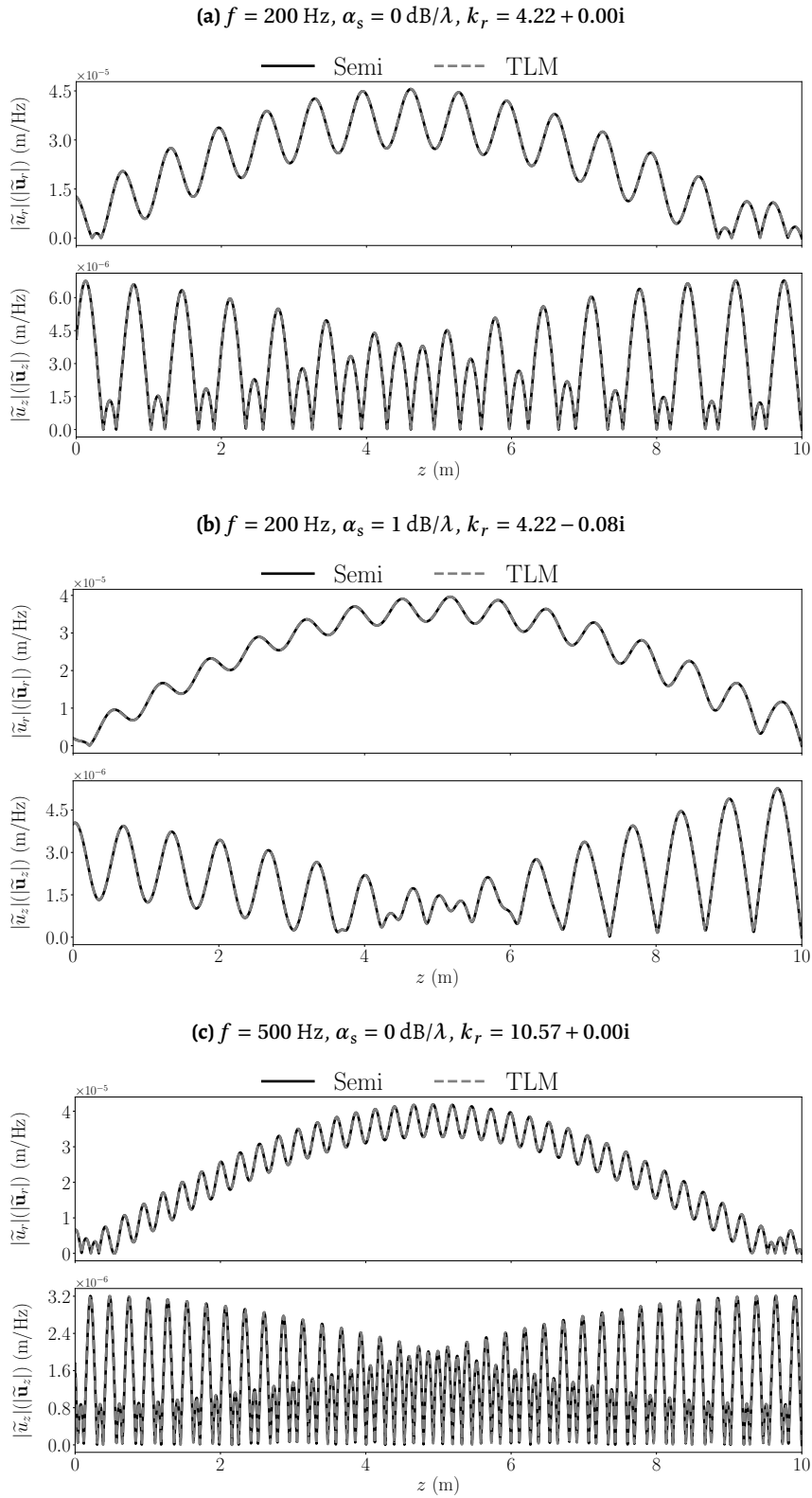
Figure C.3. Comparison of selected normalized P wave type modes obtained from semi-analytical (black-continuous line) and TLM solutions (grey-dashed line) for different cases: (a) $f = 50\,\text{Hz}$, $\alpha_s = 0\,\text{dB}/\lambda$, (b) $f = 200\,\text{Hz}$, $\alpha_s = 0\,\text{dB}/\lambda$, (c) $f = 200\,\text{Hz}$, $\alpha_s = 1\,\text{dB}/\lambda$, (d) $f = 500\,\text{Hz}$, $\alpha_s = 0\,\text{dB}/\lambda$.

C.3 Evanescent type modes

(a) $f = 50$ Hz, $\alpha_s = 0$ dB/λ, $k_r = 0.54 - 14.94i$

(b) $f = 200$ Hz, $\alpha_s = 0$ dB/λ, $k_r = 0.30 - 14.73i$
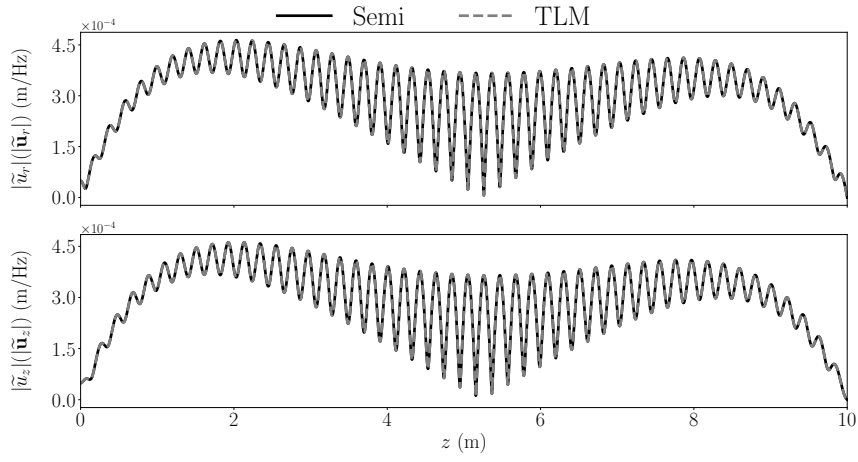
(c) $f = 50$ Hz, $\alpha_s = 1$ dB/λ, $k_r = 0.41 - 14.77i$
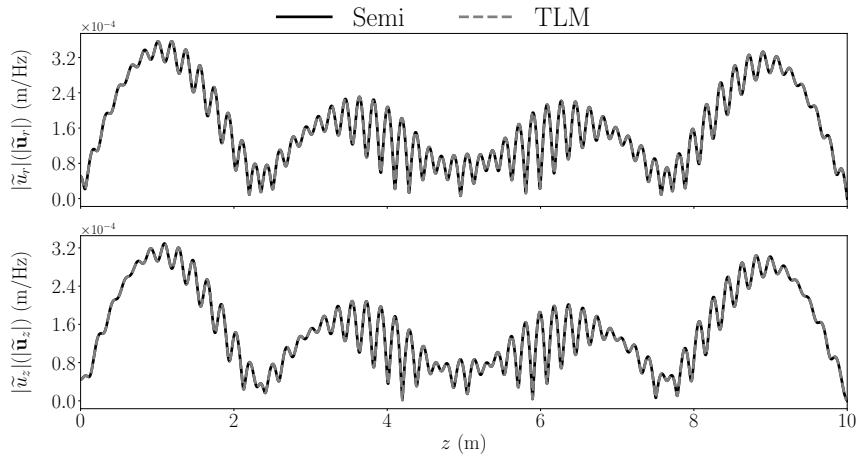
(a) $f = 50$ Hz, $\alpha_s = 0$ dB/λ, $k_r = 0.00 - 9.69$i
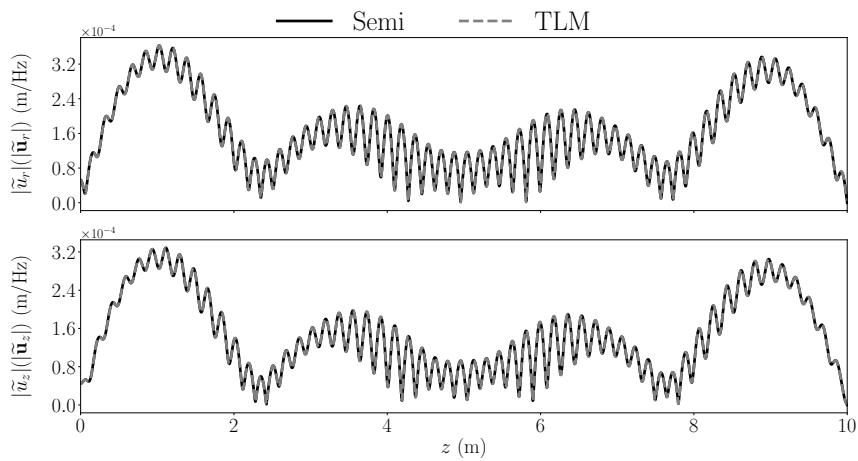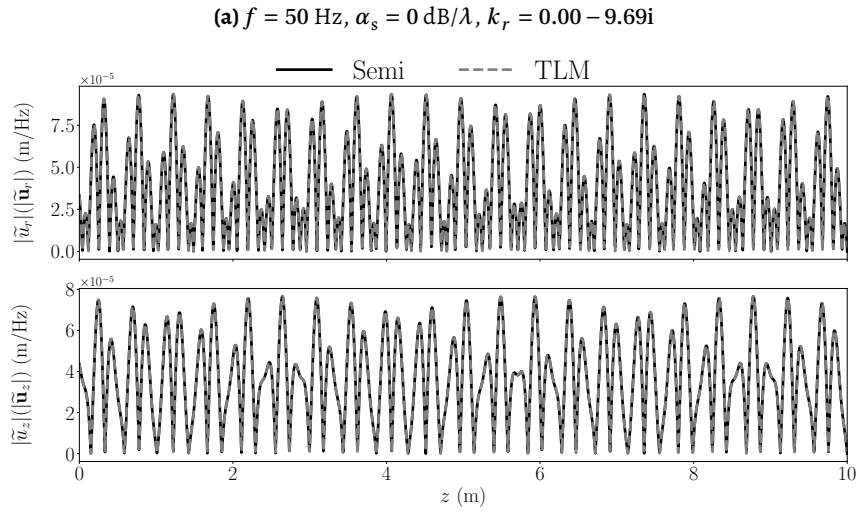
Figure C.5. Comparison of selected normalized evanescent wave type modes obtained from semi-analytical (black-continuous line) and TLM solutions (grey-dashed line) for different cases: (a) $f = 50$ Hz, $\alpha_s = 0$ dB/λ, (b) $f = 200$ Hz, $\alpha_s = 0$ dB/λ, (c) $f = 200$ Hz, $\alpha_s = 1$ dB/λ, (d) $f = 500$ Hz, $\alpha_s = 0$ dB/λ.

D

Additional Results of an Elastic Domain with PML

This Appendix provides additional results of Chapter 5, including

1. The comparison of eigenvalues for Groups 1.1, 1.3 and 1.4 in Table 5.2.

2. The comparison of matched eigenmodes for Groups 1.1, 1.3 and 1.4 in Table 5.2.

3. The modal orthogonality plots for Groups 1.1, 1.3 and 1.4 in Table 5.2.

D.1 Comparisons of Eigenvalues

(a) $h_\ell = 0.25$ m, comparison of roots

(b) $h_\ell = 0.25$ m, zoomed-in comparison of roots

(c) $h_\ell = 0.01$ m, comparison of roots

(d) $h_\ell = 0.01$ m, zoomed-in comparison of roots
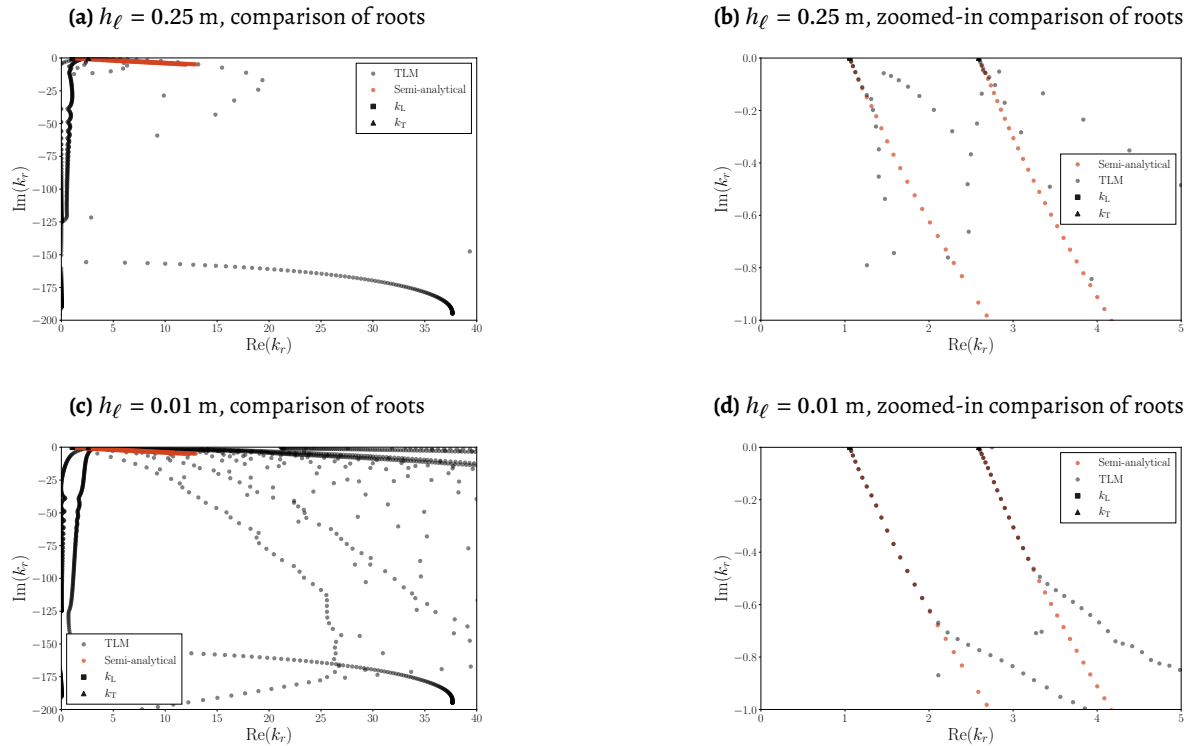
Figure D.1. Comparison of eigenvalues obtained via semi-analytical approach(red circles) and TLM (black crosses) for $f = 50$Hz, $\alpha_s = 0\,\mathrm{dB}/\lambda$: (a) and (b): $h_\ell = 0.25$ m; (c) and (d): $h_\ell = 0.01$ m.

(a) $h_\ell = 0.25$ m, comparison of roots

(b) $h_\ell = 0.25$ m, zoomed-in comparison of roots

(c) $h_\ell = 0.01$ m, comparison of roots

(d) $h_\ell = 0.01$ m, zoomed-in comparison of roots
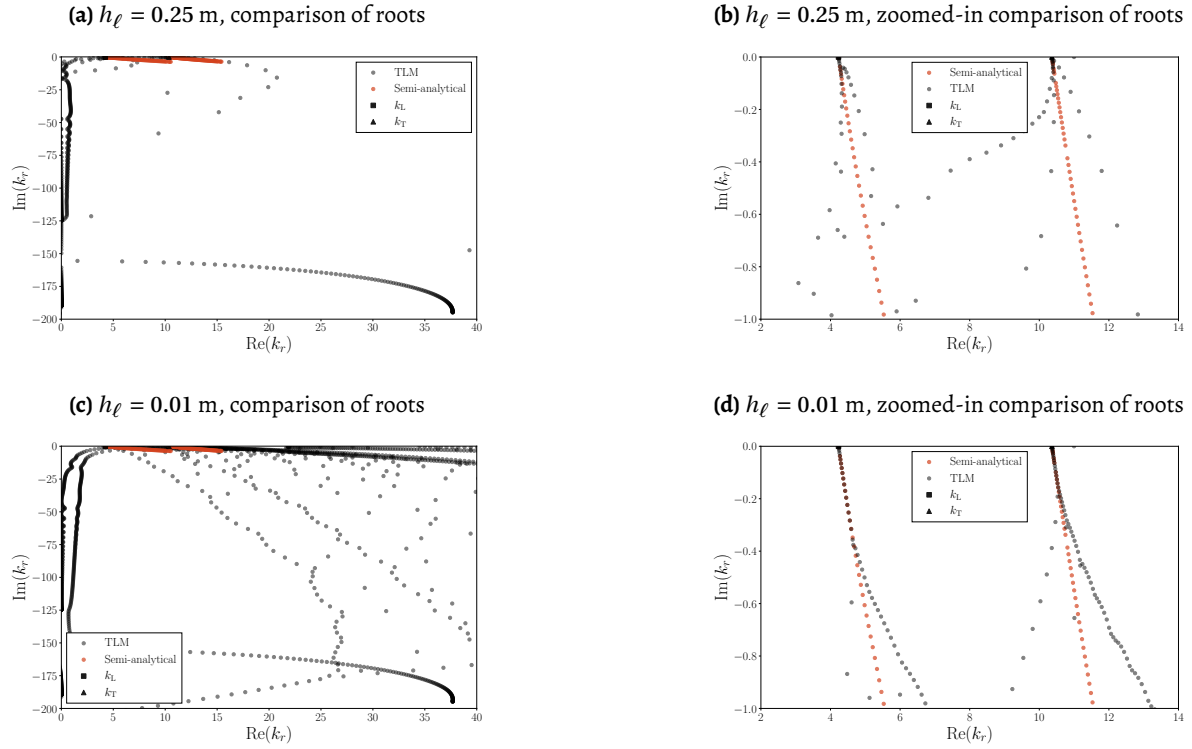
Figure D.2. Comparison of eigenvalues obtained via semi-analytical approach(red circles) and TLM (black crosses) for $f = 200$Hz, $\alpha_s = 0$ dB$/\lambda$: (a) and (b): $h_\ell = 0.25$ m; (c) and (d): $h_\ell = 0.01$ m.

(a) $h_\ell = 0.25$ m, comparison of roots

(b) $h_\ell = 0.25$ m, zoomed-in comparison of roots

(c) $h_\ell = 0.01$ m, comparison of roots

(d) $h_\ell = 0.01$ m, zoomed-in comparison of roots
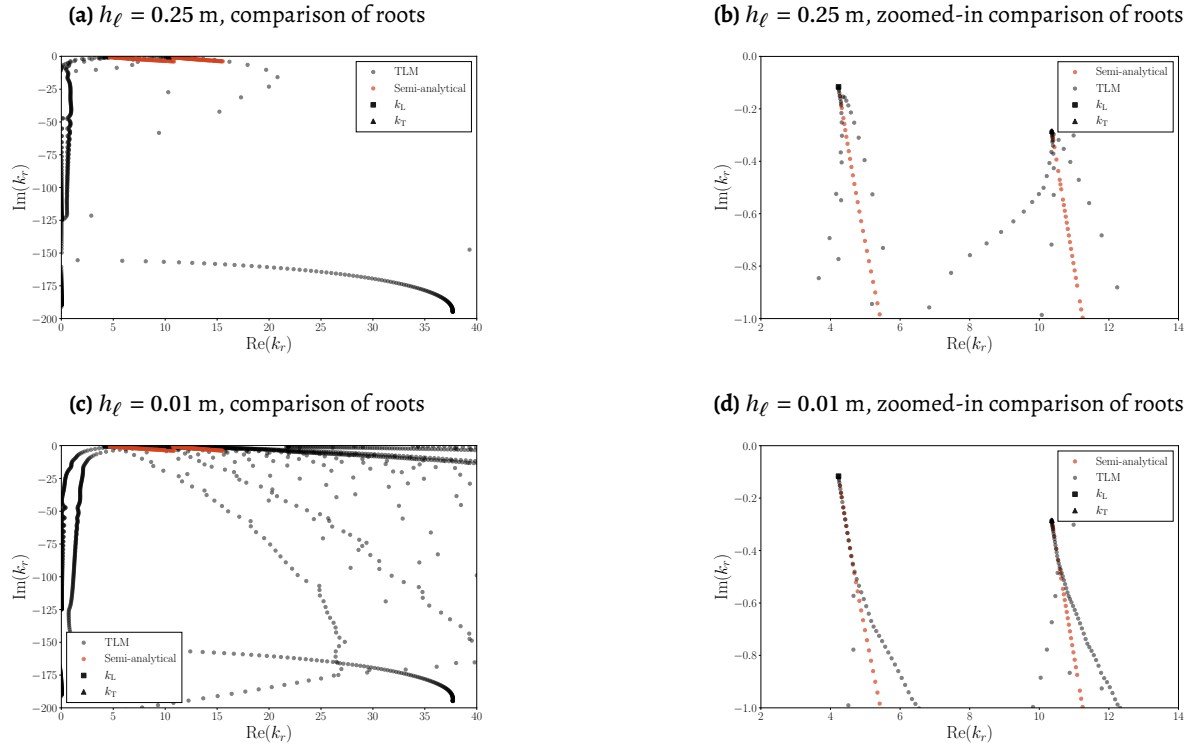
Figure D.3. Comparison of eigenvalues obtained via semi-analytical approach(red circles) and TLM (black crosses) for $f = 200$Hz, $\alpha_s = 1.5$ dB$/\lambda$: (a) and (b): $h_\ell = 0.25$ m; (c) and (d): $h_\ell = 0.01$ m.

D.2 Comparisons of Eigenmodes

(a) $f = 50$ Hz, $\alpha_s = 0\,\text{dB}/\lambda$

(b) $f = 200$ Hz, $\alpha_s = 0\,\text{dB}/\lambda$
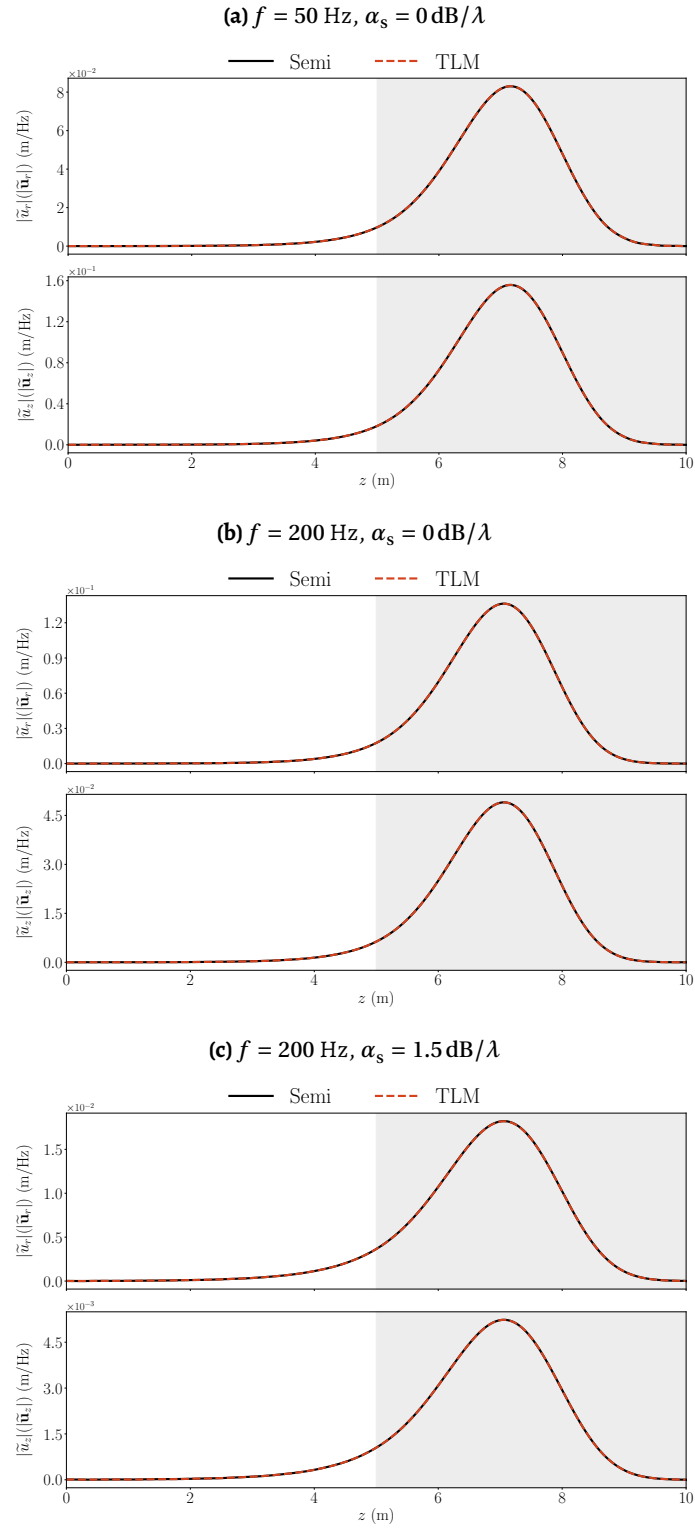
(c) $f = 200$ Hz, $\alpha_s = 1.5\,\text{dB}/\lambda$

Figure D.4. Comparison of eigenvectors obtained via semi-analytical approach (black-continuous line) and TLM (red-dashed line), and grey domain indicates the PML for (a) $f = 50$Hz, $\alpha_s = 0\,\text{dB}/\lambda$; (b): $f = 200$Hz, $\alpha_s = 0\,\text{dB}/\lambda$; (b): $f = 200$Hz, $\alpha_s = 1.5\,\text{dB}/\lambda$

D.3 Orthogonality

Semi-analytical solution

(a) $f = 50$ Hz and $\alpha_s = 0\text{dB}/\lambda$.
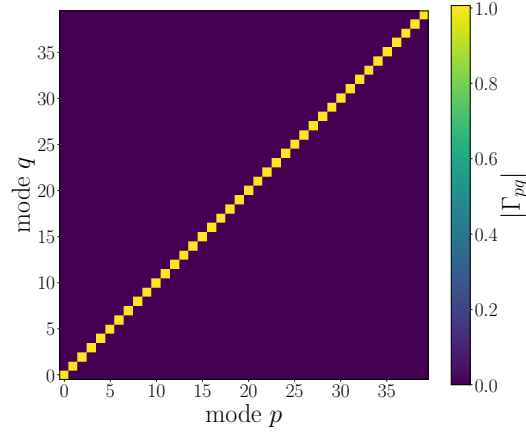
(b) $f = 200$ Hz and $\alpha_s = 0\text{dB}/\lambda$.
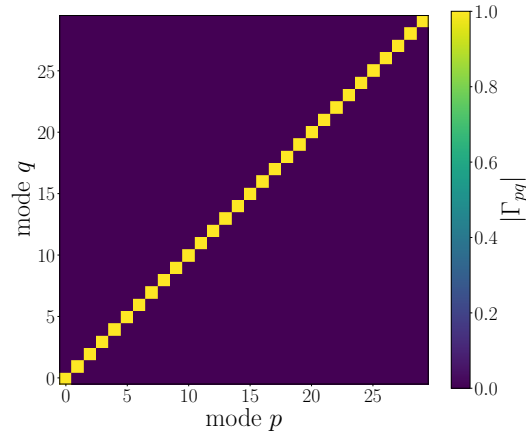
(c) $f = 200$ Hz and $\alpha_s = 1.5\text{dB}/\lambda$.
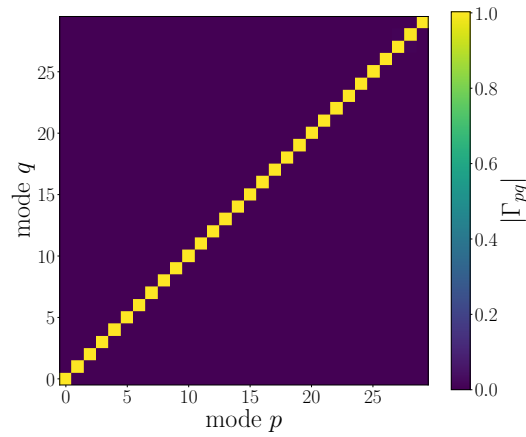
Figure D.5. Orthogonality of first forty modes at $f = 50$ Hz and first thirty modes at $f = 200$ Hz obtained via semi-analytical method

Thin layer method

(a) $\alpha_s = 0\text{dB}/\lambda$, $f = 50$ Hz, $h_\ell = 0.25$ m

(b) $\alpha_s = 0\text{dB}/\lambda$, $f = 50$ Hz, $h_\ell = 0.01$ m

(c) $\alpha_s = 0\text{dB}/\lambda$, $f = 200$ Hz, $h_\ell = 0.25$ m

(d) $\alpha_s = 1.5\text{dB}/\lambda$, $f = 200$ Hz, $h_\ell = 0.01$ m

(e) $\alpha_s = 1.5\text{dB}/\lambda$, $f = 200$ Hz, $h_\ell = 0.25$ m

(f) $\alpha_s = 0\text{dB}/\lambda$, $f = 200$ Hz, $h_\ell = 0.01$ m
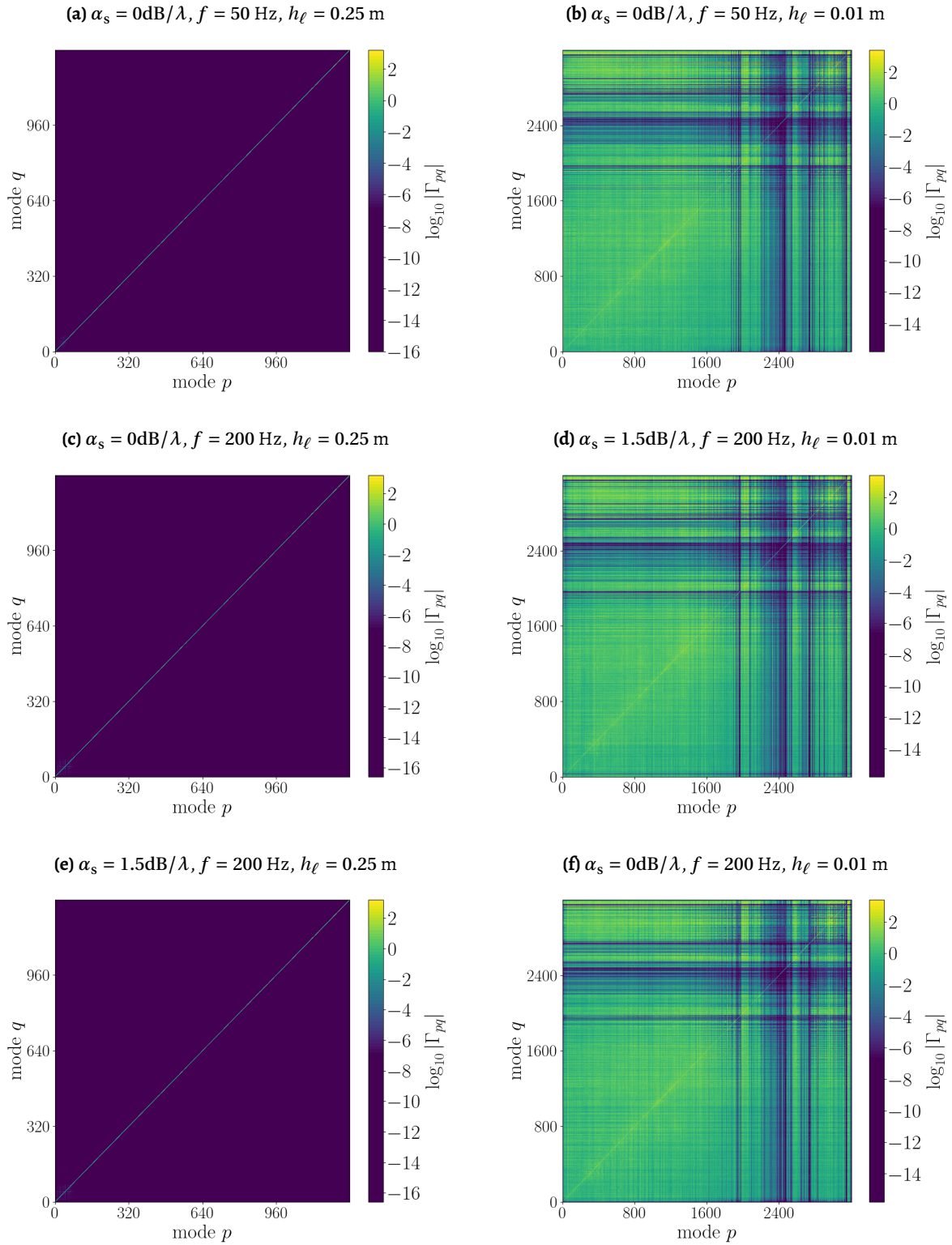
Figure D.6. Orthogonality of all modes obtained via TLM: left column: good orthogonality when $h_\ell = 0.25$ m, right column: violated orthogonality when $h_\ell = 0.01$ m.

E

Additional results of an acousto-elastic domain with PML

E.1 Results at 100 Hz

(a) f = 100 Hz, Eigenvalues

(b) f = 100 Hz, Orthogonality
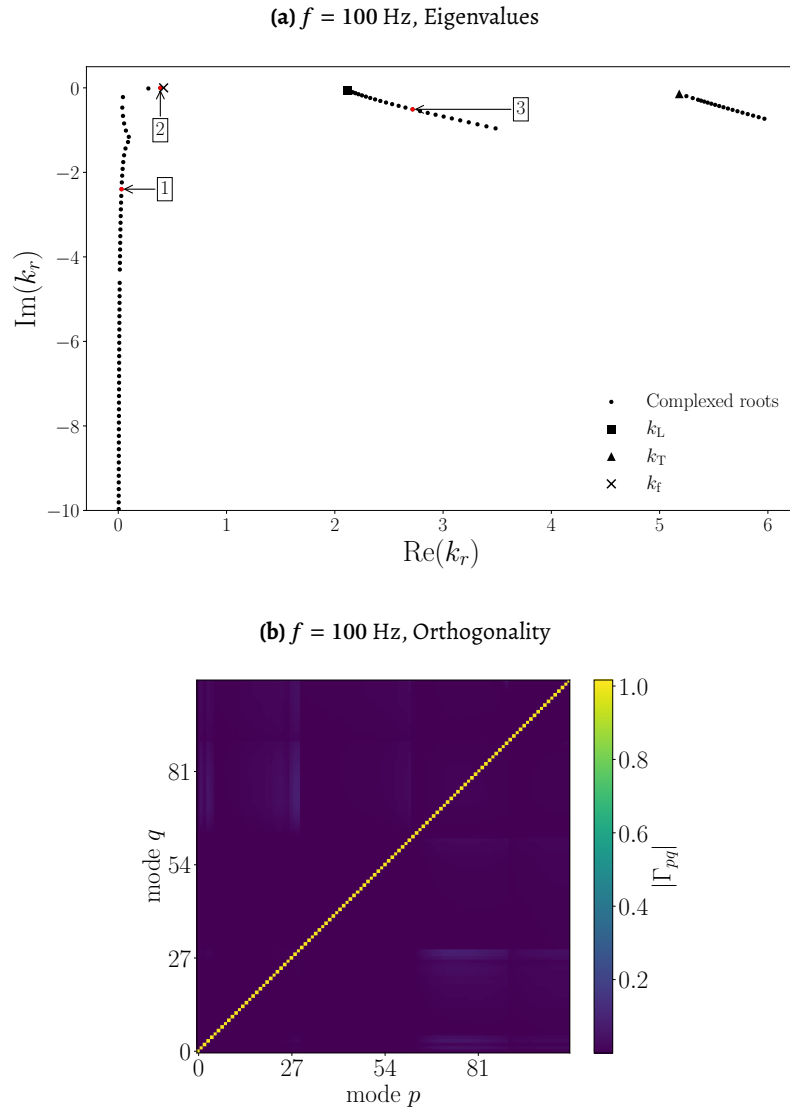
Figure E.1. Orthogonality of the first 108 modes of the acousto-elastic layer with one PML at f = 100 Hz.

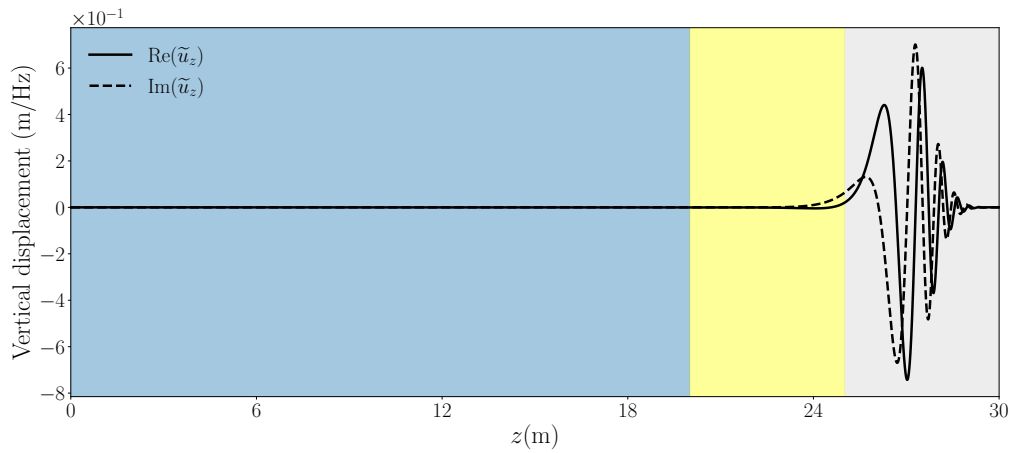**(a)** f = 100 Hz, vertical pressure eigenfunction for wavenumber **1** as marked in Figure E.1a
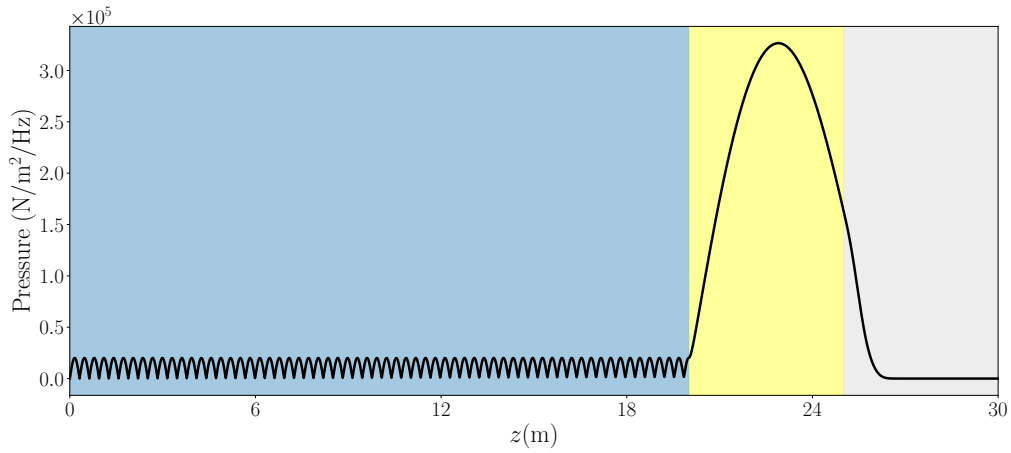
(b) f = 100 Hz, vertical pressure eigenfunction for wavenumber **2** as marked in Figure E.1a
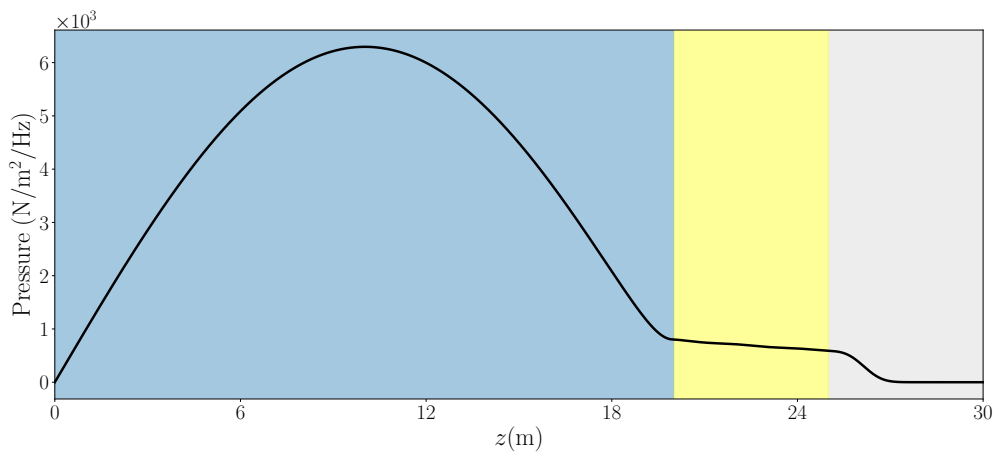
(c) f = 100 Hz, vertical pressure eigenfunction for wavenumber **3** as marked in Figure E.1a
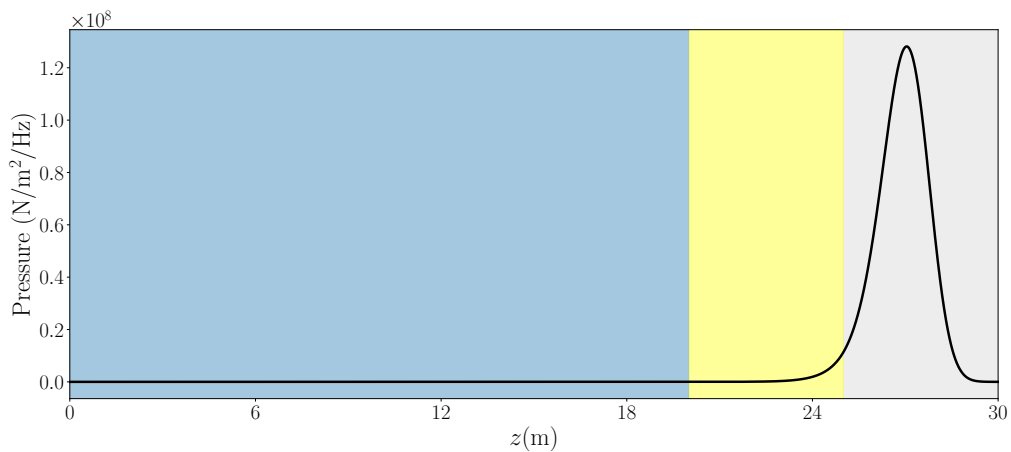
Figure E.2. Pressure field distributions for three types of modes at frequency f = 100 Hz. The computational domain consists of the acoustic region (blue), the elastic region (yellow), and the perfectly matched layer (PML) region (grey).
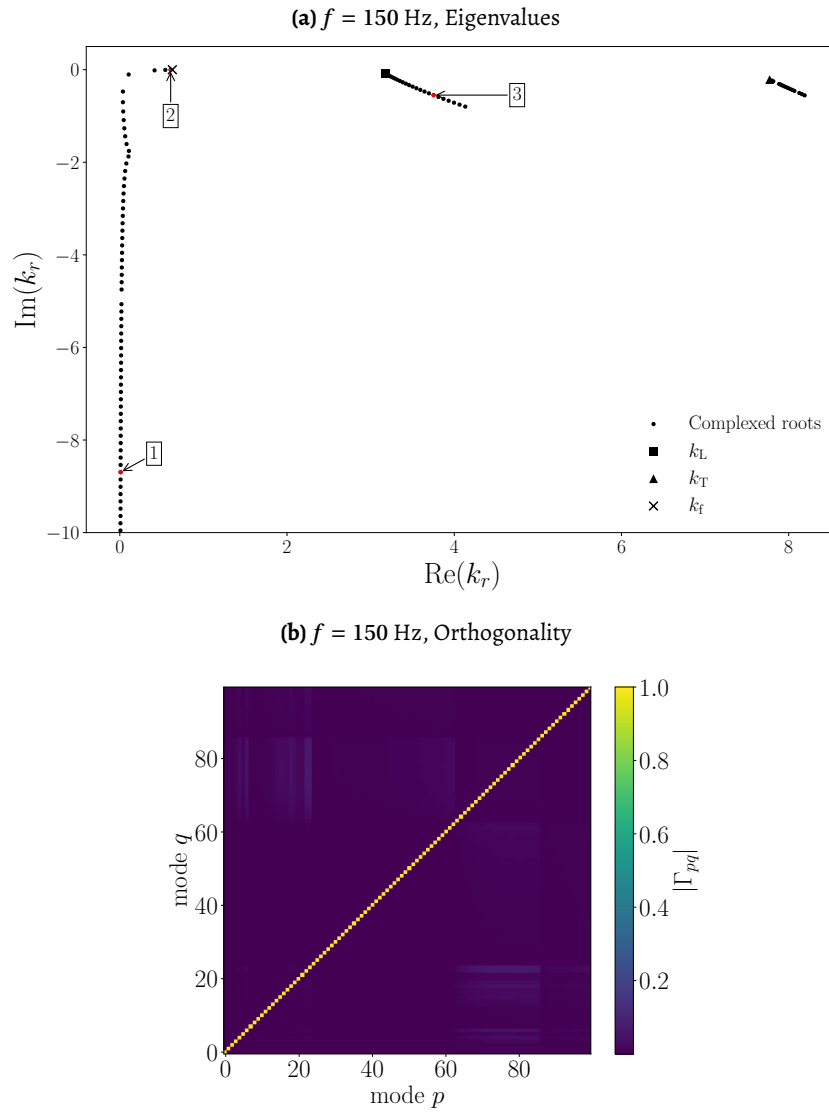
(a) $f = 100$ Hz, vertical displacement eigenfunction for wavenumber **1** as marked in Figure E.1a
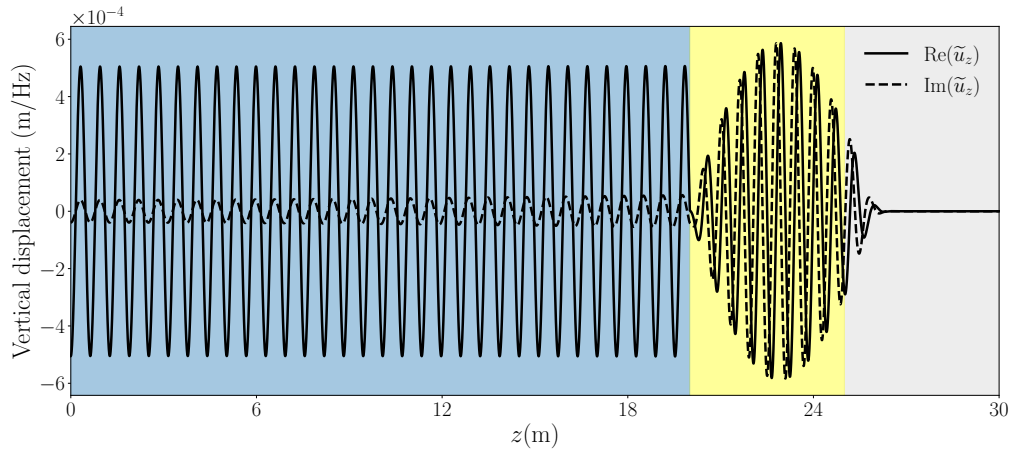
(b) $f = 100$ Hz, vertical displacement eigenfunction for wavenumber **2** as marked in Figure E.1a
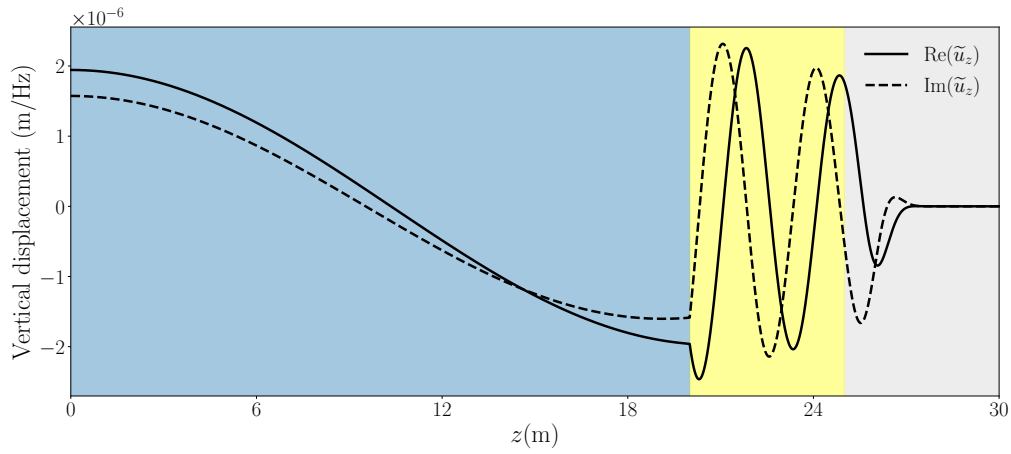
(c) $f = 100$ Hz, vertical displacement eigenfunction for wavenumber **3** as marked in Figure E.1a

Figure E.3. Displacement field distributions for three types of modes at frequency $f = 100$ Hz. The computational domain consists of the acoustic region (blue), the elastic region (yellow), and the perfectly matched layer (PML) region (grey).

E.2 Results at 150 Hz

(a) f = 150 Hz, Eigenvalues

(b) f = 150 Hz, Orthogonality

Figure E.4. Orthogonality of the first 100 modes of the acousto-elastic layer with one PML at f = 150 Hz.
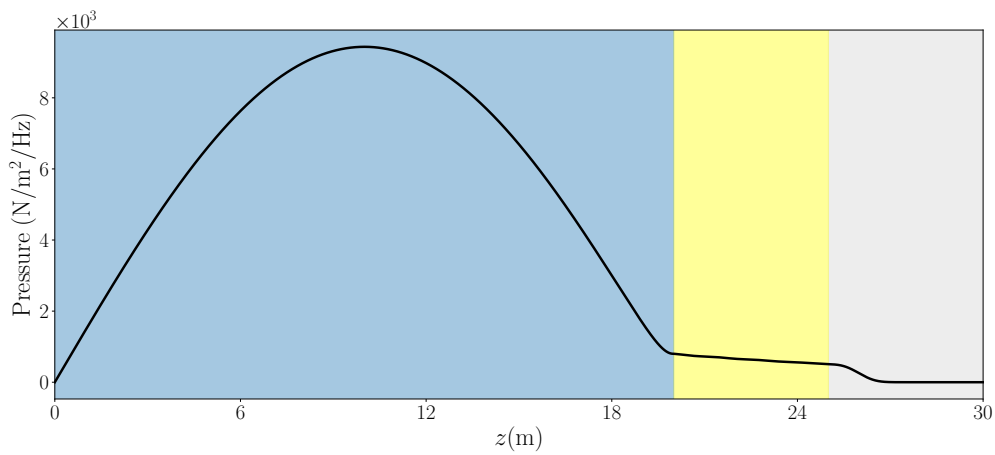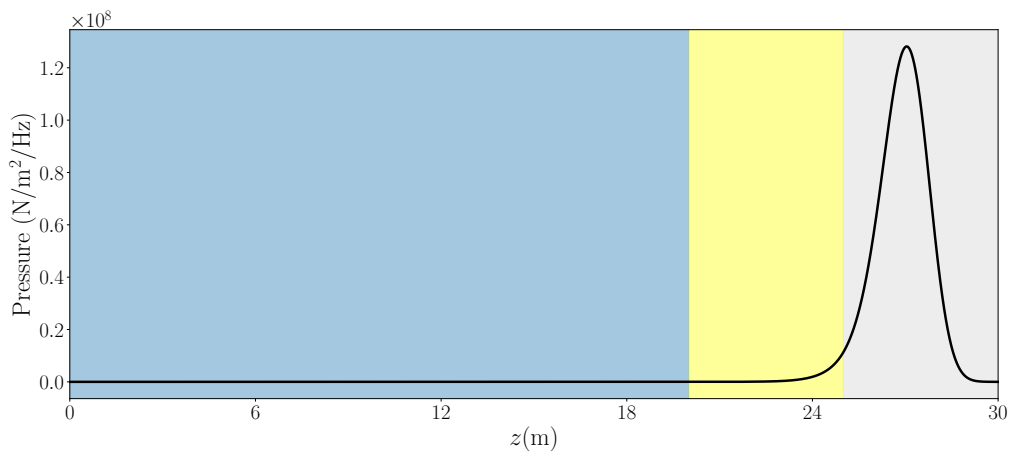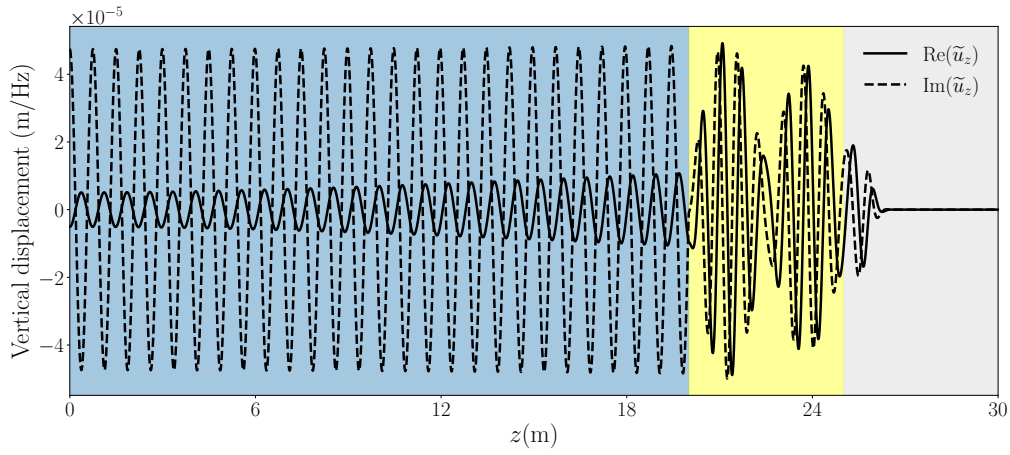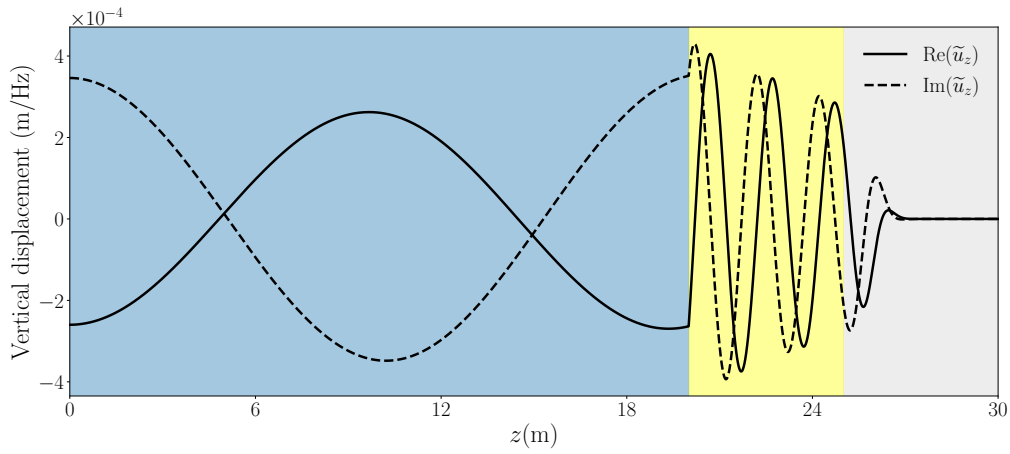
(a) f = 150 Hz, vertical pressure eigenfunction for wavenumber **1** as marked in Figure E.4a
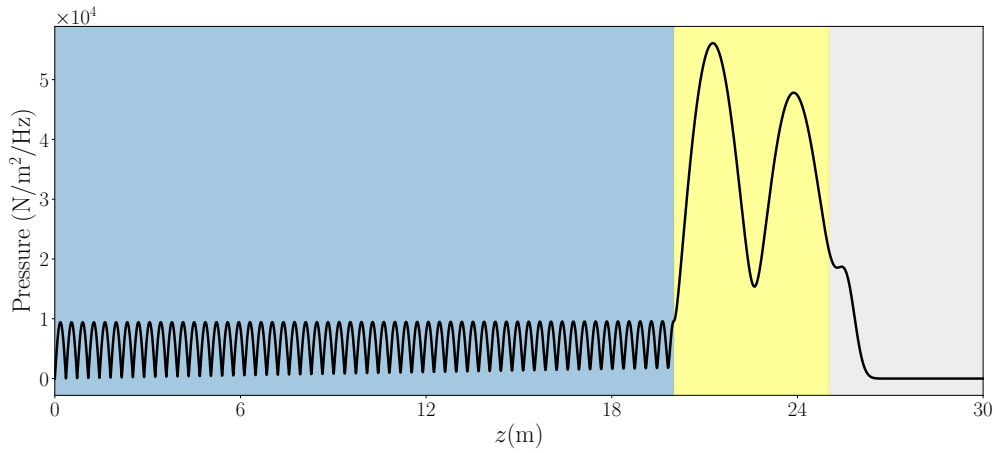
(b) f = 150 Hz, vertical pressure eigenfunction for wavenumber **2** as marked in Figure E.4a

(c) f = 150 Hz, vertical pressure eigenfunction for wavenumber **3** as marked in Figure E.4a

Figure E.5. Pressure field distributions for three types of modes at frequency f = 100 Hz. The computational domain consists of the acoustic region (blue), the elastic region (yellow), and the perfectly matched layer (PML) region (grey).

(a) $f = 150$ Hz, vertical displacement eigenfunction for wavenumber **1** as marked in Figure E.4a

(b) $f = 150$ Hz, vertical displacement eigenfunction for wavenumber **2** as marked in Figure E.4a

(c) $f = 150$ Hz, vertical displacement eigenfunction for wavenumber **3** as marked in Figure E.4a
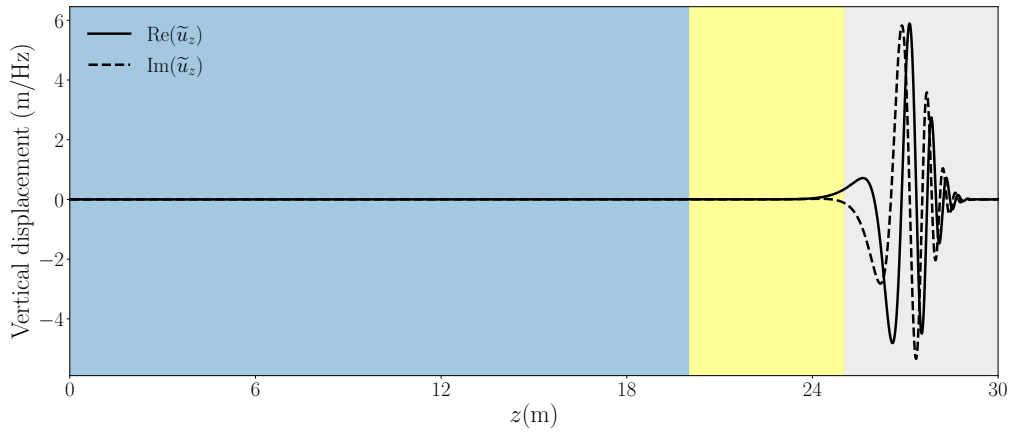

Figure E.6. Displacement field distributions for three types of modes at frequency $f = 150$ Hz. The computational domain consists of the acoustic region (blue), the elastic region (yellow), and the perfectly matched layer (PML) region (grey).